

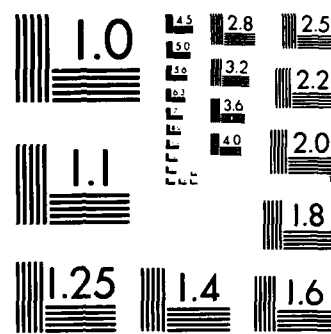
RD-A184 468 FAILURE ANALYSIS OF COMPOSITE STRUCTURE MATERIALS(U) 1/2
BOEING MILITARY AIRPLANE CO SEATTLE WA B SMITH ET AL.
27 MAY 87 AFWAL-TR-87-4001 F33615-84-C-5010
UNCLASSIFIED F/G 11/4 NL

UNCLASSIFIED

F/G 11/4

1/2

46



MICROCOPY RESOLUTION TEST CHART
NATIONAL BUREAU OF STANDARDS-1963-A

DTIC FILE COPY

2

AD-A184 468

AFWAL-TR-87-4001



FAILURE ANALYSIS OF COMPOSITE STRUCTURE MATERIALS

Brian Smith
Ray Grove
Boeing Military Airplane Company
P.O. Box 3707 MS 73-43
Seattle, WA 98124

DTIC
SELECTED
S D
SEP 16 1987
C D

May 1987

Final Report for Period of 1 October 1985 to 31 August 1986

Approved for public release; distribution is unlimited

Materials Laboratory
Air Force Wright Aeronautical Laboratory
Air Force Systems Command
Wright-Patterson Air Force Base, OH 45433-6533

NOTICE

When Government drawings, specifications, or other data are used for any purpose other than in connection with a definitely related Government procurement operation, the United States Government thereby incurs no responsibility nor any obligation whatsoever; and the fact that the government may have formulated, furnished, or in any way supplied the said drawings, specifications, or other data, is not to be regarded by implication or otherwise as in any manner licensing the holder or any other person or corporation, or conveying any rights or permission to manufacture, use, or sell any patented invention that may in any way be related thereto.

This report has been reviewed by the Office of Public Affairs (ASD/PA) and is releasable to the National Technical Information Service (NTIS). At NTIS, it will be available to the general public, including foreign nations.

This technical report has been reviewed and is approved for publication.



Frank J. Feclek

Air Force Project Engineer

FOR THE COMMANDER



Theodore Reinhart, Branch Chief

Materials Engineering Branch

Systems Support Division

Materials Laboratory

If your address has changed, if you wish to be removed from our mailing list, or if the addressee is no longer employed by your organization please notify AFW AL/MLSE, W-PAFB, OH 45433-6533 to help us maintain a current mailing list.

Copies of this report should not be returned unless return is required by security considerations, contractual obligations, or notice on a specific document.

UNCLASSIFIED

SECURITY CLASSIFICATION OF THIS PAGE

REPORT DOCUMENTATION PAGE

1a REPORT SECURITY CLASSIFICATION UNCLASSIFIED		1b. RESTRICTIVE MARKINGS										
2a SECURITY CLASSIFICATION AUTHORITY		3 DISTRIBUTION/AVAILABILITY OF REPORT Approved for public release; distribution is unlimited.										
2b. DECLASSIFICATION / DOWNGRADING SCHEDULE												
4. PERFORMING ORGANIZATION REPORT NUMBER(S)		5 MONITORING ORGANIZATION REPORT NUMBER(S) AFWAL-TR-87-4001										
6a NAME OF PERFORMING ORGANIZATION Boeing Military Airplane Company	6b OFFICE SYMBOL (If applicable) AFWAL/MLSE	7a NAME OF MONITORING ORGANIZATION Air Force Wright Aeronautical Laboratory, Materials Laboratory, Systems Support Division										
6c. ADDRESS (City, State, and ZIP Code) P. O. Box 3707, MS 73-43 Seattle, WA 98124		7b ADDRESS (City, State, and ZIP Code) AFWAL/MLSE Wright Patterson AFB, OH 45433-6533										
8a. NAME OF FUNDING / SPONSORING ORGANIZATION	8b OFFICE SYMBOL (If applicable) AFWAL/MLSE	9 PROCUREMENT INSTRUMENT IDENTIFICATION NUMBER Contract No. F33615-84-C-5010										
8c. ADDRESS (City, State, and ZIP Code) WPAFB, OH 45433-6533		10 SOURCE OF FUNDING NUMBERS <table border="1"> <tr> <td>PROGRAM ELEMENT NO 62102F</td> <td>PROJECT NO 2418</td> <td>TASK NO 04</td> <td>WORK UNIT ACCESSION NO 31</td> </tr> </table>		PROGRAM ELEMENT NO 62102F	PROJECT NO 2418	TASK NO 04	WORK UNIT ACCESSION NO 31					
PROGRAM ELEMENT NO 62102F	PROJECT NO 2418	TASK NO 04	WORK UNIT ACCESSION NO 31									
11 TITLE (Include Security Classification) Failure Analysis of Composite Structure Materials												
12 PERSONAL AUTHOR(S) Brian Smith, Ray Grove												
13a TYPE OF REPORT Final	13b TIME COVERED FROM Oct 1985 TO Aug 1986	14. DATE OF REPORT (Year, Month, Day) 87/05/27	15 PAGE COUNT									
16. SUPPLEMENTARY NOTATION												
17 COSATI CODES <table border="1"> <tr> <th>FIELD</th> <th>GROUP</th> <th>SUB-GROUP</th> </tr> <tr> <td>11</td> <td>04</td> <td></td> </tr> <tr> <td></td> <td></td> <td></td> </tr> </table>	FIELD	GROUP	SUB-GROUP	11	04					18. SUBJECT TERMS (Continue on reverse if necessary and identify by block number) Composites, composite structure, failure analysis, fractography, graphite-epoxy, stress analysis, nondestructive evaluation, materials characterization, and in situ SEM.		
FIELD	GROUP	SUB-GROUP										
11	04											
19 ABSTRACT (Continue on reverse if necessary and identify by block number)				<p>The objectives of the Failure Analysis for Composite Structural Materials program are to develop analytical and diagnostic techniques that can be used for determining the causes of failure in composite materials and to incorporate these results into a compendium of procedures that may be used as a reference manual when conducting a postfailure analysis of a composite structure, given the failed part as the starting point of the investigation. Such techniques include flowcharts describing the logical arrangement of investigative operations along with diagnostic procedures that reveal the cause and mechanism of failure. To achieve these objectives, this program was divided into five tasks: (1) task 1—literature search and diagnostic technique selection, (2) task 2—specimen production and test, (3) task 3—diagnostic technique evaluations, (4) task 4—creation of a failure analysis compendium, and (5) task 5—evaluation and demonstration of techniques. This final report summarizes the progress and findings of activities carried out for tasks 1 through 5 that identified, organized, and examined a variety of postfailure analysis methods for composite materials. Because such failures may arise from a wide variety of causes, analysis techniques examined included four basic disciplines: nondestructive evaluation (NDE), stress analysis, fractography, and materials characterization.</p>								
20 DISTRIBUTION/AVAILABILITY OF ABSTRACT <input checked="" type="checkbox"/> UNCLASSIFIED/UNLIMITED <input type="checkbox"/> SAME AS RPT <input type="checkbox"/> DTIC USERS		21 ABSTRACT SECURITY CLASSIFICATION Unclassified										
22a NAME OF RESPONSIBLE INDIVIDUAL Frank Fecak		22b TELEPHONE (Include Area Code) 513-255-7483	22c OFFICE SYMBOL AFWAL/MLSE									

SUMMARY

The objectives of the Failure Analysis for Composite Structural Materials program were to develop analytical and diagnostic techniques that can be used for determining the causes of failure in composite materials and to incorporate these results into a compendium of procedures which may be used as a reference manual when conducting a postfailure analysis of a composite structure, given the failed part as the starting point of the investigation. Such techniques included flow charts describing the logical arrangement of investigative operations along with diagnostic procedures that reveal the cause and mechanism of failure. To achieve these objectives, this program was divided into five tasks:

- Task 1-Literature search and diagnostic technique selection.
- Task 2-Specimen production and test.
- Task 3-Diagnostic technique evaluation.
- Task 4-Creation of a failure analysis compendium.
- Task 5-Evaluation and demonstration of techniques.

This final report summarizes the progress and findings of activities carried out for tasks 1 through 5 which identified, organized, and examined a variety of postfailure analysis methods for composite materials. Because such failures may arise from a wide variety of causes, analysis techniques examined included four basic disciplines: nondestructive evaluation (NDE), stress analysis, fractography, and materials characterization. Results of efforts in the first half of this program were reported in the interim report "Failure Analysis of Composite Material Structures" (AFWAL-TR-86-4033), and included findings from tasks 1, 2, and 3. This final report briefly presents these results, with the major emphasis and detail covering efforts on tasks 2, 3, 4, and 5.

In task 1, each of these disciplines was reviewed, and specific methods valuable to the postmortem analysis of failed composite structures were identified. This investigation was accomplished by reviewing available literature in each diagnostic area and by visiting experts throughout the United States.

The literature search revealed that there were well-developed capabilities applicable to postfailure analysis using the techniques of nondestructive evaluation and materials characterization. The techniques of fractography and stress analysis were also identified in the literature, but were found insufficiently developed for direct

incorporation into the program compendium. At the conclusion of task 1, detailed flowcharts were developed outlining a logical, sequential procedure for conducting a postfailure analysis of composite materials (see section 6.0).

Tasks 2 and 3 involved the fractographic examination of pedigree specimens that failed under tightly controlled conditions of a 177°C (350°F) AS4/3501-6 graphite/epoxy system. The results provided valuable baseline information for determination of the specific fracture features relative to crack growth directions, relative load state, and separation mechanisms for a variety of simple and complex failure conditions. The simple conditions involved interlaminar Mode I tension and Mode II shear, translaminar shear, and crack of both modes at various environmental conditions and crossply orientations.

The complex conditions involved a study of structural/loading effects and defect/contamination effects. Eight primary test specimen types were designed and tested to evaluate operative failure causes, such as:

- Contaminants.
- Voids.
- Fatigue.
- Mixed modes (tension and shear).
- Manufacturing/in-service damage.
- Structure specific geometries.
- Environmental exposure.

The completion of task 4 provided a reference document which presented an overview of the analytical and diagnostic techniques that can be used to determine the causes of failure in continuous fiber reinforced composite materials. Such techniques included flow charts describing the logical arrangement of the investigative operations using fractography, materials characterization, nondestructive evaluation, and stress analysis as the primary diagnostic procedures. Interpretive methods were also presented to illustrate how to evaluate the information obtained during the application of the various analytical techniques. Finally, supportive data such as case histories of actual failure analyses and an extensive atlas of fractographs were included to provide a comparative reference source.

The task 4 Compendium has been completed and published by AFWAL as AFWAL-TR-86-4137, "Compendium of Post-Failure Analysis Techniques for Composite Materials". The Compendium should be considered as a precursor to a more comprehensive handbook which will be produced through current Air Force Contracts F33615-86-C-5071 (Boeing Military Airplane Company) and F33615-87-C-5212 (Northrop Corporation).

Task 5 involved the demonstration and evaluation of the failure analysis logic sequences (FALNs), various analytical techniques, and the overall capability to adequately define the cause of failure. During the performance of this task, the causes of failure of three-composite structural components were successfully determined. The FALNs and the various analytical techniques developed within this program were used to identify the sequence of failure, the origin locations, the loading conditions, and the direction of crack propagation for the following structural components:

- V-22 Osprey full scale wing test box.
- NASA HiMAT test wing.
- I-beam.

The successful results obtained during the postfailure analyses investigations suggested that the technology has come a long way since its initialization in the late 1970's. Through efforts within this program as well as other research programs from the scientific community, it is evident that many of the analytical instruments and methods are approaching the capability currently available for metal failure analysis. The primary deficiency evident through actual application of the various techniques on failed components, such as those evaluated in task 5, is that the fractography interpretive methods are still in the infancy stages. Although the capability to understand the microscopic fracture mechanisms and the characteristic microscopic fracture features is rapidly evolving from programs such as this, future efforts need to be aimed at lower magnification fracture analysis technique development.

SEARCHED	INDEXED
SERIALIZED	FILED
APR 19 1987	
FBI - MEMPHIS	

FOREWORD

This report documents work performed under Contract F33615-C-5010 from October 2, 1985 through August 31, 1986. This contract with the Boeing Military Airplane Company, Seattle, Washington, is monitored by AFWAL/MLSE under the direction of Mr. F. Fechek, Air Force Wright Aeronautical Laboratories, Materials Laboratory, Wright-Patterson Air Force Base, Ohio 45433-6533.

The program is being conducted by the Materials Technology organization of the Boeing Commercial Airplane Company. Mr. D. F. Sekits is the program manager, and Mr. B. W. Smith and Mr. R. A. Grove are co-principal investigators.

Other contributors to this report are Mr. T. E. Munns, Mr. R. E. Smith, and Dr. A. G. Miller of the Boeing Materials Technology group. In situ fracture analysis studies were performed at Texas A&M by Dr. W. Bradley.

The authors wish to thank Mr. F. Fechek of AFWAL/MLSE and Ms. P. Stumpff of AFWAL/MLSA for their input and guidance.

TABLE OF CONTENTS

1.0	INTRODUCTION AND OBJECTIVES	1
2.0	APPROACH	5
3.0	RESULTS	7
3.1	Task 1-Literature Search and FALN Development	7
3.2	Task 2-Production of Specialized Test Specimens	8
3.3	Task 3-Diagnostic Technique Evaluation	10
3.3.1	Results Prior to Interim Report	10
3.3.2	Results Since Interim Report	11
3.4	Task 4-Compendium of Post-Failure Analysis Procedures	13
3.5	Task 5-Verification and Demonstration of Three Failed Components	14
4.0	TASK 2-SPECIMEN FABRICATION AND TESTING	15
4.1	Objectives	15
4.2	General Approach to Task 2	15
4.3	Material Pedigree	20
4.4	Specimen Fabrication	20
4.5	Environmental Moisture Preconditioning	21
4.6	Interlaminar Mixed Mode Flexure (MMF) Testing	21
4.7	Interlaminar Fatigue Testing (Mode I and Mode II)	22
4.8	Laminate Flexure Testing	24
4.9	Fastener-Filled-Hole Testing (Tension and Compression)	24
4.10	Buckling Specimen Testing (With FEP Insert)	24
4.11	Drill Breakout Specimens	24
4.12	Interlaminar Defect and Contamination Specimens	25
4.13	Compression After Impact (CAI)	25
5.0	TASK 3 - DIAGNOSTIC TECHNIQUE EVALUATION	27
5.1	Objectives	27
5.2	Approach	27
5.3	Translaminar Mode I Tension, Environmental	29
5.3.1	Temperature Extremes, Dry	29
5.3.2	Environmental Conditions (Temperature and Moisture)	32
5.4	Translaminar Mode I Compression, Environmental	45
5.4.1	Environmental, Dry	45
5.4.2	Environmental, Wet	54
5.5	Translaminar Mode II Rail Shear	63

5.6	Interlaminar Mixed Mode Flexural (MMF)	79
5.7	Interlaminar Mode I Fatigue	80
5.8	Interlaminar Mode II Fatigue	82
5.9	Laminate Flexure	94
5.9.1	0-Degree Layup	94
5.9.2	0/90 and Quasi-Isotropic Laminates	97
5.9.3	+45/-45 Laminates	100
5.10	Fastener-Filled-Hole (Tension and Compression)	100
5.11	Drill Breakout	102
5.12	Interlaminar Defect/Contamination, Modes I and II	106
5.13	Compression After Impact (CAI)	113
5.14	Texas A&M Subcontract - In situ SEM	118
5.14.1	Overview/Approach	118
5.14.2	Experimental Procedures	118
5.14.3	Results	120
●	In Situ Fractography	120
●	Postmortem Fractography	124
●	Discussion	124
●	Comments (Boeing)	127
6.0	TASK 5 VERIFICATION AND DEMONSTRATION ON FAILED COMPONENTS	129
6.1	JVX V-22 Osprey Full Scale Wing Test Box	135
6.1.1	Nondestructive Evaluation	135
6.1.2	Materials Characterization	140
6.1.3	Fractography	143
6.1.4	Stress Analyses	145
6.2	NASA HiMAT Wing	145
6.2.1	Nondestructive Evaluation	147
6.2.2	Materials Characterization	151
6.2.3	Fractography	151
6.2.4	Stress Analyses	156
6.3	Carbon Fiber Reinforced Plastic I-Beam	156
6.3.1	Nondestructive Evaluation	156
6.3.2	Materials Characterization	160
6.3.3	Fractography	165
6.3.4	Stress Analyses	165

7.0 CONCLUSIONS	167
8.0 GLOSSARY	171

LIST OF ILLUSTRATIONS

Figure		Page
1	Program Task Interrelationships	3
2	Singular and Multiple Failure Condition	
	Test Specimen Matrix (3 Sheets)	16
3	Basic Modes of Loading Involving Different Crack Types and Surface Displacements (<i>Interlaminar and Translaminar</i>)	19
4	The Interlaminar Mixed Mode Flexural Specimen Geometry (57% Mode I, 43% Mode II)	23
5	Crack Lap Shear (CLS) Specimen Geometry and Loading Conditions	23
6	Through-Transmission Ultrasonic Scan of a Quasi-Isotropic Laminate Following Impact Testing	26
7	Compression After Impact Test Fixture with Specimen in Place . . .	26
8	Optical Photomicrographic of Fiber End Fractures (Translaminar Tension, 0/90, 180°F Dry)	30
9	Optical Photomicrograph of Intralaminar Fracture Area (Translaminar Tension, 0/90, 180°F Dry)	30
10	Low Magnification SEM Fractographs Illustrating Variation in Fiber Pullout with Temperature for 0/90-deg Laminates	31
11	Low Magnification SEM Fractographs Illustrating Variation in Fiber Pullout with Temperature for +45/-45-deg Laminates	33
12	Low Magnification SEM Fractographs Illustrating Variation in Fiber Pullout with Temperature for Quasi-Isotropic Laminates . . .	34
13	SEM Fractographs Illustrating the Direction of Individual Fiber Breakage for Each Environmental Dry Condition (0/90 Layup)	35
14	SEM Fractographs Illustrating the Direction of Individual Fiber Breakage for each Environmental Dry Condition (+45/-45 Layup)	36
15	SEM Fractographs Illustrating the Direction of Individual Fiber Breakage for each Environmental Dry Condition (Quasi-Isotropic Layup)	37
16	Low Magnification SEM Fractographs Illustrating Environmental Wet, 0/90, Tensile Failures	39

17	Low Magnification SEM Fractographs Illustrating Environmental Wet, Quasi-Isotropic Tensile Failures	40
18	Low Magnification SEM Fractographs Illustrating Environmental Wet, +45/-45 Tensile Failures	41
19	SEM Fractographs Illustrating the Direction of Individual Fiber Fractures for Environmental Wet, 0/90, Tensile Failures	42
20	SEM Fractographs Illustrating the Direction of Individual Fiber Fractures for Environmental Wet, Quasi-Isotropic Tensile Failures	43
21	SEM Fractographs Illustrating the Direction of Individual Fiber Fracture for Environmental Wet, +45/-45, Tensile Failures	44
22	Low Magnification SEM Fractographs Illustrating Similar Appearances of Translaminar Compression Fracture at Different Temperatures for 0-deg Laminates	46
23	Low Magnification SEM Fractographs Illustrating Similar Appearances of Translaminar Compression Fracture at Different Temperatures for 0/90-deg Laminates	47
24	Low Magnification SEM Fractographs Illustrating Similar Appearances of Translaminar Compression Fracture at Different Temperatures for Quasi-Isotropic Laminates	48
25	Low Magnification SEM Fractographs of Translaminar Compression Fractographs at Different Temperatures for +45/-45-deg Laminates	49
26	SEM Fractographs Illustrating Similar Appearances of Translaminar Compression Fracture at Different Temperatures for 0-deg Laminates	50
27	SEM Fractographs Illustrating Similar Appearances of Translaminar Compression Fracture at Different Temperatures for 0/90-deg Laminates	51
28	SEM Fractographs Illustrating Translaminar Compression Fracture Appearances at Different Temperatures	52
29	SEM Fractographs Illustrating Similar Appearances of Translaminar Compression Fracture at Different Temperatures for +45/-45-deg Laminates	53
30	Low Magnification Fractographs of 0-deg Laminate Compression Failures Produced at 70°F, 180°F and 270°F, Wet	55

31	Low Magnification Fractographs of Quasi-Isotropic Laminate Compression Failures Produced at 70°F, 180°F, and 270°F, West	56
32	Low Magnification Fractographs of 0/90-deg Laminate Compression Failures Produced at 70°F, 180°F, and 270°F, Wet	57
33	Low Magnification Fractographs of +45/-45-deg Laminate Compression Failures Produced at 70°F, 180°F, and 270°F, Wet	58
34	SEM Fractographs of 0-deg Laminate Compression Failures Produced at 70°F, 180°F, and 270°F, Wet	59
35	SEM Fractographs of Quasi-Isotropic Laminate Compression Failures Produced at 70°F, 180°F, and 270°F, Wet	60
36	SEM Fractographs of 0/90-deg Laminate Compression Failures Produced at 70°F, 180°F, and 270°F, Wet	61
37	SEM Fractographs of +45/-45-deg Laminate Compression Failures Produced at 70°F, 180°F, and 270°F, Wet	62
38	SEM Fractographs Illustrating Morphology of 70°F, Dry, 0/90-deg Laminate Rail Shear Failure	64
39	SEM Fractographs Illustrating Morphology of 70°F, Dry, Quasi-Isotropic Laminate Rail Shear Failure	65
40	Low Magnification Fractographs Illustrating Morphology of Quasi-Isotropic Rail Shear Failures Produced at -65°F, 180°F, and 270°F, Dry	66
41	Low Magnification Fractographs Illustrating Morphology of 0/90-deg Rail Shear Failures Produced at -65°F, 180°F, and 270°F, Dry	67
42	Low Magnification Fractographs Illustrating Morphology of Quasi-Isotropic Rail Shear Failures Produced at -65°F, 180°F, and 270°F, Wet	68
43	Low Magnification Fractographs Illustrating Morphology of 0/90-deg Rail Shear Failures Produced at -65°F, 180°F, and 270°F, Wet	69
44	Detailed Fracture Characteristics of Quasi-Isotropic Rail Shear Laminates Failed at -65°F, 180°F, and 270°F, Dry	70
45	Detailed Fracture Characteristics of 0/90-det Rail Shear Laminates Failed at -65°F, 180°F, and 270°F, Dry	71
46	Detailed Fracture Characteristics of Quasi-Isotropic Rail Shear Laminates Failed at -65°F, 180°F, and 270°F, Wet	72
47	Detailed Fracture Surface Characteristics of 0/90-deg Rail Shear Laminates Failed at -65°F, 180°F, and 270°F, Wet	73

48	Mixed Mode Fracture Morphology for 0-deg Laminate	75
49	SEM Fractographs Illustrating Mixed Mode Fracture of 0/90-deg Laminate	76
50	SEM Fractographs Illustrating Mixed Mode Fracture of 0/45-deg Laminate	77
51	SEM Fractographs Illustrating Mixed Mode Fracture Morphology Characteristic of +45/-45-deg Laminate	78
52	Schematic Showing Formation of Reverse Crack Directions Due to Out-of-Plane Crack Divergence and Subsequent Crack Tip Bridging	81
53	Optical Photomicrographs of Fatigue Crack Growth Region for the 0/0 Interface Mode I DBC Specimen	83
54	SEM Photomicrographs of Typical Fatigue Striation Formation of Mode II CLS Specimen	84
55	High Magnification SEM Photomicrographs of Regions That Exhibit Faint Striations	85
56	Optical Photomicrographs of Intended Fracture Plane Between 0-deg Plies for the CLS Fatigue Specimen (100x and 1000x)	87
57	Optical Photomicrographs of Intended Fracture Plane Between 0-deg Plies for the CLS Fatigue Specimen (100x and 400x)	88
58	Optical Photomicrographs of Intended Fracture Plane Between 0/90-deg Plies for the CLS Fatigue Specimen	89
59	SEM Photomicrographs of Effect of Tilt on Striation Resolution (5000x)	91
60	SEM Photomicrographs of Effect of Tilt on Striation Resolution (500x and 5000x)	92
61	SEM Photomicrographs of Typical Fatigue Striation Formation of Mode II CLS Specimen	93
62	Overall Macrographs of Laminate Flexure Specimens (100x and 400x)	95
63	Macrograph of Fracture Surface from the Unidirectional 0-deg Laminate Flexure Specimen	95
64	SEM Photomicrographs of Unidirectional 0-deg Laminate Flexure Specimen	96
65	Photomacrographs of 0/90 Laminate Flexure Specimen	98

66	Interlaminar Fracture Surface Characteristics of the 0/90 Laminate Flexure Specimen	99
67	Optical Photomicrographs of Cross Sections from the +45/-45 Laminate Flexure Specimen	101
68	Overall Photomacographs of the Fastener-Filled-Hole Tension and Compression Specimens Following Testing	103
69	Damage to Fastener-Filled-Hole Tension and Compression Specimen	104
70	Edge View of Fastener-Filled-Hole Tension and Compression Specimens	105
71	Visual and Optical Details From the Drill Breakout Specimen	107
72	SEM Photomicrographs of Typical Delamination Surface Features for the Drill Breakout Specimen	108
73	Typical Fracture Surface Morphology of Void Defect Specimens ...	109
74	Typical Fracture Surface Morphology of Teflon Defect Specimens	111
75	Typical Fracture Surface Morphology of Frekote Defect Specimens	112
76	Through-Transmission Ultrasonic Scan of Compression After Impact	114
77	Typical Optical Fractographs Taken from Excised Delamination Surfaces of Compression After Impact Specimen	115
78	Typical Crack Directions Observed on Compression After Impact Panel Using Optical Fractography	117
79	Mode I Delamination (Wedge)	119
80	Mode II Delamination (Cracked End)	119
81	Mode I In Situ Delamination (Damage Zone)	121
82	Mode II In Situ Delamination (Three Stages)	122
83	Mode II In Situ Delamination (Hackle Formation)	123
84	Interlaminar Mode I Postmortem Fractography	125
85	Mode II Postmortem Fractography (Hackle Formation)	126
86	Detailed Failure Analysis Logic Network (FALN)	130
87	Nondestructive Evaluation Sub-FALN	131
88	Material Verification Technique Sub-FALN	132
89	Fractography Diagnostic Technique Sub-FALN	133
90	Stress Analysis Sub-FALN	134

91	Central Portion of JVX V-22 Central Wing Test Box	136
92	JVX Wing Test Box Upper Skin Surface	137
93	JVX Wing Test Box Inner Side of Upper Skin Surface	138
94	JVX Wing Test Box Front and Rear Spars	139
95	JVX Wing Test Box Lower Skin Surface	141
96	Ultrasonic C-Scan of Upper Skin Surface	142
97	JVX Wing Test Box Crack Mapping Results	144
98	NASA HiMAT Test Wing in the As-Received Condition	146
99	Upper Skin Inboard Edge Damage	148
100	NDE Results of the Lower Surface	149
101	NDE Results of the Upper Surface	150
102	Fiber Identification by Surface Analysis	152
103	Photomicrograph of Cross-Section Damage Zone B	153
104	Cross Section Illustrating Boron Fiber Misalignment Resulting in Resin-Rich Adjacent Regions	154
105	Photomacrograph of Beach Marks Indicative of Cyclic Crack Growth and Crack Propagation Direction	155
106	Fractography Results From NASA HiMAT Wing	157
107	Crack Mapping Results From Selected Delamination Regions	158
108	CFRP I-Beam in the As-Received Condition	159
109	Regions of (a) Compression Buckling and (b) Delamination in the Cap Section of the I-Beam	161
110	Another View of (a) Compression Buckling and (b) Delamination in the Cap Section of the I-Beam	162
111	TTU C-Scans of the I-Beam Subcomponents	163
112	Extensive Porosity and Laminate Deformity in the Web-to-Cap Junction	164
113	Results of Fractographic Crack Mapping of an Upper Cap Delamination	166

1.0 INTRODUCTION AND OBJECTIVES

The need to develop a comprehensive postfailure analysis capability for composite materials has become apparent in recent years. With the increasing use of these materials in aerospace applications, unanticipated failures under full-scale test conditions as well as in service are more likely to occur. This likelihood makes it necessary to develop the technology (or capability) to identify the causes and understand the circumstances of such failures, so that improvements to future designs can be made or appropriate corrective actions taken.

The steps for determining the causes of component failure in metallic structures are well established. Not only do postfailure investigators have a well-established protocol, but they can also draw on a battery of recognized analytical methods. Unfortunately, that was not the case with composite materials. Neither a well accepted protocol, such as a failure analysis logic network (FALN), or a set of analysis methods existed to determine failure causes for composite materials.

This program was specifically aimed at correcting that situation. The Air Force overall multiyear/multiprogram objective is to establish a widely disseminated and generally accepted "Composite Structure Failure Analysis Handbook" - or the equivalent for composite materials of such metal books as the Air Force sponsored "Electron Fractography Handbook" and the American Society for Metals (ASM) "Failure Analysis and Prevention" handbooks. While this program did not produce the fully comprehensive handbook, it has produced the "Compendium of Post-Failure Analysis Techniques for Composite Materials" (AFWAL-TR-86-4137), which should provide a strong basis for the handbook.

To provide the basic technology required for successfully carrying out a composites postfailure analysis investigation, this program consisted of three primary objectives:

- Establish, verify, compile, and demonstrate techniques and procedures for the postfailure analysis of graphite/epoxy structures.
- Define a logical investigative sequence, using the above procedures, that identifies the starting point, mode, and reason for in service failures.
- Establish a compendium that summarizes the techniques and investigative procedures defined above.

To achieve these objectives, the existing program has been restructured as follows:

- Task 1—Literature search and diagnostic technique evaluation.
- Task 2—Specimen production and test.
- Task 3—Diagnostic technique evaluation.
- Task 4—Creation of a failure analysis compendium.
- Task 5—Evaluation and documentation of techniques.

These tasks and their interrelationships are schematically illustrated in figure 1. Tasks 1 through 3 address the compilation and review of the various diagnostic techniques and protocols available, then select and evaluate their overall utility and effectiveness on test specimens made to fail under controlled conditions. The resulting compendium (task 4) provides a listing of the techniques and procedures found to be applicable in tasks 1 through 3. This compendium is presented in an instructional format and includes example data/information as well as appropriate FALNs to guide investigators along a logical analysis path. In task 5, the techniques and procedures developed within tasks 1 through 3 were applied to three failed components selected and submitted by the Air Force.

This final report completes all technical efforts within this program. Results from all efforts are included, with a brief description of research covered in the interim report, and a detailed description of studies encountered in the latter half of this program. Significant features are as follows:

- A review of existing technical literature.
- Detailed failure analysis logic networks (FALNs).
- Descriptions of specimen test procedures for the generation of controlled fractures for complex failure conditions.
- Fractographic findings for specimens failed under both simple, singular failure conditions and complex failure conditions.
- Results of failure analyses for the three failed components, demonstrating the developed failure analysis capability gained within this program.
- Results of in situ SEM analysis of interlaminar fracture, performed under subcontract by Texas A&M University.

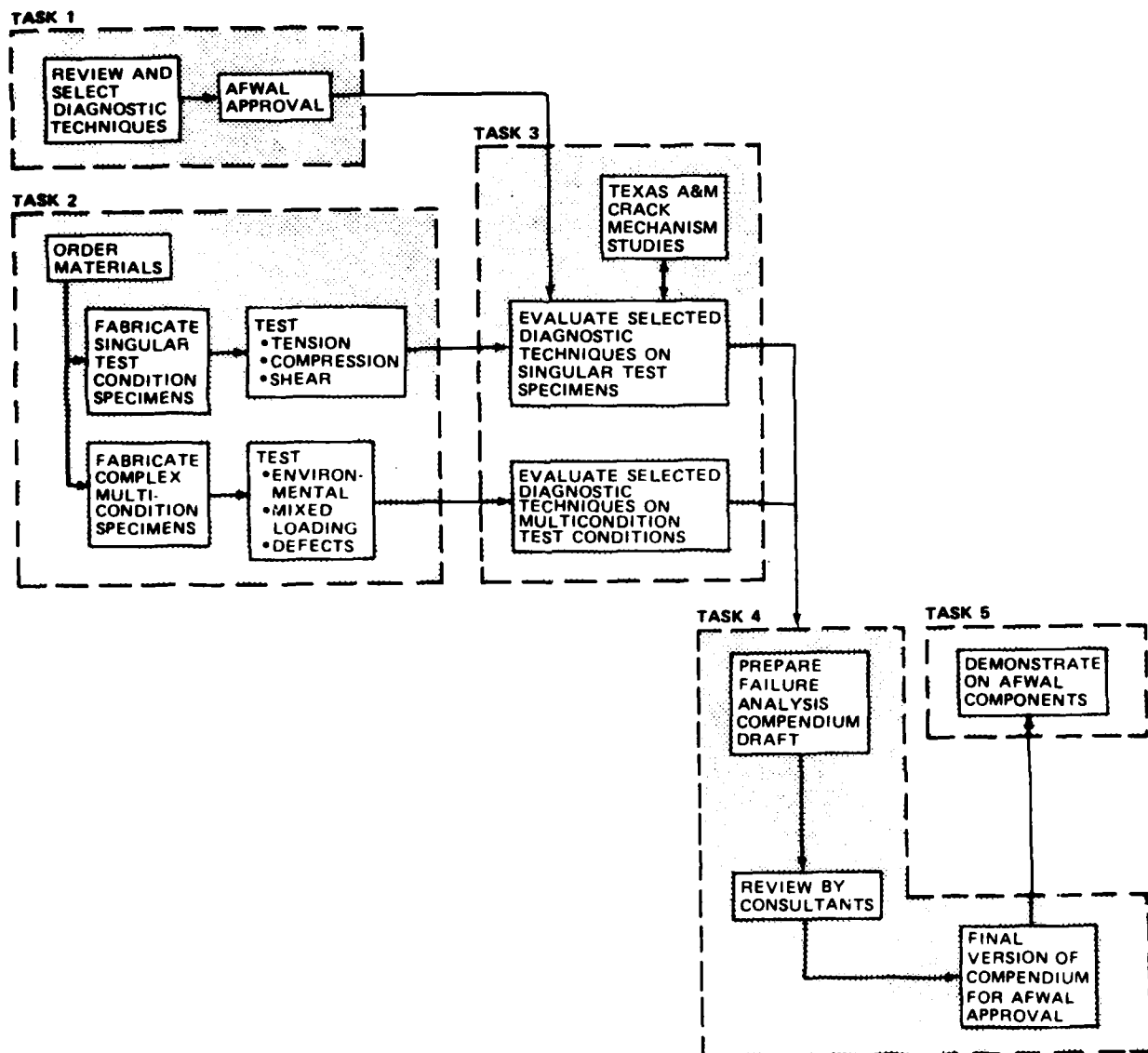


Figure 1. Program Task Interrelationships

6-B70236-001

2.0 APPROACH

This program was structured to produce a Compendium of Post-Failure Analysis Techniques for Composite Materials, along with several supporting examples of its application and effectiveness. The fundamental approach was to use the existing Boeing expertise along with pertinent scientific literature, and then, through a series of five tasks, identify, evaluate, summarize, and demonstrate the techniques and procedures necessary for a rudimentary failure analysis. The tasks were as follows:

- Task 1—Literature search and diagnostic technique evaluation.
- Task 2—Specimen production and test.
- Task 3—Diagnostic technique evaluation.
- Task 4—Creation of a failure analysis compendium.
- Task 5—Evaluation and documentation of techniques.

Figure 1 illustrates the specific interrelationships of these tasks, with Boeing experience forming the basic foundation at program start. In general, comprehensive failure analysis has been hampered by a lack of clearly defined information requirements. Research, while moving forward, has not always addressed large scale in service failures or the needs of the failure analyst. Because Boeing has been involved in composite failure analyses since 1977, that experience provided an initial model defining the necessary requirements, techniques, and procedures.

Tasks 1 through 3 systematically identified, reviewed, and evaluated diagnostic techniques necessary for a failure analysis.

Task 1 compiled diagnostic techniques from the available literature for: (1) direct incorporation into the final compendium, (2) additional study, or (3) elimination. Because many of the techniques for performing a failure analysis already existed, the literature review represented a logical starting point; it included nondestructive evaluation, stress analysis, materials characterization, and fractographic analysis techniques. Task 1 also involved on site visits with specific experts to further define existing capabilities available from the scientific community.

Those techniques selected for further study were evaluated in tasks 2 and 3 by examining pedigree specimens that failed under tightly controlled conditions. These studies were carried out on a model state-of-the-art carbon fiber/350°F curing epoxy

system (Hercules 3501-6 resin with AS4 fibers) in order to provide standard baseline data.

Information generated by tasks 1 through 3 provided the majority of information necessary to establish a Compendium of Post-Failure Analysis Methods for Composite Materials (Task 4). This compendium assembled the diagnostic techniques and FALNs into an instructionally oriented failure analysis form. The diagnostic techniques and interpretive skills developed in tasks 1 through 3 were evaluated by performing analyses of three failed components during task 5. The exercises within task 5 evaluated the investigative sequence, as well as the fractographic, nondestructive, and materials characterization techniques examined and developed in this program.

3.0 RESULTS

The following paragraphs briefly describe the results of tasks 1 through 5 during the performance of this program. More detailed descriptions of program results are provided in sections 4.0, 5.0, and 6.0, which present research findings obtained since the interim reporting period.

3.1 TASK 1—LITERATURE SEARCH AND FALN DEVELOPMENT

The objectives of this task were twofold: first, to review existing diagnostic techniques and identify those of potential value for composite materials failure analysis, and second, to organize these techniques into a logical framework describing their sequence of use. The framework considers the type of information obtainable by each technique, its value, and its relationship to other techniques.

Literature published from 1978 to the present was reviewed to identify existing diagnostic techniques for composite failure analysis. These documents addressed four general areas: (1) nondestructive evaluation, (2) stress analysis, (3) fractography, and (4) materials characterization. A total of 286 abstracts were identified, and 58 papers were examined.

Well-developed diagnostic techniques were identified for both nondestructive evaluation and materials characterization. In both these areas, there were many techniques that were sufficiently mature for direct incorporation into the "Compendium of Post-Failure Analysis Techniques for Composite Materials." However, in fractography and stress analysis, the information available from the literature search was insufficiently developed or documented for direct incorporation.

In the case of stress analysis, most of the surveyed literature focused on simple specimens failed under idealized conditions. Such techniques generally assumed relatively simple failure criteria and were capable only of roughly approximating the load at failure. Consequently, while it is reasonable to assume that these techniques might be improved to deal adequately with inservice failures, the accuracy, documentation, and degree of detail in current stress analysis literature is inadequate for direct incorporation into a useful compendium.

In the area of fractography, the situation was similar. Again, a significant portion of the literature reviewed relatively small coupons failed under ideal conditions, although some documents dealt with methods for analyzing larger, full-scale coupons. In general, while the available literature on fractography makes an important contribution to the understanding of fractures, it did not appear sufficiently complete to be directly incorporated into the final compendium. Detailed findings of the literature review have been presented in the interim report.

Under task 1, the Boeing initial FALN was reviewed, updated, and expanded. This FALN delineated the logical sequence of investigative operations required for carrying out a failure analysis, and described when and where to employ nondestructive evaluation, stress analysis, materials characterization, and fractography. This framework was based upon well-established procedures utilized in the failure analyses of metallic structures. It considered each major failure category, potential interrelationships, and the prevention of premature destruction of evidence. It was organized in a manner which emphasized the initial use of simple, inexpensive examinations followed by progressively more detailed analyses at later stages. Because the FALN applied these techniques on a broad scale, four sub-FALN's were developed to describe the logical flow of analysis in greater detail for each major discipline (see section 6.0). To aid investigators in selecting the best techniques for these sub-FALN's, supporting charts were also developed under task 1. The charts (contained in the interim report) describe the uses, attributes, and drawbacks of the most useful analysis techniques.

3.2 TASK 2—PRODUCTION OF SPECIALIZED TEST SPECIMENS

The primary objective of task 2 was to design, fabricate, and test specimens until they failed under singular failure mode with known crack direction or under complex, multiple conditions. The task was divided into two subtasks, 2A and 2B. The first of these subtasks examined the simpler conditions of failure, whereas subtask 2B examined multiple, complex conditions.

In accordance with Boeing procedures, these specimens were cured at 177°C (350°F), and employed Hercules 3501-6 resin with AS4 fibers. Vendor tests of the materials were performed prior to fabrication to establish the pedigree of the material.

In addition to design and fabrication, specimen tests were completed for the subtask 2A (single failure mode) specimens during the interim reporting period. Four specimen configurations were tested, each of which was designed to provide control over the mode and direction of crack propagation. In the case of interlaminar fractures, failures were produced under Mode I (tension) conditions, using a double cantilever beam (DCB) specimen configuration. Failures under Mode II (shear) conditions were produced using an end-notch flexural (ENF) specimen geometry. Controlled fractures through the laminate thickness (translaminar) were generated using notched-beam flexure for Mode I (tension and compression) and notched rails for Mode II (shear). As part of subtask 2A, specimens were also tested at under the following conditions.

<u>Conditions</u>			
<u>Dry</u>		<u>Wet*</u>	
<u>C°</u>	<u>F°</u>	<u>C°</u>	<u>F°</u>
-54	-65	21	70
21	70	82	180
82	180	132	270
132	270		

*The wet specimens were preconditioned at 71°C (160°F) and 100% relative humidity (condensing) environmental soak to an absorbed moisture content of 1.0% by weight.

During this final reporting period, specimen tests were completed for the subtask 2B (complex failure mode) specimens. Seven primary test specimen types were designed and tested to study the effects of operative failure causes, such as:

- Contaminants.
- Voids.
- Multiple load conditions.
- Mixed mode delaminations.
- Mechanical/inservice damage.
- Structure specific geometries.
- Environmental exposure.

Where possible, specimen configurations were tested to provide control over the mode and direction of crack propagation. For instance, the first four operative failure causes

listed above were produced under interlaminar Mode I and Mode II conditions, utilizing the DCB and ENF specimen configurations, respectively. The last three operative failure causes were produced with a wide variety of specimen configurations (that is, compression after impact, drill breakout, fastener-filled-tension, and laminate flexure). Each of the task 2B specimens were considered successful in generating the intended operative type of failure.

3.3 TASK 3—DIAGNOSTIC TECHNIQUE EVALUATION

3.3.1 Results Prior to Interim Report

This task established and evaluated the fractographic means for identifying the direction and mode of crack propagation, and contributing conditions such as environment, defects, or other factors, involved in failure. During the earlier interim reporting period, interlaminar Modes I and II, and translaminar Mode I tension and compression failures were examined. For each of these fractures, a variety of analytical methods for identifying the direction and mode of failure were evaluated. Consistent with the failure analysis logic networks developed under task 1, this task employed both optical and scanning electron microscope (SEM) analysis methods for examining these relatively simple singular failure conditions.

Through extensive analyses of over 500 specimens in this program, sound evidence supported the use of low magnifications investigations wherever possible. Particularly for inspection of delamination surfaces, the optical microscope provided significantly more information in a given timeframe than the SEM. Crack mapping and fracture mode determinations can be performed two or three times faster with the optical microscope; therefore, the amount of surface area and thus the reliability of the data can be greatly increased. The SEM has proven itself as a unique and powerful instrument, with primary advantages over the optical microscope for topographically rough fracture surfaces (translaminar) or high magnification inspection of fine details (fiber ends, striations, etc.).

Detailed examinations of interlaminar and translaminar singular fracture mode failures revealed significant differences in fracture characteristics.

Interlaminar Mode I fractures were relatively easy to identify and analyze. For this mode of failure, the direction of crack propagation could be discerned by examining the direction of cumulative river mark coalescence or detailed resin microflow. Mode I failures were easily identified by their consistently flat planar fracture topography.

Interlaminar Mode II (shear) fractures typically exhibited a rougher and more complex appearance than those noted under Mode I (tension). Because of their more complex appearance, it was more difficult to determine the crack propagation direction of Mode II fractures. For crossply layups (ply orientations other than 0/0-degree), the tilt of the fractured epoxy platelets or hackles were aligned in the direction of crack propagation. However, for 0/0-degree ply layups, the hackles were aligned roughly parallel to the crack, but are oriented both toward and away from the direction of crack propagation, and therefore do not reliably indicate crack growth direction.

Translaminar Mode I fractures are easily identified by extensive fiber pullout and the distinctively radial morphology of the fractured fiber ends. This radial morphology indicates the local direction of fiber end fracture. The cumulative direction of these individual fiber end fractures corresponded to the direction of crack growth.

Translaminar compression fractures typically exhibited extensive fracture surface damage and fiber microbuckling. Though this mode was relatively easy to identify, no combination of discrete features was found that could be used to clearly determine the direction of crack propagation.

3.3.2 Results Since Interim Report

During this final reporting period, efforts were completed for subtasks 3A and 3B. Subtask 3A work involved a continuation of efforts initiated earlier in this program (reported in the interim report), including translaminar Mode I and Mode II fractures (four-point side notched and the rail shear specimens, respectively). Subtask 3B research included fractographic analysis of more complex failures involving structural and defect conditions. For each of these fractures, a variety of analytical methods for determining the direction and mode of failure were evaluated. Consistent with the failure analysis logic networks previously developed under task 1, this task employed both optical and scanning electron microscope (SEM) analysis methods for examining both the simple (task 3A) and complex (task 3B) failure conditions.

Detailed examinations of the task 3A translaminar fractures revealed significant variations in the appearance of the macroscopic and microscopic fracture morphologies. The four-point translaminar tension and compression specimens that were subjected to a variety of environmental conditions exhibited the same basic features identified for room temperature dry fractures, except that more fiber-matrix separation was evident at conditions of elevated temperature and absorbed moisture. The rail shear translaminar Mode II specimens exhibited a failure morphology consisting of compression damage and fiber microbuckling. The appearance was different from compression Mode I fractures as evident by the much rougher overall topography, extensive amounts of protruding isolated fibers, and a slant type fracture at each individual fiber end.

Subtask 3B specimens involved two primary conditions of complex fracture, namely, structural/loading conditions and defect/contamination conditions. Detailed examination of the interlaminar mixed mode flexure specimens revealed a dominant morphology found on the Mode II shear interlaminar specimens. Hackles, scallops, and river marks were observed, with interfacial failure occurring by both mechanisms A and B, with the tilt of the hackles oriented parallel to the direction of induced propagation.

The interlaminar fatigue specimens exhibited the primary features representative of static type fractures. Microscopic striations were evident for both the Mode I and Mode II specimens, with striations located in the resin matrix fracture regions for the Mode I fractures, and striations located in the fiber-matrix separation regions for the Mode II fractures.

Laminate flexure specimens proved interesting in that pronounced differences in failure mode occurred for each specimen layup. Failure of the 0/90 and the quasi-isotropic laminated occurred along the tensile surface and involved both translaminar splitting and delamination. In contrast, failure of the unidirectional 0-degree specimen occurred through the full specimen thickness with very little delamination. Failure of the +45/-45 specimens occurred without any identifiable conditions of fracture, however cross sections showed localized minor internal cracking.

The drill breakout specimens exhibited extensive backside breakout damage. The backside delaminations exhibited mixed mode failure morphology (initiating at the bore edge) and machining debris was lodged into the delamination cracks.

Microscopic analysis of the interlaminar defect/contamination specimens exhibited unique and easily distinguishable features representative of defect conditions such as voids, Teflon, and Frekote. Each defect type exhibited localized regions which lacked resin fracture features, indicative of little or no fracture toughness.

The analysis of the compression after impact (CAI) specimens indicated that interpretive methods developed for the singular failure conditions were directly applicable to complex failure conditions such as CAI. By utilizing these methods, the microscopic load state of failure was identified and the point of origin was located.

In situ SEM studies were performed by Dr. Walter L. Bradley through a subcontract with Texas A&M. Real time and postmortem observations for both pure Mode I and Mode II delaminations indicate there is an extensive zone of microcracking in the resin ahead of the main crack tip (at least 90 μ m for Mode I and 200 μ m for Mode II). For each loading condition, cracking occurred by microcrack coalescence and interfacial debonding. Dr. Bradley's interpretations indicate that the orientation of hackles do not in any simple way relate to the direction of crack growth, and that the inclination of hackles relative to the plane of fracture is indicative of the fractional percentage of Mode II during the fracture process.

3.4 TASK 4—COMPENDIUM OF POST-FAILURE ANALYSIS PROCEDURES

This task provided a reference document which presents an overview of the analytical and diagnostic techniques that can be used to determine the causes of failure in continuous fiber reinforced composite materials. Such techniques included flow charts describing the logical arrangement of the investigative operations using fractography, materials characterization, nondestructive evaluation, and stress analysis as the primary diagnostic procedures. Interpretive methods are also presented to illustrate how to evaluate the information obtained during the application of the various analytical techniques. Finally, supportive data such as case histories of actual failure analyses and an extensive atlas of fractographs are included to provide a comparative reference source.

The Compendium has been provided to AFWAL as contract data requirements list (CDRL) item number six, and is considered as a precursor to a more comprehensive

handbook which will be generated through Air Force Contract numbers F33615-86-C-5071 (Boeing) and F33615-87-C-5212 (Northrop).

3.5 TASK 5-VERIFICATION AND DEMONSTRATION OF THREE FAILED COMPONENTS

The objectives of task 5 were to demonstrate and evaluate the FALN and various analytical techniques, as well as the overall capability to adequately define the cause of failure. During the performance of this task, the causes of failure of three composite structural components were successfully determined. The FALN and the various analytical techniques developed within this program were used to identify the sequence of failure, the origin locations, the loading conditions, the effect of material deficiencies or environmental influences, and the direction of crack propagation for the following structural components:

- V-22 Osprey full scale wing test box.
- NASA HiMAT test wing.
- I-beam.

4.0 TASK 2—SPECIMEN FABRICATION AND TESTING

4.1 OBJECTIVES

The objectives of task 2 were to design, fabricate, and test specimens to failure under singular and multiple causative conditions, producing both simple and complex fractures. This task was divided into two subtasks that reflect the division of specimen types. Under subtask 2A, specimens were designed, fabricated, and tested to create fractures under controlled conditions of crack propagation, direction, mode, origin, and environment. In task 2B, complex failure specimens were designed, fabricated, and tested to study the effects of:

- Contaminants.
- Voids and porosity.
- Mechanical damage.
- Inservice damage.
- Structure specific geometric configuration.
- Multiple load conditions.

The interim report covered all of the testing for subtask 2A. The following discussion reviews the pedigree of the materials used, specimen fabrication for tasks 2A and 2B, and the test history of subtask 2B specimens.

4.2 GENERAL APPROACH TO TASK 2

For task 2, there were two sets of specimens, namely, those failed by a singular cause (subtask 2A) and those failed under multiple conditions (subtask 2B). Figure 2 summarizes the test matrix and test geometries used in these subtasks. In subtask 2A singular-failure-mode specimens were designed to create the Mode I and Mode II failure circumstances illustrated in figure 3. The specimens fabricated for subtask 2A differ from the typical ultimate strength test specimens used in some failure analysis investigations in that they are specifically designed to generate well characterized sites of failure initiation, crack propagation, and failure mode. The effect of varying fiber orientations on failure characteristics was assessed by testing a variety of layups and interfacial ply orientations. For all specimens in this program, the 0-degree plies were oriented along the longitudinal axis. In the case of interfacial failures, five interfacial orientations were examined: 0/0, 0/90, 0/45, +45/-45, and 90/90 degrees (indicating the

SPECIMEN*	PLY LAYUPS, NUMBER OF PLIES, deg	COMMENTS	NUMBER OF SPECIMENS	SPECIMEN CONFIGURATION, cm (in.)
TASK 2A SINGULAR FAILURE-CONDITION SPECIMENS				
INTERLAMINAR • Mode I: DCB	24.0 24 ± 45 24.0.45° 24.0.90° 24.90°	• Will use 0-deg plies for buildup • short crack stability anticipated	5 each	
INTERLAMINAR • Mode II: ENF	24.0 24 ± 45 24.0.45° 24.0.90° b	• Will use 0-deg plies for buildup • cannot be tested in shear	5 each	
TRANS-LAMINAR				
• Mode I: tension four point load	- 32 ± 45 32/quasi	32.0.90	-	
• Mode I: compression four point load	32.0 32 ± 45 32 quasi	32.0.90	-	
• Mode II: side-notched rail shear	- - 32/quasi	32.0.90	-	
INTERLAMINAR				
• Mode I: DCB	24.0 24 ± 45 24.0.45	24.0.90	24.90	Water content measured 2 weeks soak at 82°C (180°F)
• Mode II: ENF	24.0 24 ± 45 24.0.45	24.0.90	-	Environmental matrix
TRANS-LAMINAR				
• Mode I: tension four point load	32.0 32 ± 45 32/quasi	32.0.90	-	132°C (270°F) dry, wet
• Mode I: compression four point load	32.0 32 ± 45 32/quasi	32.0.90	-	82°C (180°F) dry, wet
• Mode II: side-notched rail shear	32.0 32 ± 45 32/quasi	32.0.90	-	21°C (70°F) dry, wet
				.54°C (65°F) dry

*DCB: double cantilever beam, ENF: end-notched flexure, MMF: mixed-mode flexure, CLS: cracked-lap shear

Figure 2. Singular- and Multiple-Failure-Condition Test Specimen Matrix (Page 1 of 3)

SPECIMEN*	PLY LAYUPS, NUMBER OF PLIES, deg	COMMENTS	NUMBER SPECI-MENTS	SPECIMEN CONFIGURATION, cm (in.)	
				STRUCTURAL CONDITIONS	DEFECTS
TASK 2B MULTIPLE FAILURE CONDITION SPECIMENS					
INTERLAY/NAR	24.0	24.±45	240.45	240.90	-
• Mode I, MMF					Search
					1.27 (0.5)
				See Task 2A for specimen geometry: Mode I DCBs will be bonded to height-tapered beams	
• Fatigue	24.0	24.±45	240.45	240.90	-
• Mode DCB	24.0	24.±45	240.45	240.90	-
• Mode I, CS	24.0	24.±45	240.45	240.90	-
TRANSLAM/NAR					
• Laminate fracture	32.0	32 quasi	32/±45	320.90	-
• Fastener					Search
• Fired nose compression	-	32 quasi	-	-	-
• Fired-nose tension	-	32 quasi	-	-	Search
• Bulging stud w/ FEP insert	32/quasi	-	-	-	Search
• Bulging stud w/o FEP insert	32/quasi	-	-	-	Search
TASK 2B MULTIPLE FAILURE CONDITION SPECIMENS					
INTERLAY/NAR	32.0	32/quasi	32/±45	-	-
• Drill breakouts:					Search
					5.08 (2)
					2.54 (1)
	See Task 2A for specimen geometry			See Task 2A for specimen geometry	
• Fractile					Search
• Mode I, DCB	24.0	24.±45	240.45	240.90	-
• Mode I, ENF	24.0	32/±45	240.45	240.90	-

*DCB double cantilever beam; ENF end-notched flexure; MMF mixed mode flexure; CLS cracked lap shear

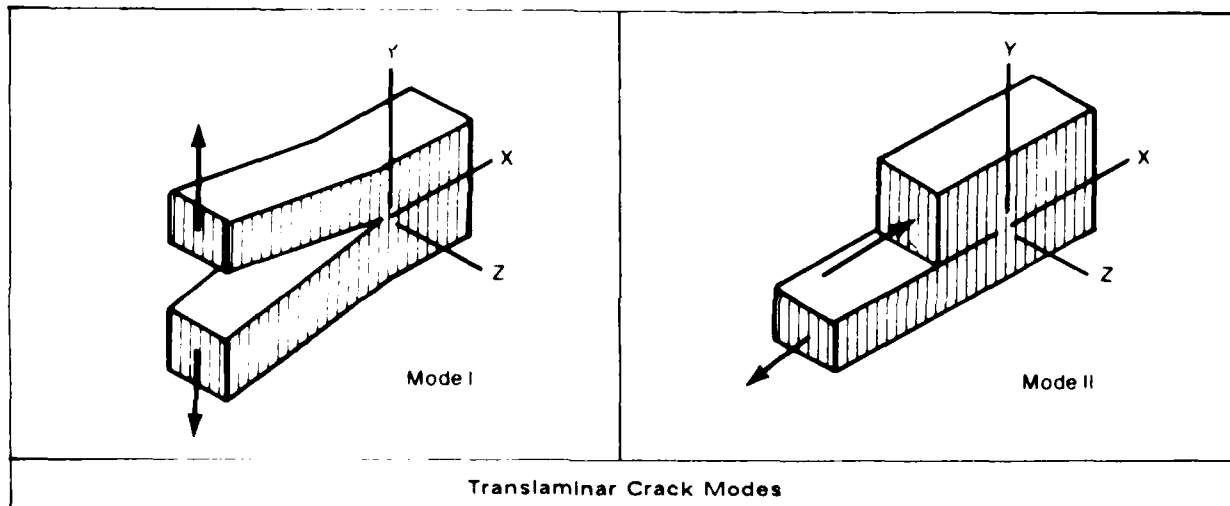
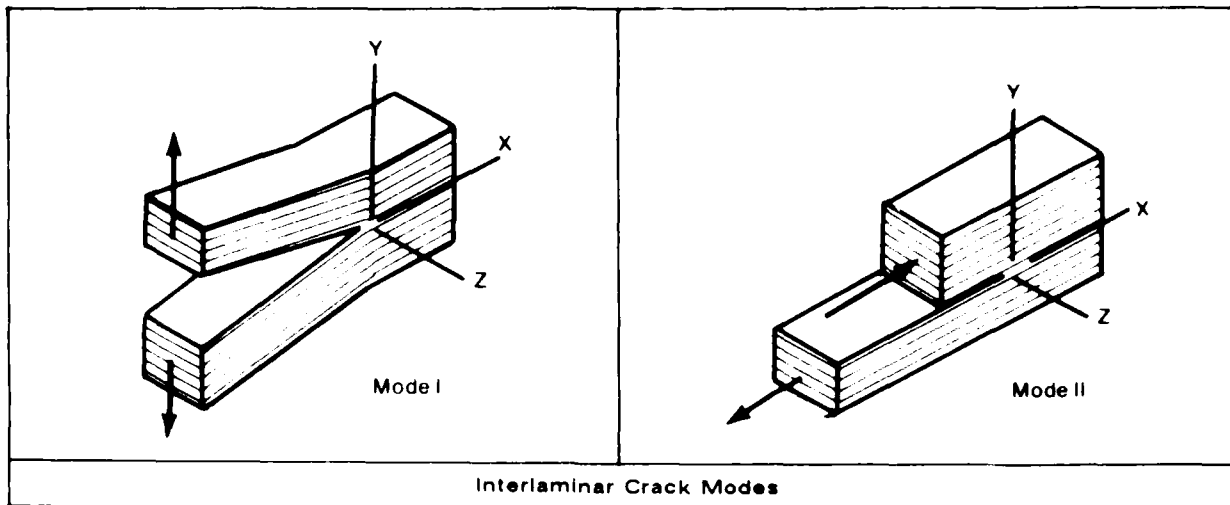
Figure 2 Singular- and Multiple-Failure-Condition Test Specimen Matrix (Page 2 of 3)

SPECIMEN*	PLY LAYUPS, NUMBER OF PLIES, deg	COMMENTS	NUMBER OF SPECIMENS	SPECIMEN CONFIGURATION, cm (in.)
TASK 2B MULTIPLE-FAILURE CONDITION SPECIMENS				
• 240 mm quasistatic				Drill breakout only; no mechanical testing required
• Mode DCB	24.0	24.0 ± 4.5	240.45	240.90
• Mode ENF	24.0	24.0 ± 4.5	240.45	240.90
• vCds				
• Mode DCB	24.0	24.0 ± 4.5	240.45	240.90
• Mode CLS	24.0	24.0 ± 4.5	240.45	240.90
• T-dac				
• Compression after impact	32 quasi	-	-	15.24 (6)

*DCB double cantilever beam ENF end-notched flexure. MMF: mixed-mode flexure. CLS: cracked lap shear

Figure 2 Singular- and Multiple-Failure-Condition Test Specimen Matrix (Page 3 of 3)

6-B70236-002



Denotes ply orientation

Mode I Opening or tensile mode, where the crack surfaces move directly apart

Mode II Sliding or in-plane shear mode, where the crack surfaces slide over one another in a direction perpendicular to the leading edge of the crack

Figure 3 Basic Modes of Loading Involving Different Crack Types and Surface Displacements (Interlaminar and Translaminar)

6-B70236-003

angular orientation of the plies between which delamination was produced). For example, 90/90 indicates a condition where interlaminar fracture was produced between two adjacent 90-degree plies. In the latter part of the subtask 2A, the effect of environmental conditions on fracture characteristics was assessed by testing at a variety of temperatures, both with and without absorbed moisture.

The task 2B specimens were designed to produce multiple failures while maintaining as much control as possible over the variables being analyzed. Two basic kinds of specimens were tested; specimens that use the singular-failure-condition configurations employed in subtask 2A (with the addition of fatigue and defect conditions), and specimens designed to create mixed loading and structural detail simulations that are complex in load state and application. By using these types of specimens, a set of failure types and modes were generated that, when analyzed in task 3, provided basic information concerning the effect of these multiple conditions and aided in verifying and evaluating the diagnostic techniques developed in subtask 3A.

4.3 MATERIAL PEDIGREE

Currently, a fairly wide variety of resin systems and fiber combinations exist for use in graphite/epoxy composite materials. However, due to the high performance demands of military and commercial aircraft structures, the types of available materials are limited to those systems that exhibit good environmental behavior, toughness, and high ultimate strength. These systems are typically 177°C (350°F) cured graphite/epoxy systems based on tetraglycidyl diaminodiphenyl methane-diaminodiphenyl sulfone (TGDDM-DDS) epoxy matrices, with or without BF₃-amine catalyst additions. For this program, Hercules 3501-6/AS4 carbon epoxy tape was selected.

To guarantee the pedigree of the material, the prepreg tape was purchased in accordance with XBMS 8-294, Type 1, Form I, Class 1, Grade 145. Basic properties were verified by vendor testing.

4.4 SPECIMEN FABRICATION

Specimens for subtask 2A and 2B were fabricated per Boeing process specification BAC 5562, in which panels were cured at 586 Pa (85 lb/in²) and 179°C (355°F) for 120 to 180 minutes, using a neutralized vacuum bag system.

Through-transmission ultrasonic (TTU) techniques were used to inspect each specimen for defects resulting from panel fabrication or subsequent machining. Those specimens with areas greater than approximately 0.322 cm^2 (0.05 in^2) that exhibited ultrasonic indications three levels higher (18 dB) than the baseline were rejected and scrapped. Over 97% of the fabricated specimens were found to be acceptable. In addition to ultrasonic inspection, representative samples from each of the panels were optically examined in cross section, and subjected to thermomechanical analysis (TMA). Optical microscopy of representative cross sections confirmed that the ply stacking sequence for all but one of the panels was correct. For this one panel, a plus 45-degree ply was inadvertently laid up with a minus 45-degree orientation. However, this error was considered inconsequential given the strictly fractographic aims of task 3. Additional microscopy evaluated defect conditions identified by TTU on rejected specimens. The TTU identified defects corresponded with matrix voids. The degree of panel cure was evaluated by determining the glass transition temperature of each panel by TMA in the flexure mode. All measured values were found to be typical of full cure and were judged acceptable.

4.5 ENVIRONMENTAL MOISTURE PRECONDITIONING

Moisture preconditioning of subtask 2A specimens, which required an absorbed moisture level at fracture, were placed in a 71°C (160°F), 100% relative humidity environment until a 1.0% moisture content by weight was achieved.

This moisture content was selected as representative of typical values that can be anticipated for long term inservice exposure. Moisture gain data gathered by NASA on ground rack exposed samples at various locations around the world have indicated a stable equilibrium value of about 1% for 3501 epoxy systems.

4.6 INTERLAMINAR MIXED MODE FLEXURE (MMF) TESTING

(0/0, 0/90, 0/-45, +45/-45, and 90/90 interfaces)

Interlaminar failures under a mixture of Mode I and Mode II conditions were produced by asymmetric loading of 1 by 10 mm \times 24 ply double cantilever beam specimens. In order to provide a known ratio of Mode I and Mode II, this asymmetry was produced by cutting only the outer edge of the double cantilever beam specimen at the fluorinated

ethylene propylene (FEP) insert end as shown in figure 4. This condition produces approximately 57% Mode I and 43% Mode II (based on elastic beam behavior). Cantilever support of the specimen during test was achieved by using the end-notch flexure (ENF) specimen fixture, which also provided freedom for the specimen to move laterally during test. In order to establish a relatively uniform rate of crack propagation, a variety of crosshead rates were utilized. In general, fracture of these specimens occurred in a controlled manner with fracture initiating at the FEP insert and progressing down the length of the specimen.

4.7 INTERLAMINAR FATIGUE TESTING (MODE I AND MODE II)

These tests were carried out utilizing the double cantilever beam (DCB) and crack lap shear (CLS) specimen geometries. The DCB Mode I specimen geometry was identical to that optimized earlier in the program for task 2A specimens. The CLS Mode II specimen geometry was selected to simulate primarily shear loading conditions. Although the load states are actually 80% shear and 20% tension, this specimen geometry has been proven by Boeing independent research and development (IR&D) studies to give well controlled crack growth under fatigue conditions. The CLS specimen dimensions are identical to that of the DCB specimen and the loading is presented in figure 5.

The DCB specimens were static load precracked with a mechanical testing systems (MTS) servohydraulic load frame until the crack extended about 2 in. The stroke was recorded at the maximum crack growth. Each specimen was then fatigued from 1 to 6 hz (depending on the span required). The first set of 3500 fatigue cycles was conducted between 40% and 90% of the specimen's maximum recorded stroke at failure and the second set of 3500 fatigue cycles was conducted between 10% and 60% maximum stroke.

The CLS specimens were static load precracked until the crack extended about 2 in. The ultimate load was recorded. Each specimen was then fatigued at 5 hz. The first fatigue set of 3500 cycles was conducted between 20% and 60% of the specimen's recorded ultimate load and the second fatigue set of 3500 cycles was conducted between 40% and 80% of ultimate load.

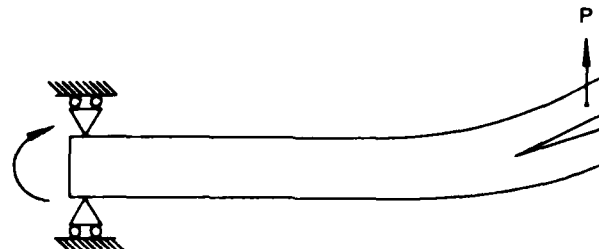
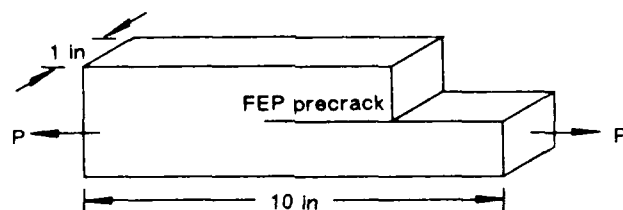


*Figure 4. The Interlaminar Mixed Mode Flexural Specimen Geometry
(57% Mode I, 43% Mode II)*

6-B70236R2-004



A shear stress gradient is generated at the crack tip so that cracking is driven from the FEP precrack toward the opposite end.

Figure 5. Crack Lap Shear (CLS) Specimen Geometry and Loading Conditions

6-B70236R1-005

4.8 LAMINATE FLEXURE TESTING

(0 Degree, Quasi-isotropic, 0/90, and +45/-45 Degree Layups)

Laminate flexure failures were produced under four-point bend. These 32 ply and 5- by 0.5-in specimens were loaded utilizing a 4.5-in span and 2-in center span. All testing was performed with a mechanical screw-driven Tinius Olsen machine at a load rate of 0.05 in/min. Failure of these specimens occurred catastrophically, with no visible identifiable origin or direction of crack propagation during the testing process.

4.9 FASTENER-FILLED-HOLE TESTING (TENSION AND COMPRESSION)

These tests failed a lap joint fabricated with 32 ply quasi-isotropic laminates bolted together with a single 3/16-in flush Hi-lok fastener. Testing was performed on a Tinius Olsen screw-driven test machine at 0.05 in/min. In order to prevent gross buckling, compression testing was carried out utilizing antibuckling restraining plates on both sides of the test specimen.

4.10 BUCKLING SPECIMEN TESTING (WITH FEP INSERT)

FEP insert compression tests were carried out by end loading each specimen while maintaining knife edge support along the unloaded specimen edges. These specimens were fabricated with a 1.5-in diameter FEP circular defect implanted at the approximate specimen center. Failure of this specimen was intended to produce a complex mixed mode delamination with a known point of origin. Testing of these specimens, however, failed to generate any delamination growth out of the central FEP defect region, as indicated by posttest TTU inspection. Catastrophic through-thickness fracture occurred at the loaded specimen end, approximately 0.1 in from the load platen. Since fracture did not occur in the vicinity of the implanted defect, the analysis of these specimens was not performed in task 3B.

4.11 DRILL BREAKOUT SPECIMENS

The drill breakout specimens were created by drilling a 0.24-in diameter hole in a 1- by 2-in, 32 ply quasi-laminate. Conditions of heavy drill force and lack of backside support material resulted in damage of the laminate on the drill exit side.

4.12 INTERLAMINAR DEFECT AND CONTAMINATION SPECIMENS

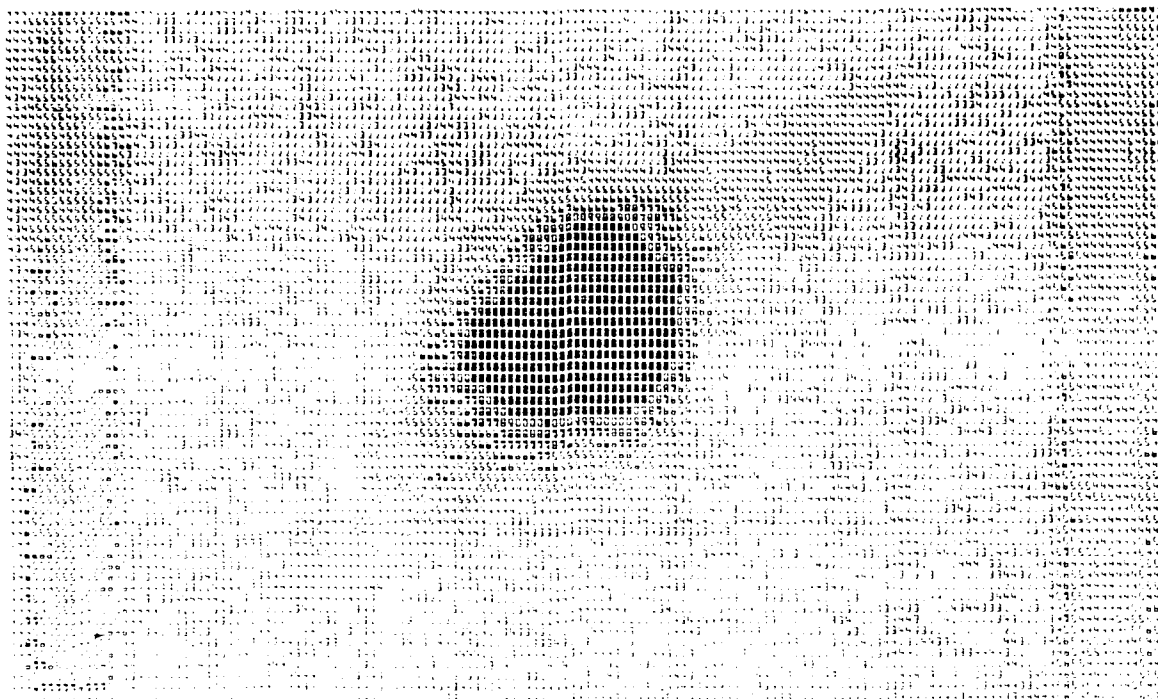
This involved creation of defect conditions of interlaminar Mode I tension (DCB) and Mode II shear (ENF) specimen geometries followed by fracture in the same test fixturing used for the task 2A singular failure mode testing. These test fractures were produced between 0/0, 0/90, +45/-45, and 0/45 ply orientations with the following defect conditions:

- Voids (due to lack of autoclave pressure).
- Frekote (applied to prepreg).
- Teflon (squeegee application).

Testing of these specimens produced zones of local crack plane divergence. However, as with the singular failure mode specimens, a sufficient amount of failure was produced between the planes of interest.

4.13 COMPRESSION AFTER IMPACT (CAI)

Compression testing was performed on 4- by 6-in quasi-isotropic laminates after impact testing. In order to provide visible surface damage and a critical level of internal damage, each specimen was impacted at 384 in-lbs at the approximate specimen center. Figure 6 illustrates the extent of internal damage generated as a result of impact testing. Compression failure after impact was produced by end loading the short dimension of the coupon, with edge fixity provided along all four sides by knife edge contact with a support jig (see figure 7). In general, buckling of these samples was observable at 80% to 90% of compression ultimate strength. However, fracture of the specimens typically occurred in a rapid and catastrophic manner, precluding visual identification of either the origin or direction of fracture during test.



The dark circular zone indicates the extent of delamination around the impact site.

Figure 6. Through-Transmission Ultrasonic Scan of a Quasi-Isotropic Laminate Following Impact Testing

6-B70236-006

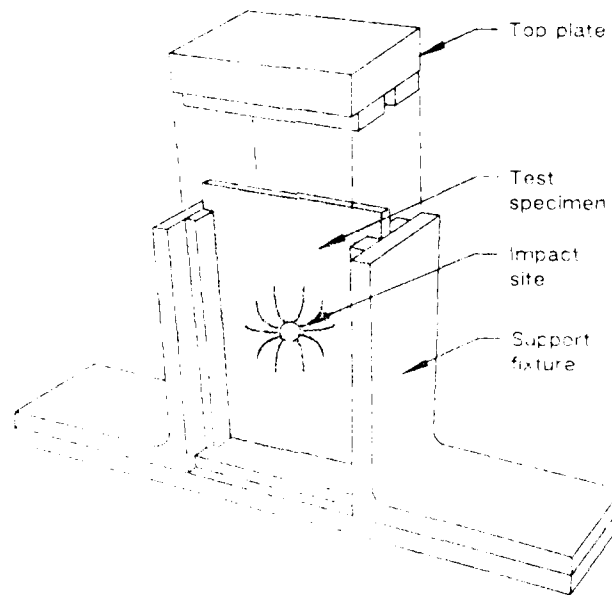


*Figure 7. Compression After Impact Test
Fixture With Specimen in Place*

6-B70236R1.7

5.0 TASK 3-DIAGNOSTIC TECHNIQUE EVALUATION

5.1 OBJECTIVES

Activities in task 3 were aimed at developing a detailed understanding of the fracture surface characteristics of composite materials. The literature search performed earlier in this program revealed that a number of investigations have been carried out to this end. However, since the overall objective of this program is the failure analysis of composite structures, effort was specifically devoted to understanding how fracture features relate to the direction of crack propagation, the load state at failure, and contributory factors such as environment, defects, and structural details. By understanding these relationships, physical evidence such as fracture features can be used by an investigator to reconstruct the order of events involved in component failure.

5.2 APPROACH

In task 3 the objective was to learn the basic relationship between fracture features and crack direction, load state, and environment by examining relatively simple specimens with well-controlled failure conditions. Using this approach, direct comparisons could be made between fracture features and simple failure conditions, thereby eliminating much of the complexity associated with most fractographic studies. After simple failure specimens were thoroughly characterized, a well-developed data base was generated, in which subtle changes in fracture features (likely to occur under more complex failure conditions) are more readily distinguishable. To understand these changes and to determine how the developed data base can be applied to real structures, the later stages of task 3 examined specimens with relatively complex modes of failure.

Task 3 has two subtasks, 3A and 3B. In subtask 3A, specimens with relatively simple modes of failure were examined with respect to crack direction, load state, and environment. During the previous report period nearly all of the specimens in this subtask were examined, and were reviewed in the interim report. In subtask 3B, specimens which were tested under relatively complex modes of failure were analyzed.

In examining the fracture surfaces of specimens failed during this program, a number of techniques were used involving examination at successively higher magnifications. Initial low magnification inspection was carried out from 8X to 40X on a Bausch & Lomb

stereo-zoom widefield microscope. Higher magnification inspections were performed on the majority of fractures at magnifications ranging from 50X to 400X using a Nikon Optiphot microscope fitted with long-working-distance objectives that give greater depth of field than other systems at equivalent magnifications. The finest fracture details were examined using an AmRay 1400 scanning electron microscope (SEM) at magnifications ranging from 20X to 20,000X.

Optical characterization of task 2 fractures contributed to a critical task 3 step in the development of a comprehensive failure analysis capability. Optical examinations of the characteristics of fracture identified specific features and morphologies that are valuable in performing failure analyses. Low magnification examinations verified the plane of intended interlaminar fracture, the location of visible macroscopic beach marks, and identified the local direction of crack propagation. More detailed examination using the Nikon Optiphot characterized specific fracture features with respect to their appearance, consistency over the fracture surface, and relationship with the imposed mode and direction of fracture. Correlation of these features with the crack direction and mode under which failure occurred is directed toward development of an optical fractography data base. In general, optical fractography is performed in metals fracture analysis as a means of rapidly identifying fracture origins and areas of further interest. Similar benefits will result from the development of a methodology in which optical analysis is used to analyze failed composite material structures.

Each fracture surface was characterized and inspected using an AmRay 1400 SEM with a beam acceleration voltage of 20 keV. This voltage was selected to enhance the resolution of shallow surface details such as resin microflow. Prior to examination, approximately 20 nm (7.9 by 10^{-7} in) gold-palladium was applied to the specimens in a Hummer V sputter coater. The coating was applied using the DC-pulsed mode for 5 min after backfilling the vacuum chamber with argon 4.0 to 6.6 Pa (30 to 50 millitorr). To provide a controlled point of reference, SEM examinations were performed at two standard tilt angles, 15- and 60-degrees. The 15-degree tilt was chosen to give a relatively flat perspective similar to that characteristic of optical microscope examinations. Sixty degree examinations revealed more of the dimension and height of specific features. In a manner similar to earlier optical examinations, photomicrographs with successively higher magnifications were taken to document the fracture topography and guarantee analysis of an area typical of the overall surface.

5.3 TRANSLAMINAR MODE I TENSION, ENVIRONMENTAL

This paragraph describes the results of optical and SEM characterization of the typical morphology of translaminar tension specimens failed under environmental conditions. The examination revealed increasing amounts of fiber pull out at elevated temperatures and absorbed moisture conditions. As with the room temperature tensile failures discussed in the interim report, these specimens were found to exhibit radial patterns on the fractured fiber ends and river marks on the localized intralaminar ply fracture regions. The specific morphology of these features were found to correspond with the direction of crack propagation.

Optical microscopic analyses of the fracture surface for these specimens revealed a mottled texture with no truly distinctive features (see figure 8). Part of the problem in optically examining these fibers occurs due to the limited depth of field of the optical microscope and the highly tiered structure characteristic of such fractures. In contrast, scanning electron microscopy of typical fiber fracture areas revealed a distinct radial morphology on the end of each fiber, as presented later in these paragraphs.

However, detailed optical inspections were carried out on the intralaminar fracture regions which were oriented at 90-degrees to the applied load axis. Plies oriented at 45-degrees could not be examined due to the irregularity of their fracture plane and objective clearance restrictions caused by crossply oriented fiber fractures. For the 90-degree plies, however, a distinct Mode I interlaminar tension morphology was observed. As shown in figure 9, matrix areas of these fractures exhibited pronounced river mark structures as well as less distinct conditions of microflow. With reference to the direction of induced cracking, these river markings were found to coalesce in the direction of crack growth, providing a positive means of identifying the direction of fracture progression.

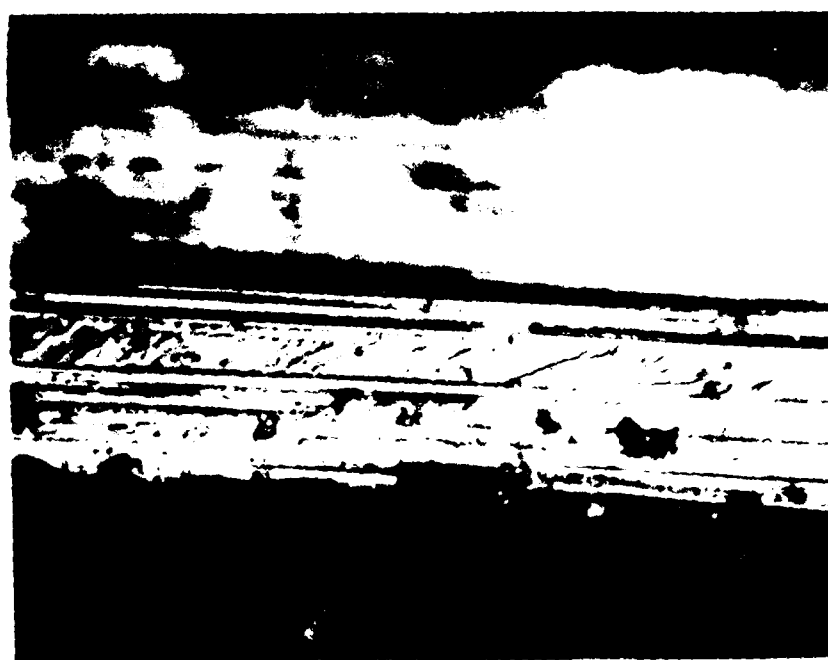
5.3.1 Temperature Extremes, Dry

For translaminar tension failures, alterations in the temperature of fracture were found to generate changes in the amount of fiber pull out. As illustrated for the 0/90 layup in figure 10, fracture at -65°F was found to produce relatively dense bundles of 0-degree fiber fracture. Fiber breakage within these bundles tends to occur along the same approximate plane. As a result, individual fiber pull out for this failure environment is



Figure 8. Optical Photomicrograph of Fiber End Fracture (Translaminar Tension, 0/90, 180°F Dry)

6-B70236-6



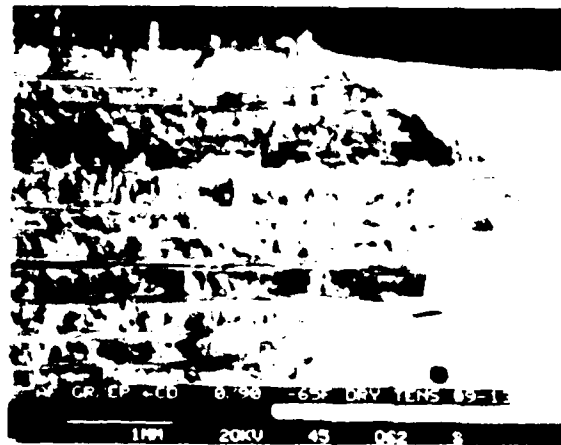
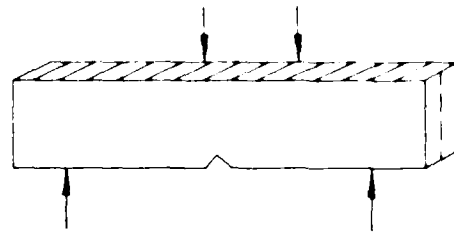
400X

Figure 9. Optical Photomicrograph of Intralaminar Fracture Area (Translaminar Tension, 0/90, 180°F Dry)

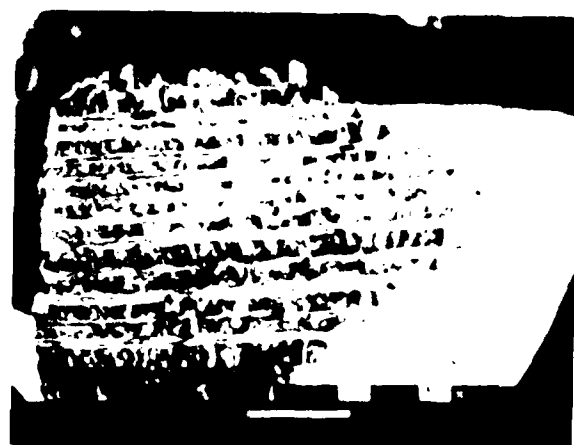
6-B70236-009

SEM photomicrographs

Fracture type	Translaminar mode I tension
Ply layup	[0 90] _{16S}
Test type	Four-point bend
• Test conditions	Dry
Material	Hercules 3501-6/177°C cure AS4 fibers

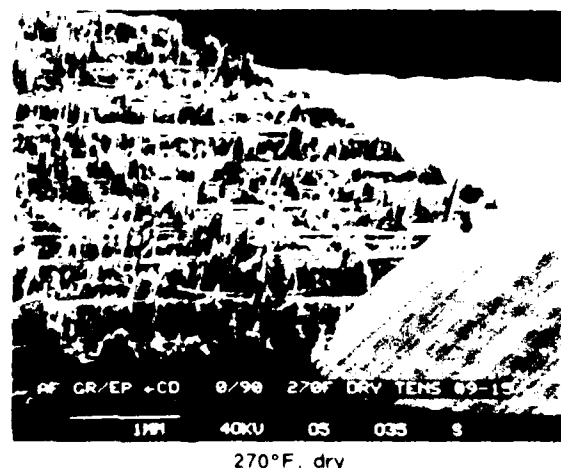


-65°F, dry



70°F, dry

Mechanically induced crack direction



270°F, dry

Figure 10. Low Magnification SEM Fractographs Illustrating Variation in Fiber Pullout With Temperature for 0/90-deg Laminates

relatively limited. This condition may be contrasted to that exhibited at 180° and 270°F in which extreme variations in the plane of fiber fracture occur. For these elevated temperatures, fiber bundle height appears characteristically irregular with each individual bundle also exhibiting a highly tiered structure. As particularly well illustrated at 270°F, extensive amounts of individual fiber pull out occur with up to 0.1-mm long sections of single fibers being visible in some cases. This structure tends to suggest that fracture at elevated temperatures occurs in a more discontinuous manner than that evidenced at colder temperatures.

As suggested by these findings, the trend towards increasing fiber-matrix separation may be due to either:

- Reduced fiber to matrix adhesion strength.
- Increased matrix ductility or toughness.
- Combinations of both of the above.

What is interesting is that these behaviors also appear to translate to 0/90 degree, +45/-45 degree (figure 11) and to a lesser extent, quasi-isotropic (figure 12) layups. This observation suggests that relative extremes in the environment prior to or during fracture may be identifiable for a variety of layups.

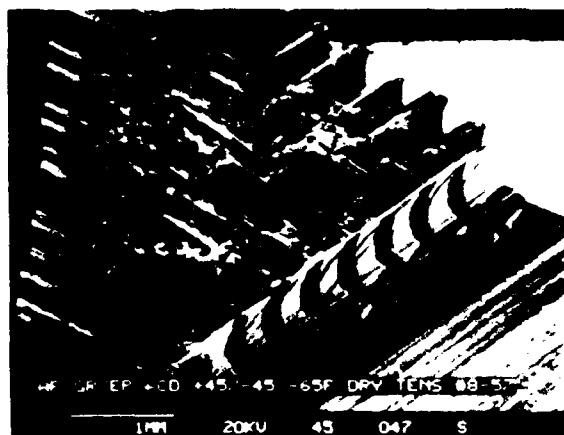
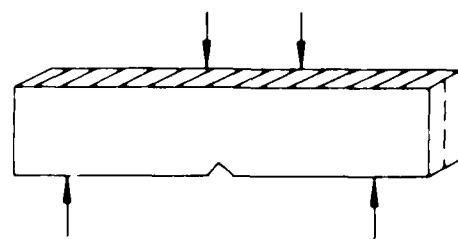
As described in the interim report, the direction of crack propagation for translaminar tensile fractures was found to be identifiable based upon the cumulative direction of individual fiber breakage. For failures produced at -65°F, 180°F, and 270°F dry, this crack mapping methodology was also found to work. Figures 13 through 15 illustrate the fiber end fracture morphologies of 0/90, +45/-45, and quasi-isotropic laminates failed at each of these temperatures. As shown, in each case the cumulative direction of fiber end fracture corresponds positively with the direction of induced failure. While this finding is encouraging in that it suggests that crack mapping is feasible for environmental conditions, it is somewhat surprising given the fracture surface roughness and extreme discontinuity evident at elevated temperatures.

5.3.2 Environmental Conditions (Temperature and Moisture)

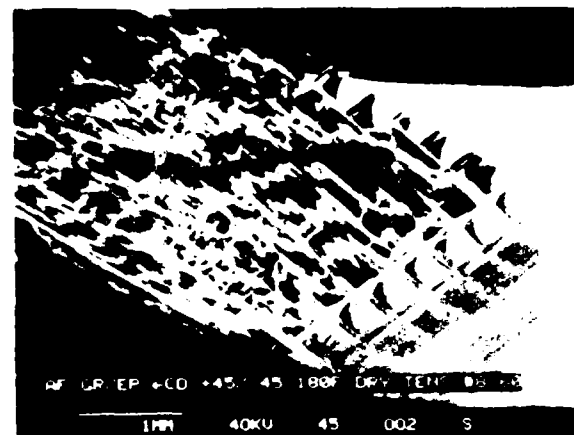
This paragraph describes the morphology and failure characteristics of environmental wet translaminar tension specimens.

SEM photomicrographs

Fracture type	Translaminar mode I tension
Ply layup	[+45, -45] 16S
Test type	Four-point bend
• Test conditions	Dry
• Fiber end fracture	
Material	Hercules 3501-6, 177°C cure AS4 fibers



-65°F, dry



180°F, dry

Mechanically induced crack direction



270°F, dry

Figure 11. Low Magnification SEM Fractographs Illustrating Variation in Fiber Pullout With Temperature for +45/-45-deg Laminates

SEM photomicrographs

Fracture type	Translaminar mode - tension
Ply layup	[0 - 45 - 90]s/s
Test type	Four point bend
• Test conditions	Dry
• Fiber end fracture	
Material	Hercules 7000 1170 cure AS4 fibers



-65°F, dry



180°F, dry

Mechanically induced crack direction



270°F, dry

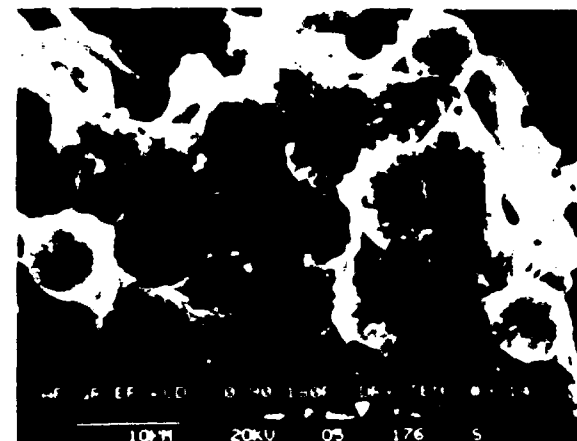
Figure 12 Low Magnification SEM Fractographs Illustrating Variation in Fiber Pullout With Temperature for Quasi-isotropic Laminates

6 870236 12

- Material Properties
 - Test Specimen Preparation
 - Test Procedure
 - Test Results
 - Test Evaluation
 Materials
 - Thermoplastic Polymers
 - Additives



65°F, dry



180°F, dry

Mechanically induced crack direction



270°F, dry

Figure 17. SEM micrographs showing the effect of temperature on the fracture surface after breaking at 0.5 in/min.

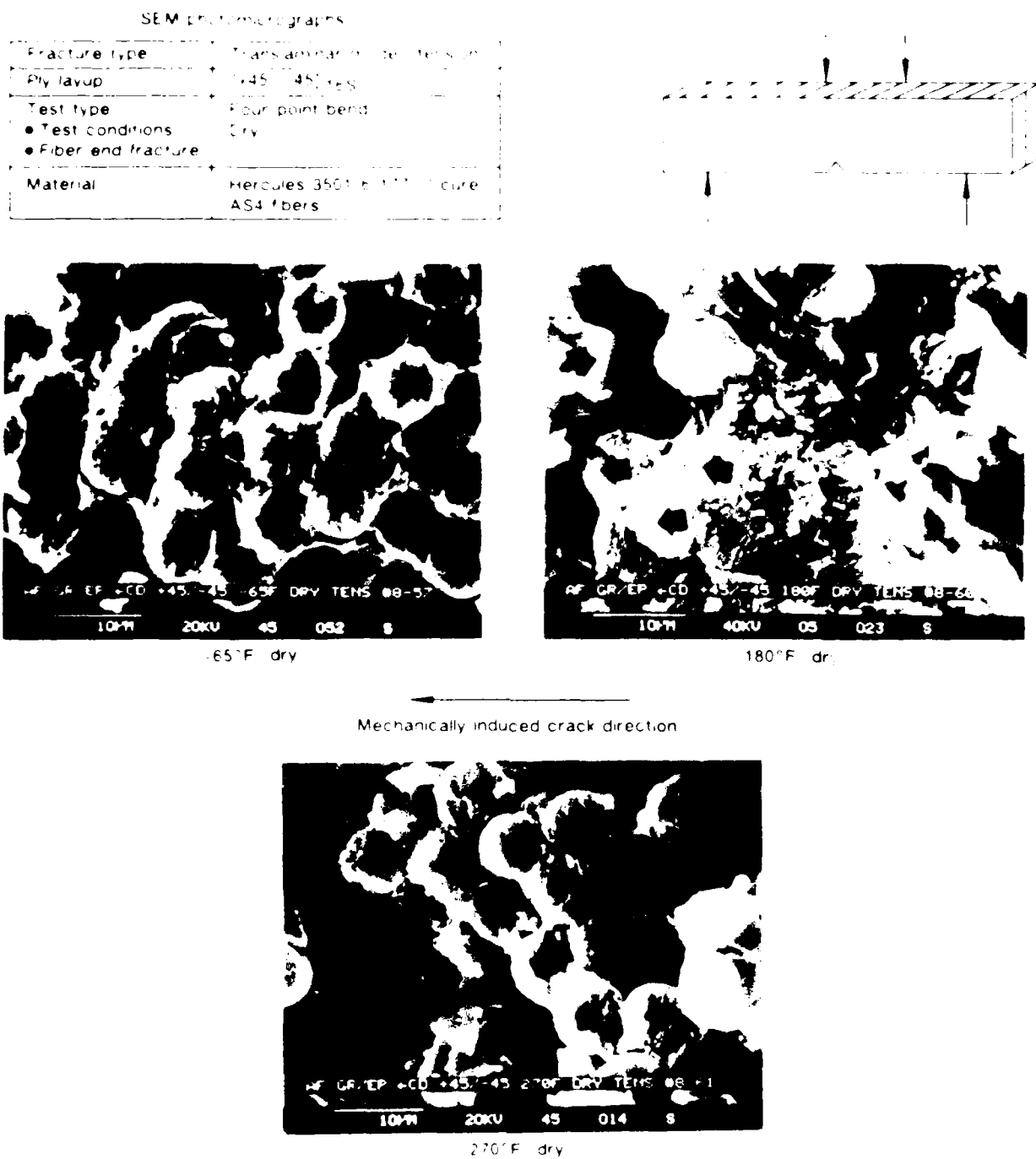
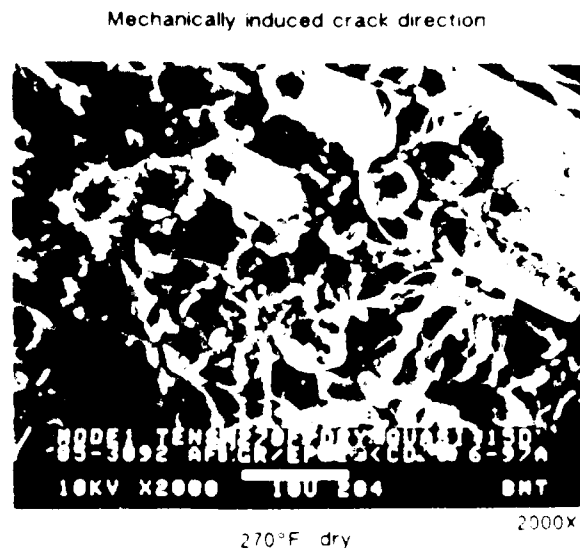
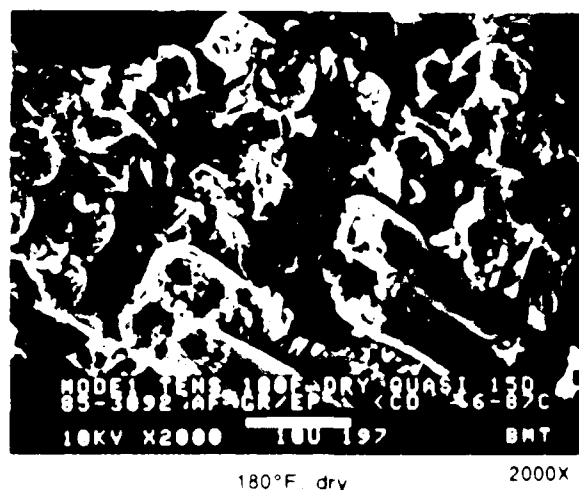
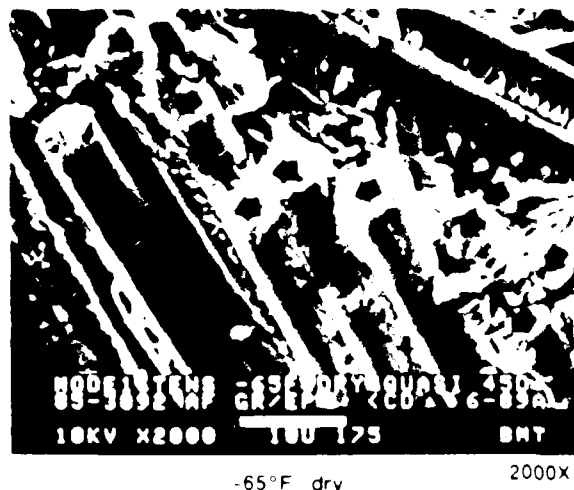
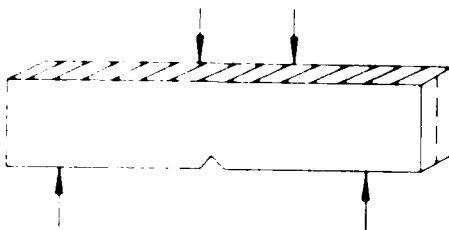


Figure 14 SEM Fractographs Illustrating the Direction of Individual Fiber Breakage for Each Environmental Dry Condition (+45/-45 Layup)

SEM photomicrographs

Fracture type	Translaminar mode I tension
Ply layup	[0 45 90]qES
Test type	Four-point bend
• Test conditions	Dry
• Fiber end fracture	
Material	Hercules 3501-6 177°C cure AS4 fibers



Mechanically induced crack direction

Figure 15 SEM Fractographs Illustrating the Direction of Individual Fiber Breakage for Each Environmental Dry Condition (Quasi-isotropic Layup).

Optical and SEM analysis of these specimens was aimed at, first, developing the ability to identify the environment at fracture, and second, verifying the ability to identify failure modes and crack directions for failures produced under a variety of conditions. Translaminar tensile failures produced under environmental wet conditions produced results strikingly similar to that noted previously for the environmental dry specimens discussed above. These specimens exhibited the following characteristics:

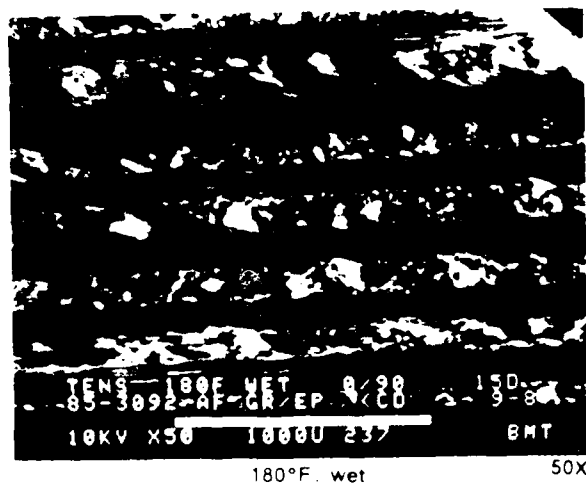
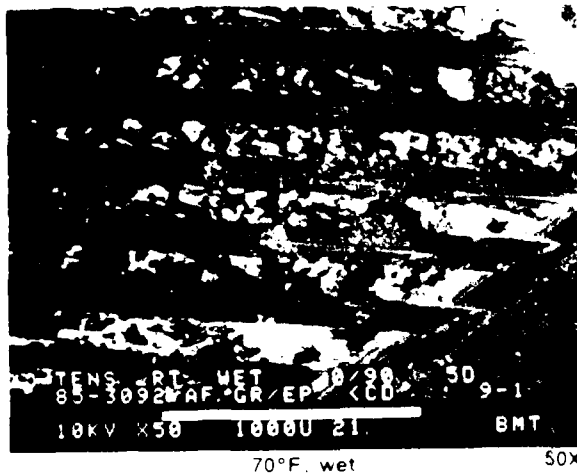
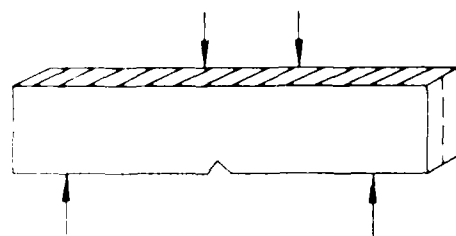
- Increased amounts of fiber pull out with increasing test temperature.
- Individual fiber fracture radials oriented in the direction of imposed crack growth despite the increase in fracture surface irregularity (relative to room temperature dry).

Figures 16 through 18 illustrate the gross morphology characteristic of 70°F, 180°F, and 270°F, wet, failures produced on 0/90, quasi-isotropic and + 45/-45 degree laminates. Tensile loading for each laminate produced two basic modes of ply failure, tensile fiber fracture and intralaminar delamination. Tensile fiber fracture represents the more interesting of these two modes. As illustrated for each laminate orientation, the amount of fiber pull out increases dramatically with elevated temperature. This condition is particularly well illustrated in figure 18 for the +45/-45 degree laminate. Typically, the amount of fiber pull out exhibited by both dry and wet conditioned specimens increased in about the same manner. As a result, while relative extremes in fracture temperature can be identified, conditions of absorbed moisture do not appear to be discernable.

As noted in the above paragraph, examinations of tensile specimens revealed that the cumulative direction of individual fiber fracture coincides with the direction of the imposed fracture independent of environmental conditions prior to, or during, the actual fracture event. Figures 19 through 21 illustrate the directions of individual fiber fracture for each of the subject layups examined. As shown, the general direction of individual fiber fracture was found to progress in the direction of imposed crack propagation. This behavior was most pronounced for failures produced at 70°F. Typically, the heavily tiered structure characteristics of fiber pull out made SEM mapping difficult due to the limited numbers of fibers visible within the microscope depth of field. This difficulty was partially overcome by utilizing a 50 μ m objective aperture, instead of the normal 200 μ m aperture to provide an increased depth of field. As illustrated, even with this heavily tiered structure, the direction of crack

SEM photomicrographs

Fracture type	Translaminar mode I tension
Ply layup	[0° 90°]S
Test type	Four-point bend
• Test conditions	Wet
• Fiber end fracture	
Material	Hercules 3501-E 177°C cure AS4 fibers



Mechanically induced crack direction

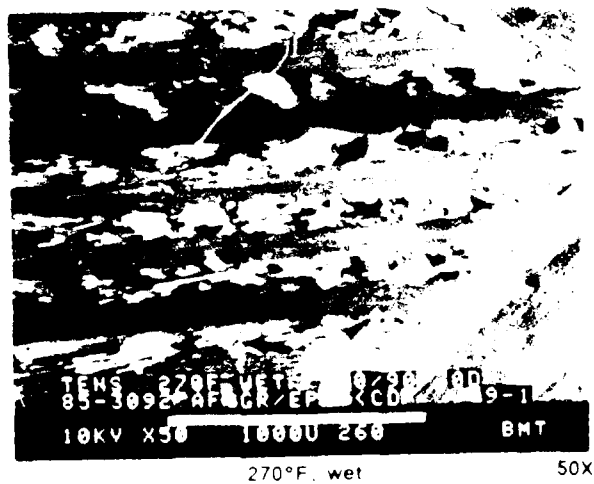
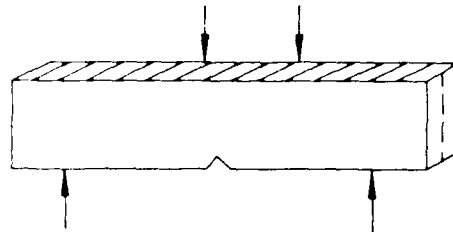


Figure 16 Low Magnification SEM Fractographs Illustrating Environmental Wet, 0/90, Tensile Failures

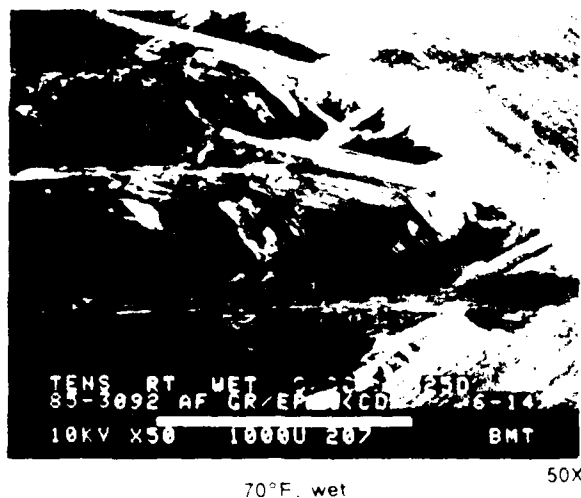
6-870236-16

SEM photomicrographs

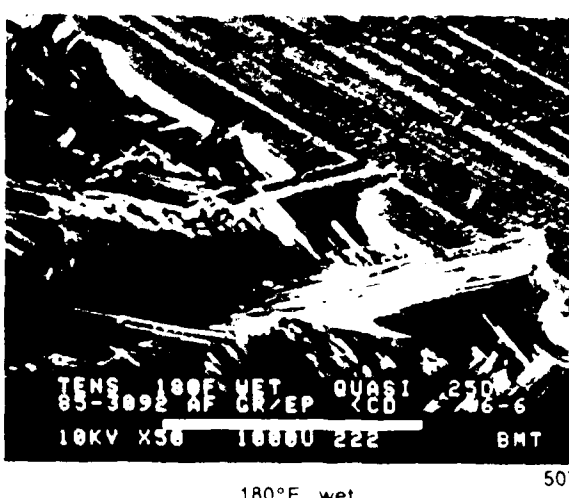
Fracture type	Translaminar mode I tension
Ply layup	[0, 45, 90] _{15S}
Test type	Four-point bend
• Test conditions	Wet
• Fiber end fracture	
Material	Hercules 3501-6 177°C cure AS4 fibers



Mechanically induced crack direction



50X



50X

Mechanically induced crack direction



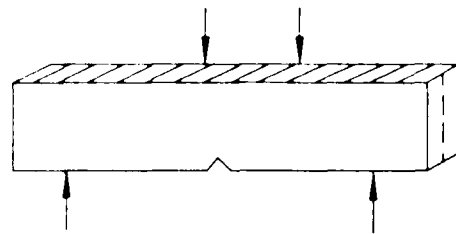
50X

Figure 17. Low Magnification SEM Fractographs Illustrating Environmental Wet, Quasi-Isotropic Tensile Failures

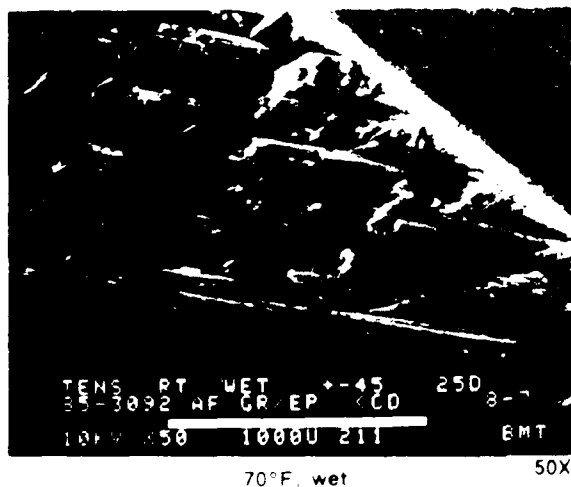
6-B70236-17

SEM photomicrographs

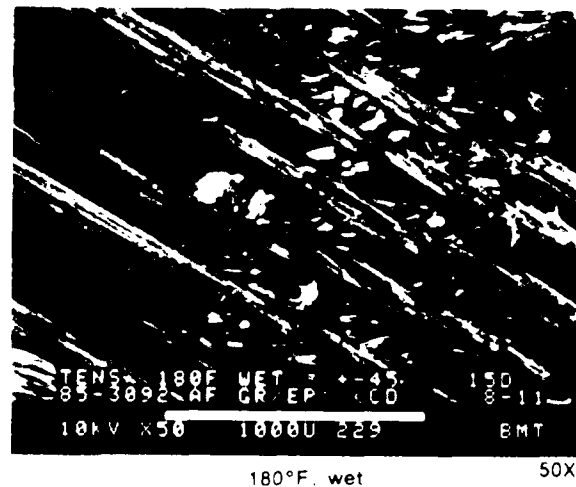
Fracture type	Translaminar mode I tension
Ply layup	[+45, -45] 16S
Test type	Four-point bend
• Test conditions	Wet
Material	Hercules 3501-6, 177 °C cure AS4 fibers



Mechanically induced crack direction



Mechanically induced crack direction



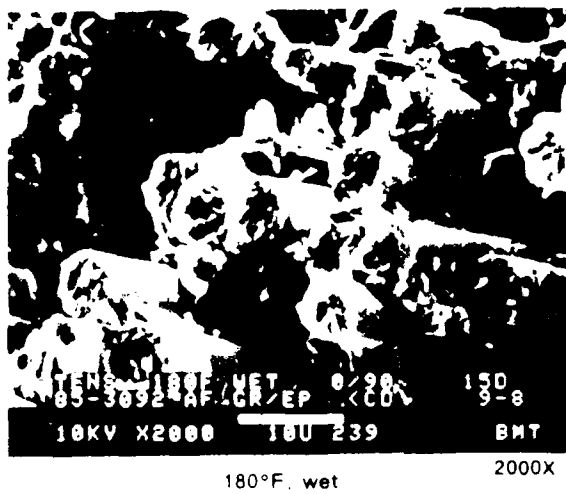
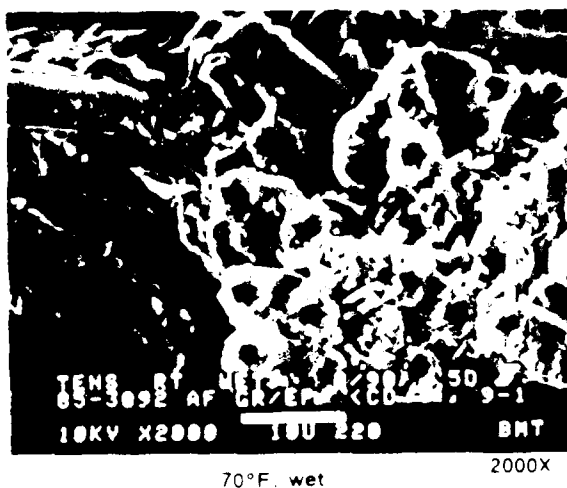
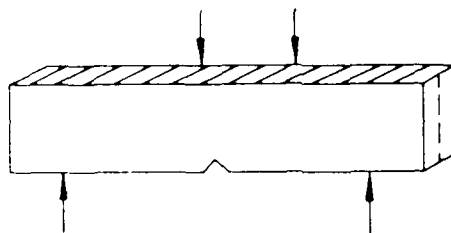
Mechanically induced crack direction



Figure 18. Low Magnification SEM Fractographs Illustrating Environmental Wet, +45/-45 Tensile Failures

SEM photomicrographs

Fracture type	Translaminar mode I tension
Ply layup	[0, 90] 16S
Test type	Four-point bend
• Test conditions • Fiber end fracture	Wet
Material	Hercules 3501-6 177°C cure AS4 fibers



Mechanically induced crack direction

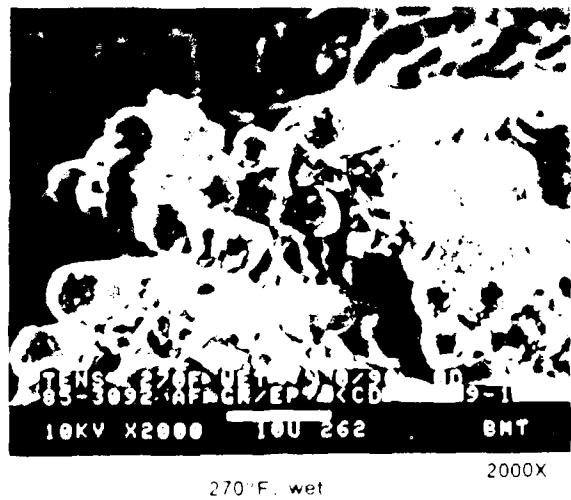
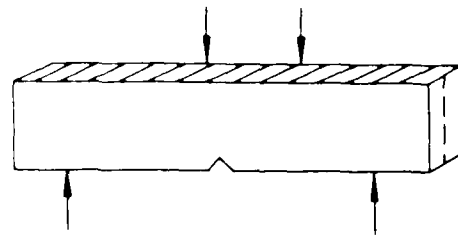


Figure 19 SEM Fractographs Illustrating the Direction of Individual Fiber Fractures for Environmental Wet, 0-30°, Tensile Failures

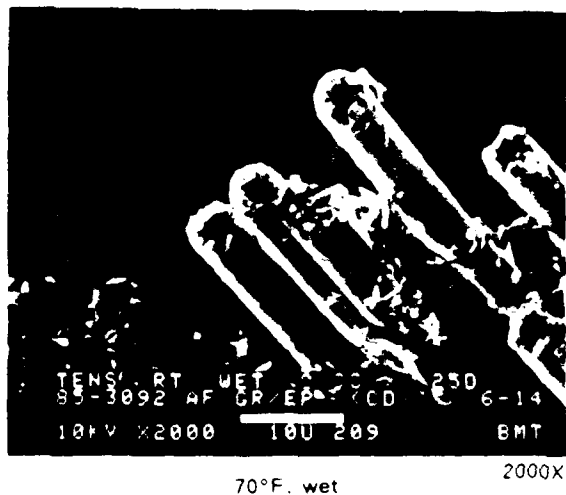
6-B70236-19

SEM photomicrographs

Fracture type	Translaminar mode I tension
Ply layup	[0, 45, 90] _{16S}
Test type	Four-point bend
• Test conditions	Wet
• Fiber end fracture	
Material	Hercules 3501-6 177°C cure AS4 fibers



Mechanically induced crack direction



Mechanically induced crack direction



Mechanically induced crack direction

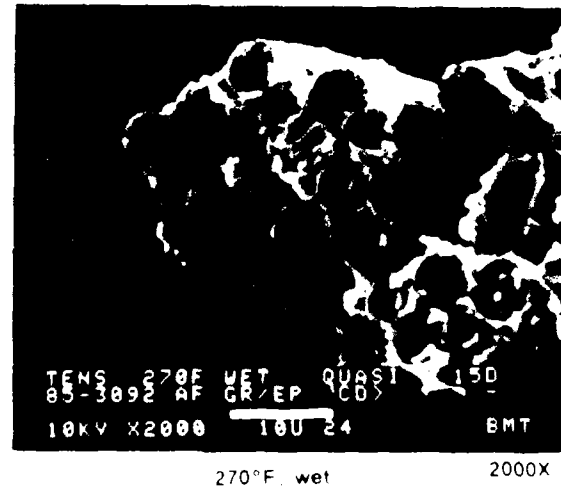
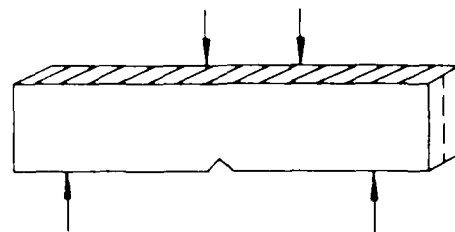


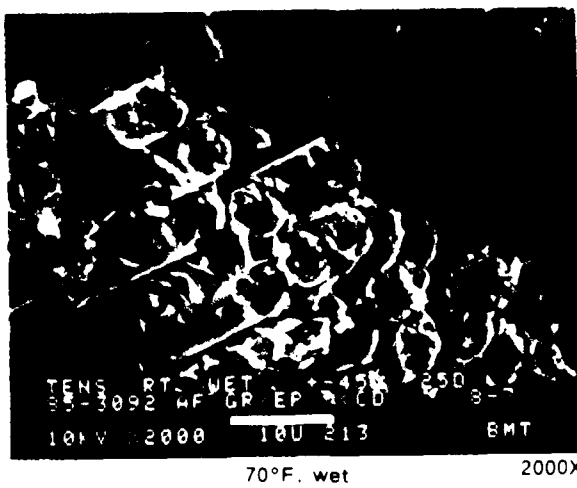
Figure 20. SEM Fractographs Illustrating the Direction of Individual Fiber Fractures for Environmental Wet, Quasi-Isotropic Tensile Failures

SEM photomicrographs

Fracture type	Translaminar mode I tension
Ply layup	[+45, -45] 16S
Test type	Four-point load Wet
Material	Hercules 3501-6 177°C cure AS4 fibers

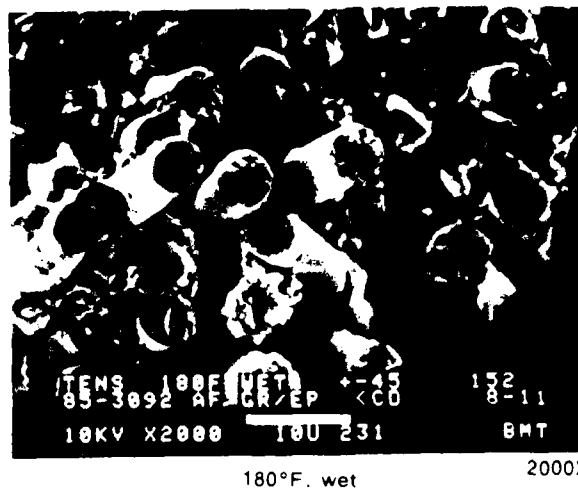


Mechanically induced crack direction



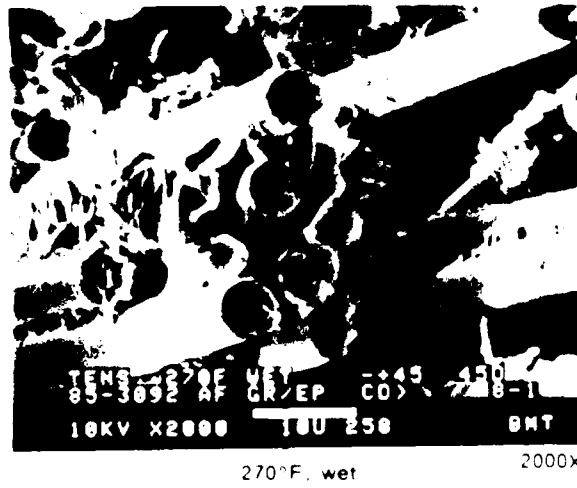
70°F, wet 2000X

Mechanically induced crack direction



180°F, wet 2000X

Mechanically induced crack direction



270°F, wet 2000X

Figure 21. SEM Fractographs Illustrating the Direction of Individual Fiber Fractures for Environmental Wet, +45/-45, Tensile Failures

propagation was found to be identifiable by examining the morphology of individual fiber fractures.

5.4 TRANSLAMINAR MODE I COMPRESSION, ENVIRONMENTAL

This paragraph describes the results of optical and SEM characterization of environmental compression specimens. As part of task 3, the analysis of these compression specimens which failed under different environmental conditions was aimed at developing the ability to identify the environment at fracture and verify the ability to identify failure modes and crack directions for failure under various environmental conditions.

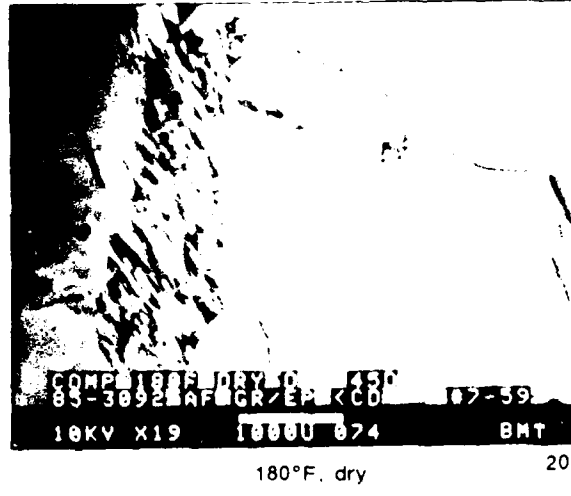
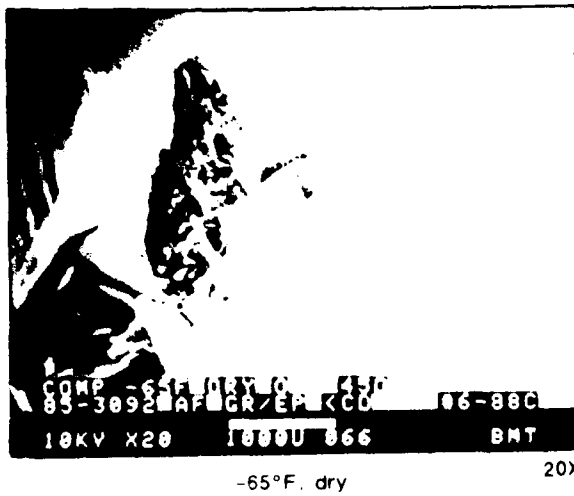
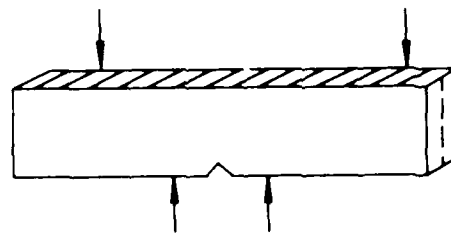
For translaminar compression fractures, failure under different temperature and absorbed moisture conditions was not found to produce any pronounced changes in fracture morphology. At low magnification each of the layups examined revealed a basic morphology consisting of distinct areas of tensile and compressive failure (see figures 22 through 25). Areas of compression fracture exhibited a flat, crushed morphology sharply contrasting the fibrous appearance of tensile fracture areas located near the end of this flexurally loaded specimen. As shown in these figures, variations in failure temperature from -65°F (-54°C) to 270°F (132°C) increased the relative size of compression fracture area but did not alter this basic morphology.

5.4.1 Environmental, Dry

These specimens were tested under various temperatures (-65° to 270°F), but were in the dry, as fabricated, state. Examination of environmental dry compression fractures at higher magnifications (see figures 26 through 29) revealed similar behaviors to that noted at low magnifications. In general, close inspection revealed that fracture occurs in a planar manner with groups of fibers failing under microbuckling induced flexure. One exception of note, however, is quasi-isotropic laminates failed at -65°F. As illustrated in figures 24 and 28 failure of this laminate produced very little compression fracture area. Usually the majority of fractures occurred by secondary tensile failure. As illustrated in figure 28 penetration of this secondary fracture into the compression loaded crack tip produced zones exhibiting both tensile and compressive fracture characteristics.

SEM photomicrographs

Fracture type	Translaminar mode I compression
Ply layup	[0, 0] 16S
Test type	Four-point bend
• Test conditions	Dry
• Fiber end fracture	
Material	Hercules 3501-6 177°C cure AS4 fibers



Mechanically induced crack direction

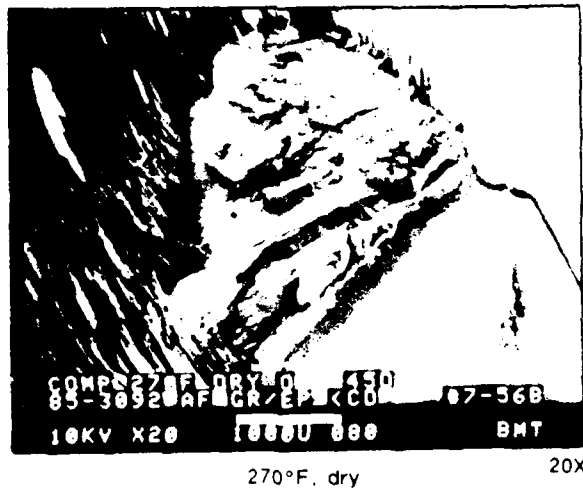
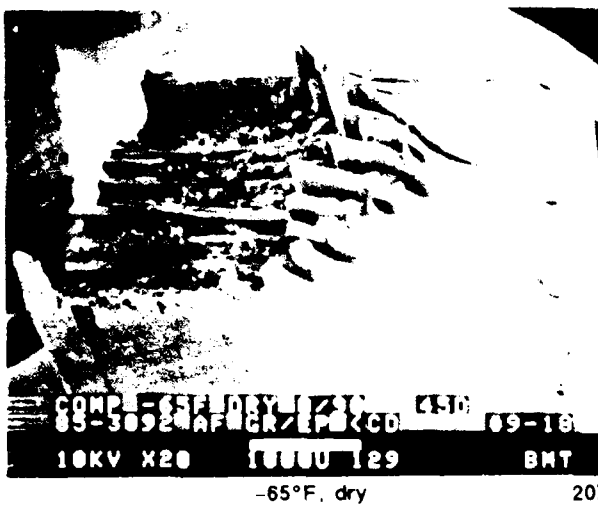
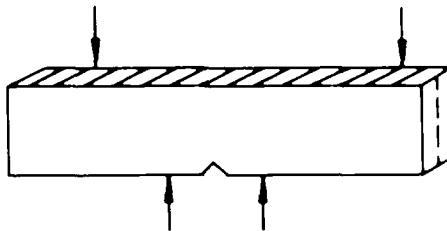


Figure 22. Low Magnification SEM Fractographs Illustrating Similar Appearances of Translaminar Compression Fracture at Different Temperatures for 0-deg Laminates

6-B79236R1-22

SEM photomicrographs

Fracture type	Translaminar mode I compression
Ply layup	[0, 90]16S
Test type	Four-point bend
• Test conditions	Dry
• Fiber end fracture	
Material	Hercules 3501-6/177°C cure AS4 fibers



Mechanically induced crack direction



Figure 23. Low Magnification SEM Fractographs Illustrating Similar Appearances of Translaminar Compression Fracture at Different Temperatures for 0/90-deg Laminates

6-B70236-23

SEM photomicrographs

Fracture type	Translaminar mode I compression
Ply layup	[0, 45 90]16S
Test type	Four-point bend
• Test conditions	Dry
Material	Hercules 3501-6 177°C cure AS4 fibers

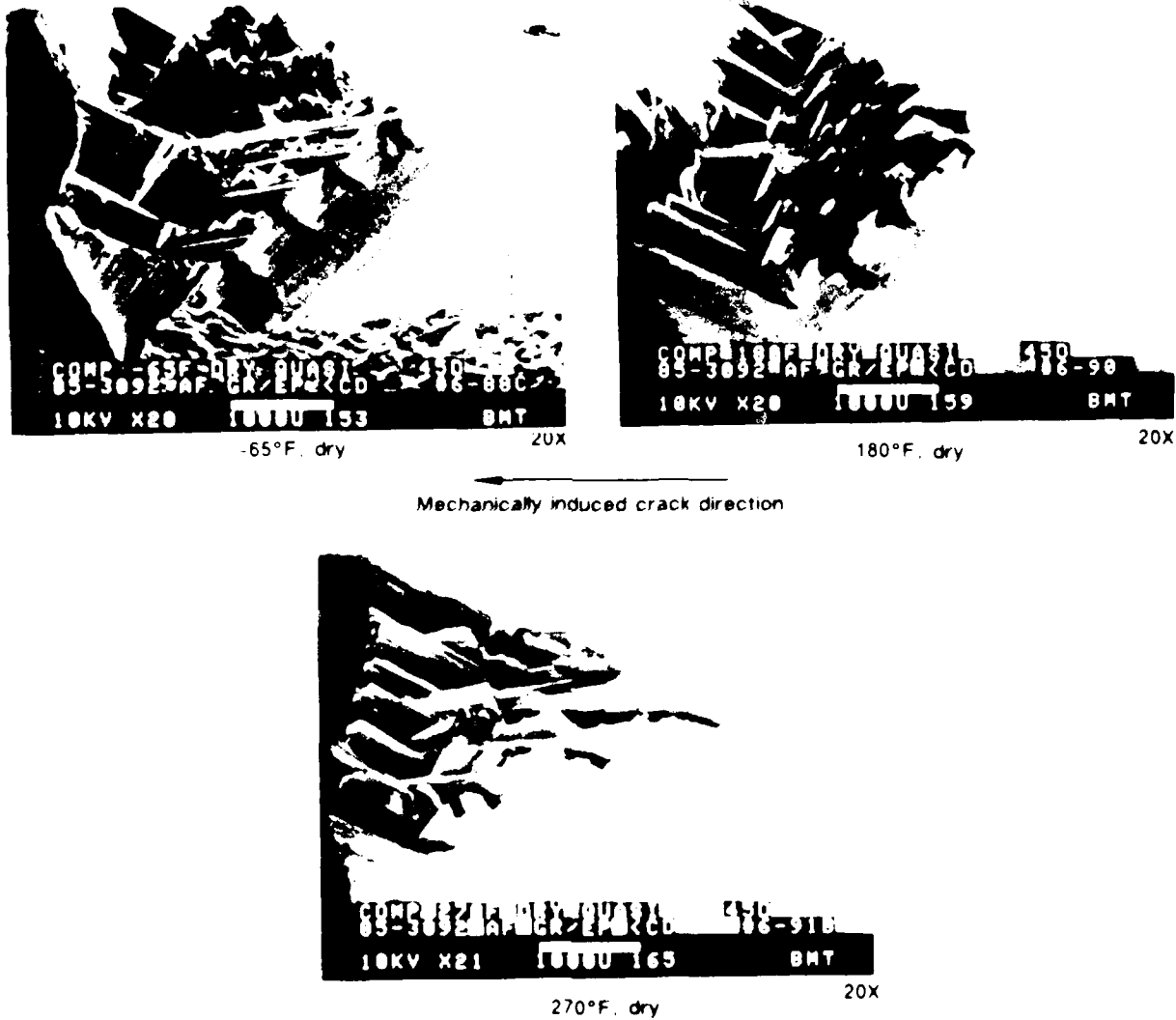
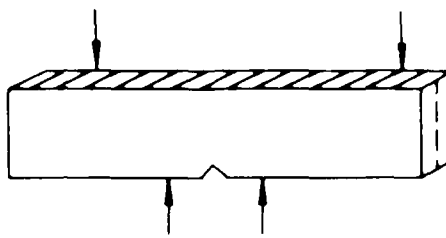
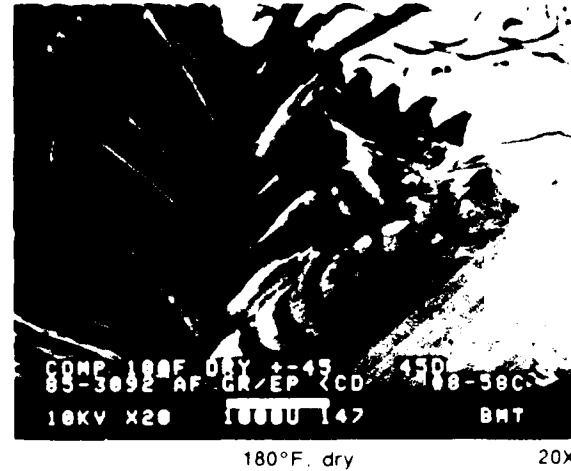
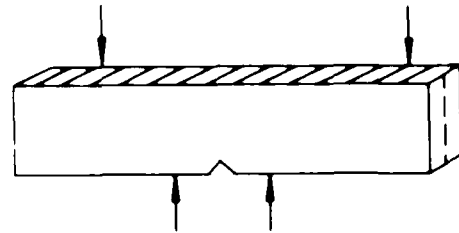


Figure 24 Low Magnification SEM Fractographs Illustrating Similar Appearances of Translaminar Compression Fracture at Different Temperatures for Quasi-Isotropic Laminates

6-B70236-24

SEM photomicrographs

Fracture type	Translaminar mode I compression
Ply layup	[+45 -45] 16S
Test type	Four-point bend
• Test conditions	Dry
• Fiber end fracture	
Material	Hercules 3501-6 177°C cure AS4 fibers



Mechanically induced crack direction

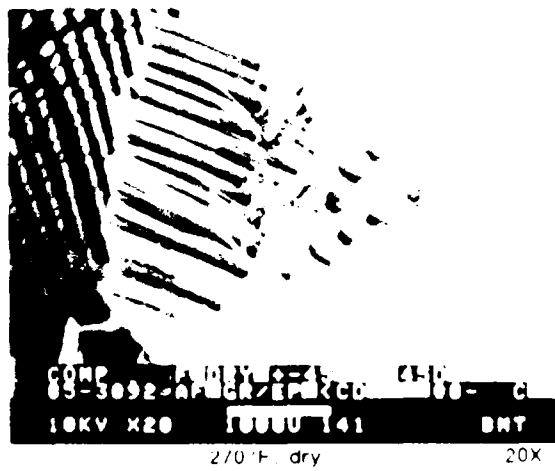


Figure 25 Low Magnification SEM Fractographs of Translaminar Compression Fracture at Different Temperature for +45/-45-deg Laminates

6-B70226R1-025

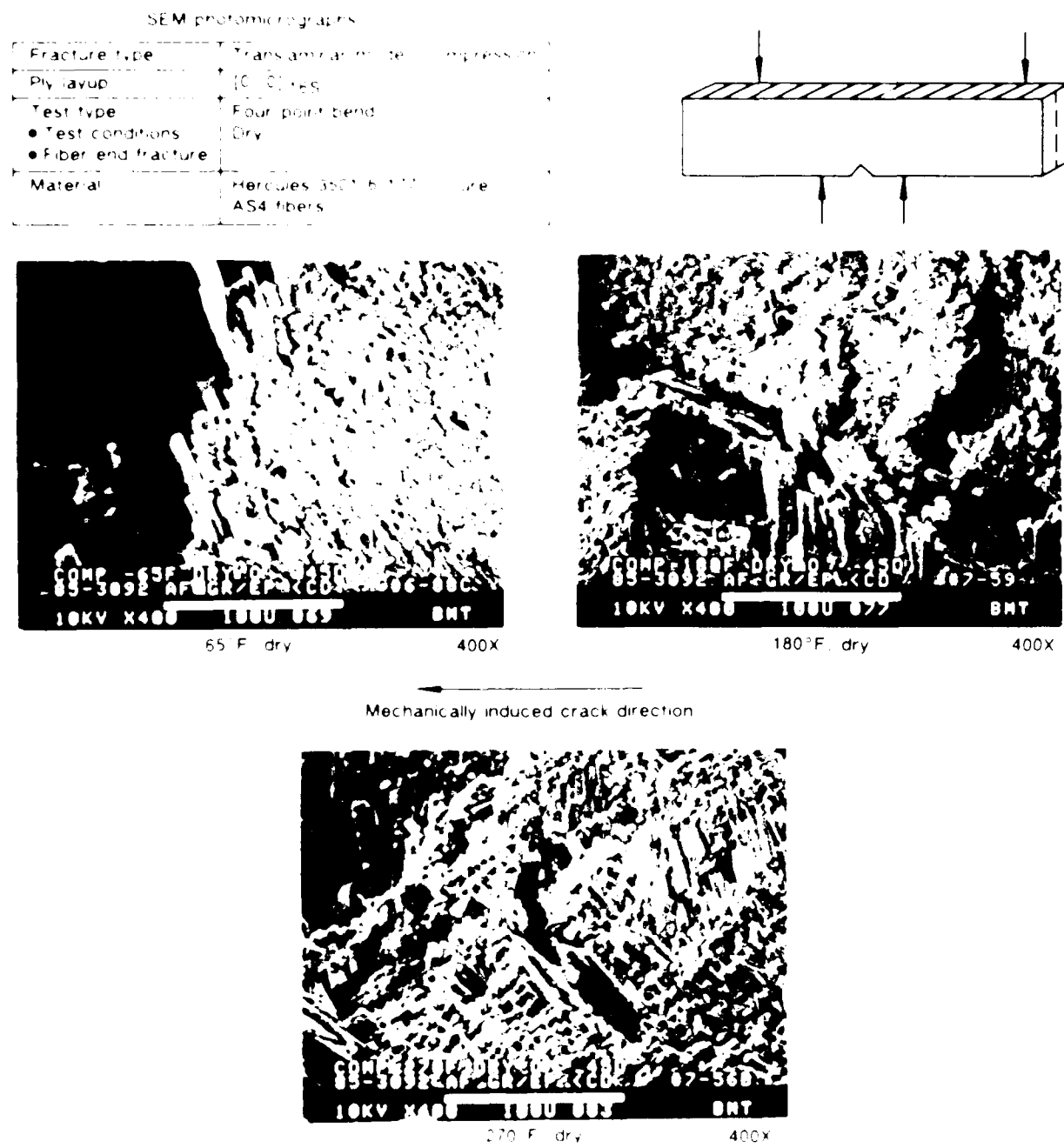
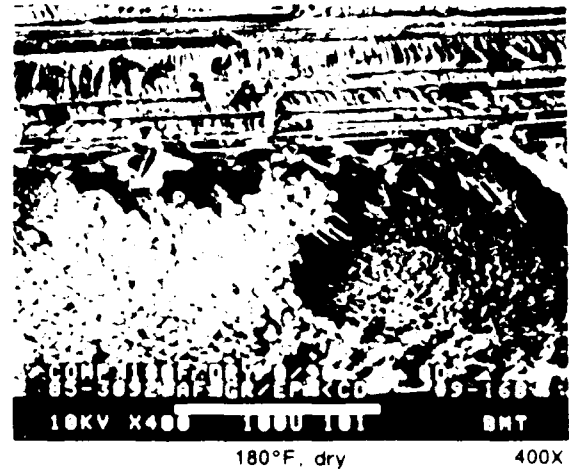
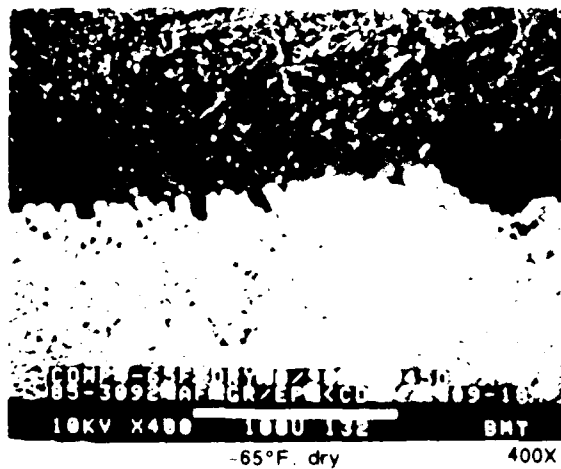
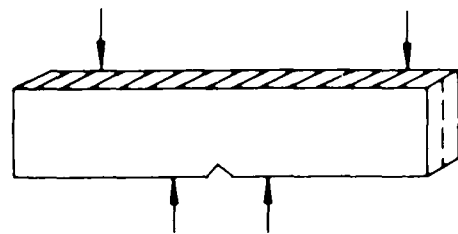


Figure 11. SEM fractographs illustrating the visual appearance of translaminar compression fracture at different temperatures for 17% carbonates.

6-B1036.C.6

SEM photomicrographs

Fracture type	Translaminar mode I compression
Ply layup	[0, 90]16S
Test type	Four-point bend
• Test conditions	Dry
• Fiber end fracture	
Material	Hercules 3501-6 177°C cure AS4 fibers



Mechanically induced crack direction

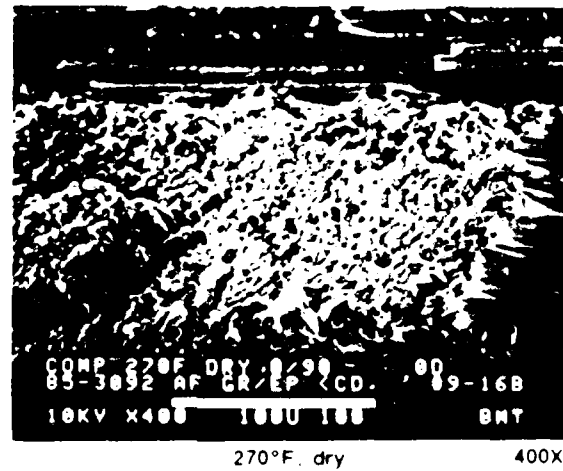
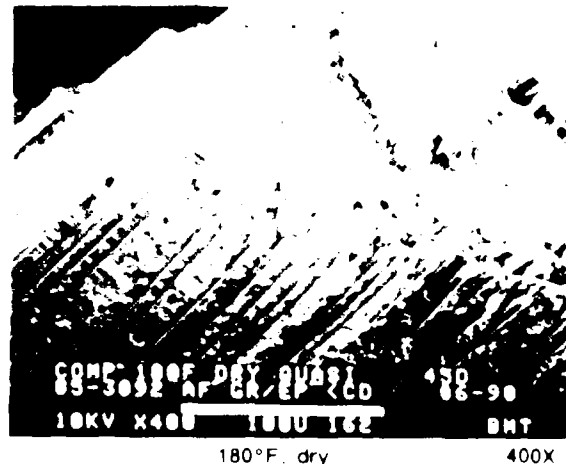
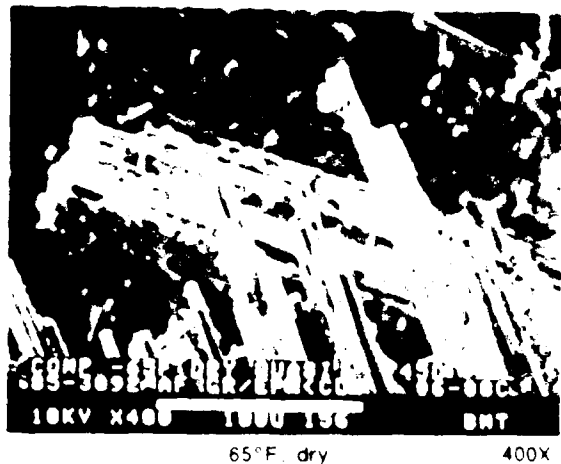
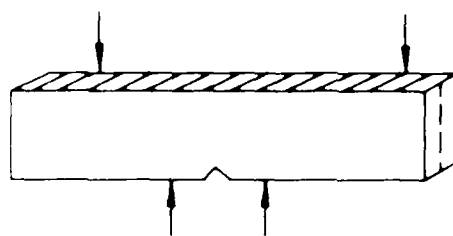


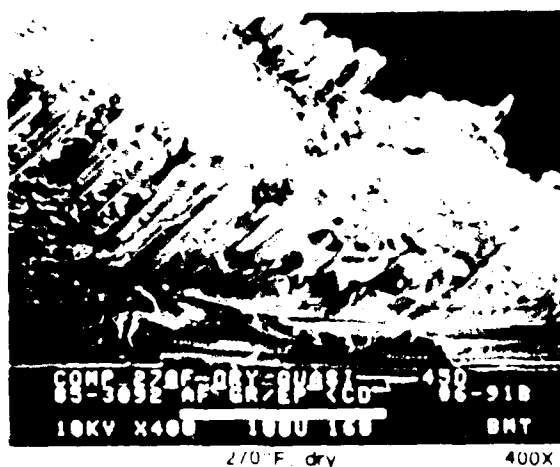
Figure 27 SEM Fractographs Illustrating Similar Appearances of Translaminar Compression Fracture at Different Temperatures for 0/90-deg Laminates

6 B70236 027

SEM photomicrographs	
Fracture type	Translaminar mode - compression
Ply layup	[0 45 90] 6S
Test type	Four point bend
• Test conditions	Dry
Fiber end fracture	
Material	Hercules 3501 8 177 C/cure AS4 fibers



Mechanically induced crack direction



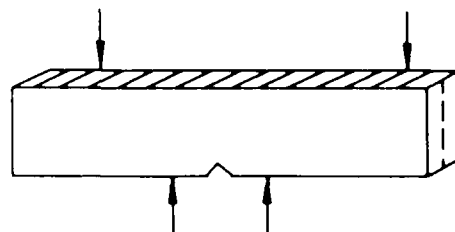
For quasi-isotropic laminates note large percentage of tensile fiber fractures occurred at 65°F

Figure 28 SEM Fractographs Illustrating Translaminar Compression Fracture Appearances at Different Temperatures

6 B70236-028

SEM photomicrographs

Fracture type	Translaminar mode I compression
Ply layup	[+45, -45] 16S
Test type • Test conditions • Fiber end fracture	Four-point bend Dry
Material	Hercules 3501-6 177°C cure AS4 fibers



Mechanically induced crack direction

6-B70236R1-029

Figure 29. SEM Fractographs Illustrating Similar Appearances of Translaminar Compression Fracture at Different Temperatures for +45/-45-deg Laminates

The above results indicate that, while the overall mode of failure may be identifiable, no specific features exist indicative of either the environment or direction of crack propagation. While this finding suggests translaminar compression fractures to be relatively intractable, it is worthwhile to remember that significant amounts of delamination commonly accompany translaminar compression failures. As demonstrated in the interim report, these failure modes can often be analyzed with fairly good success.

5.4.2 Environmental, Wet

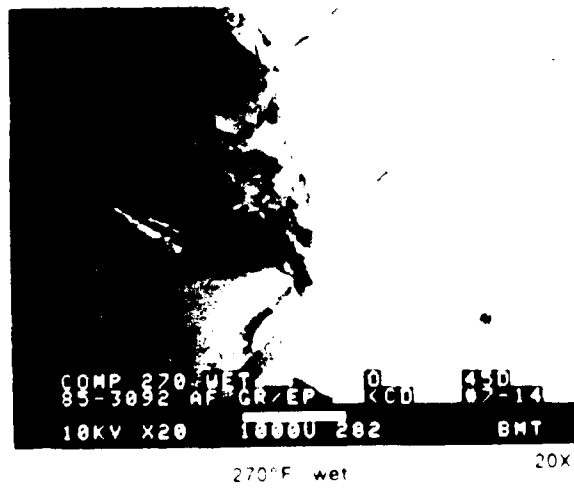
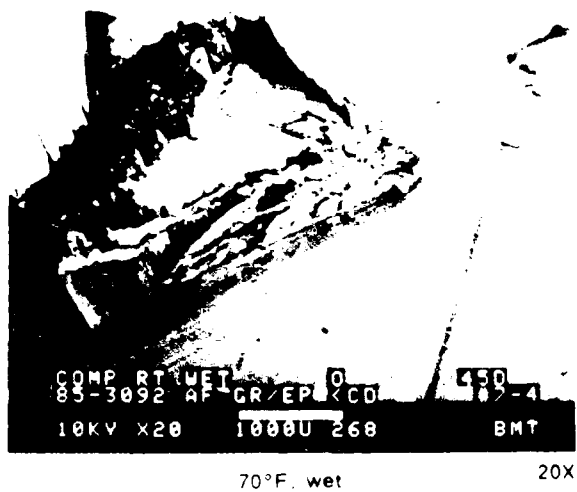
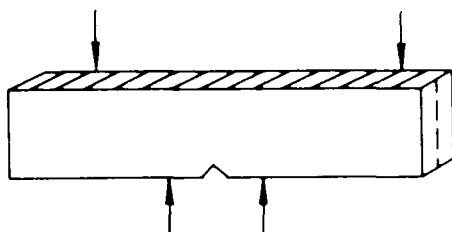
These specimens were tested under various temperatures, -65°F (-54°C) to 270°F (132°C), and were preconditioned to an absorbed moisture content of 1% by weight. Failed environmental wet compression specimens exhibited morphologies similar to that noted above for environmental dry compression failures. In this regard, the general topography produced exhibited extensive compression damage. No topographical relationship was observed with either the environment or degree of absorbed moisture present at the time of failure.

At an immediately obvious level of detail, failure occurred in the notch area by compression followed by a distinct transition into tensile failure (see figures 30 through 33). At this level of inspection, increasing test temperature can be seen to produce enlargement of the compressive failure zone as well as more distinct fiber pull out in areas of tensile separation. This alteration in compression failure zone size probably reflects the decreased compression stability of the notched region due to lowering of the matrix modulus with increasing temperature. Based on this behavior, the size of compression failure would also be expected to increase with moisture absorption. However, in comparing the appearance of wet versus dry specimens (see previous paragraphs), no differences in the size of compression failure can be distinguished. Given the pronounced effects of temperature visible in figures 30 through 33, this finding tends to suggest that matrix modulus reductions due to moisture are less than those produced by increasing temperature.

At higher magnification, failure by compression can be seen to produce a distinctly flattened topography. As depicted in figures 34 through 37, fiber failure appears to occur by axial microbuckling as evidenced by the extensive amounts of fiber kinking. Surface damage generated by the compression event, however, generally precludes the

SEM photomicrographs

Fracture type	Translaminar mode I compression
Ply layup	[0.0]16S
Test type	Four-point bend
• Test conditions	Wet
Material	Hercules 3501-6 177°C cure AS4 fibers



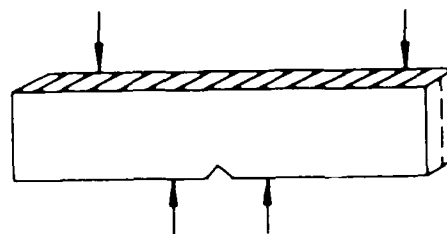
Mechanically induced
crack direction

Figure 37 Low Magnification Fractographs of C-deg Laminate Compression Failures Produced at 70°F, 180°F, and 270°F Wet

6-B70236-30

SEM photomicrographs

Fracture type	Translaminar mode I compression
Ply layup	[0.45 90] 16S
Test type	Four-point bend
• Test conditions	Wet
Material	Hercules 3501-6 177 °C cure AS4 fibers



COMP 100 WET QUASI 450
85-3092 AF GR/EP XCD 06-10
10KV X20 1000U 266 BMT

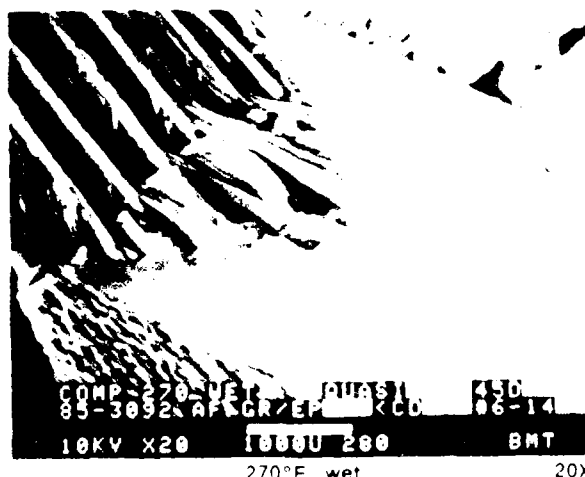
70°F, wet 20X



COMP 100 WET QUASI 450
85-3092 AF GR/EP XCD 06-10
10KV X20 1000U 272 BMT

180°F, wet 20X

Mechanically induced
crack direction



COMP 100 WET QUASI 450
85-3092 AF GR/EP XCD 06-14
10KV X20 1000U 280 BMT

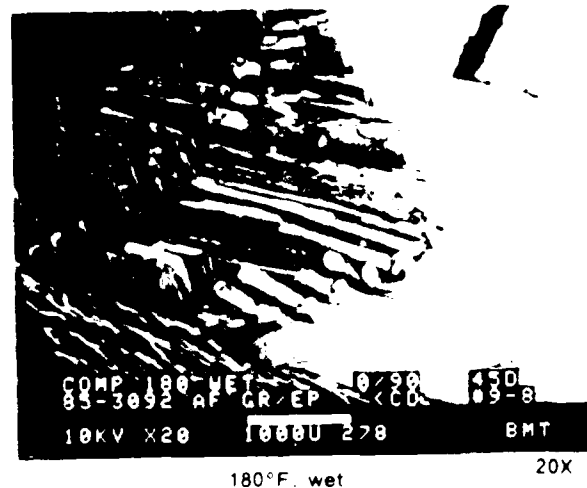
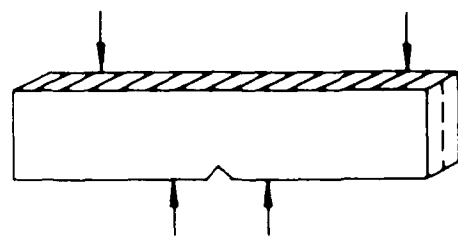
270°F, wet 20X

Figure 31 Low Magnification Fractographs of Quasi-Isotropic Laminate Compression Failures Produced at 70°F, 180°F, and 270°F, Wet

6-B70236-31

SEM photomicrographs

Fracture type	Translaminar mode I compression
Ply layup	[0/90] _{1S}
Test type	Four-point bend
• Test conditions	
• Fiber end fracture	Wet
Material	Hercules 3501-6 177°C cure AS4 fibers



Mechanically induced
crack direction

Figure 32 Low Magnification Fractographs of 0/90-deg Laminate Compression Failures Produced at 70°F, 180°F, and 270°F Wet

SEM photomicrographs

Fracture type	Translaminar mode I compression
Ply layup	[+45/-45] TES
Test type	Four-point bend
• Test conditions	Wet
• Fiber end fracture	
Material	Hercules 3501-E 177°C cure AS4 fibers

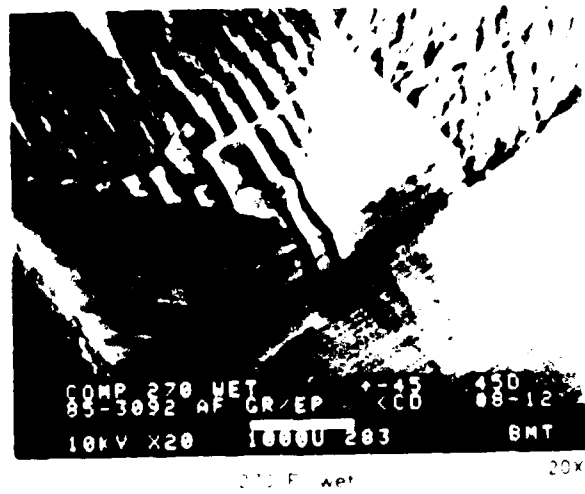
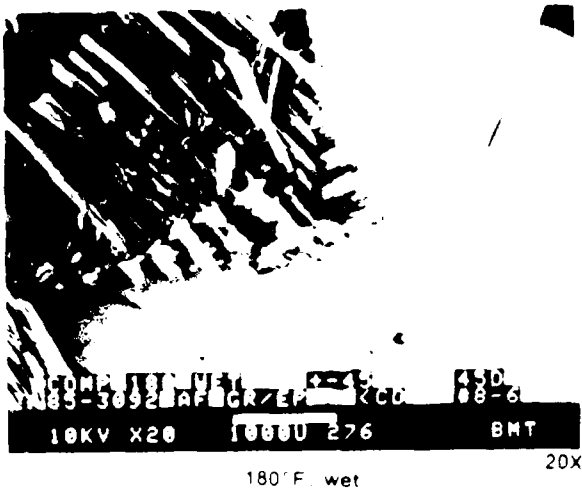
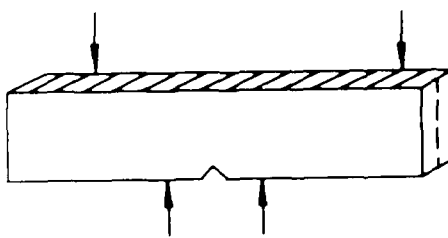
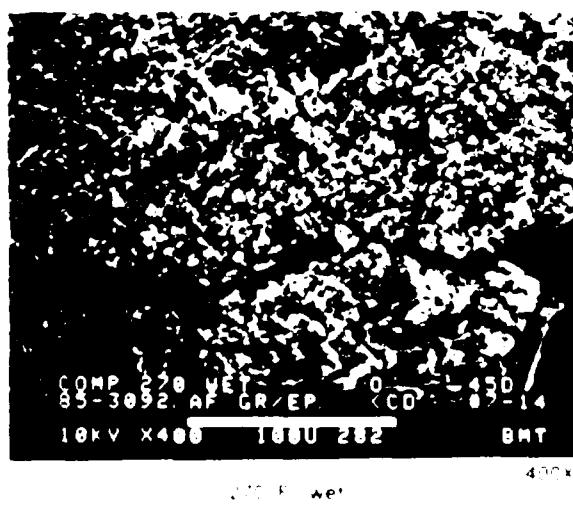
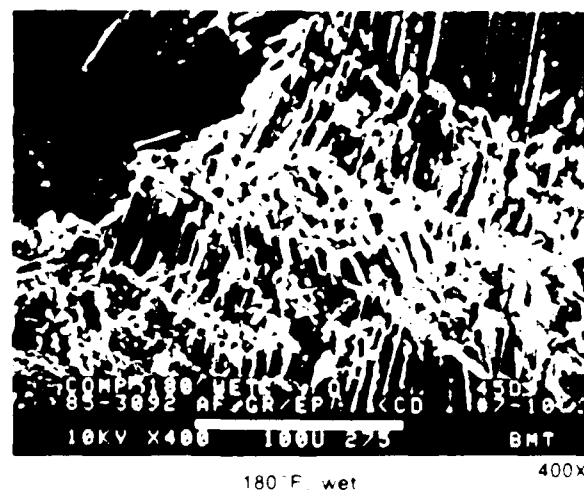
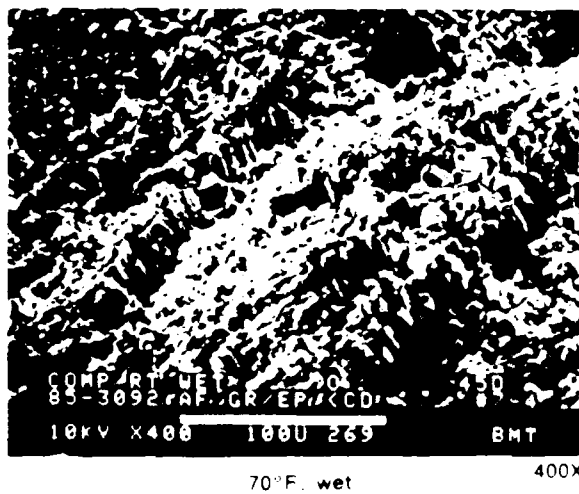
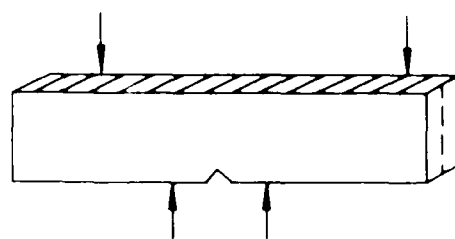


Figure 33 Low Magnification Fractographs of +45/-45-deg Laminate Compression Failures Produced at 70°F, 180°F, and 270°F, Wet

6 B70236 33

SEM photomicrographs

Fracture type	Translaminar mode I compression
Ply layup	[0 0]16S
Test type	Four-point bend
• Test conditions	Wet
Material	Hercules 3501-6 177°C cure AS4 fibers

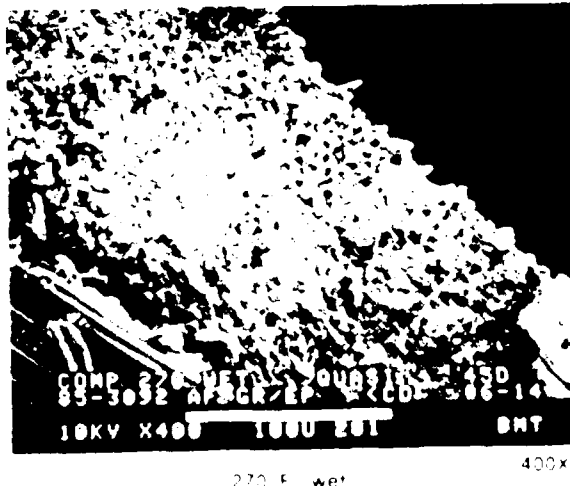
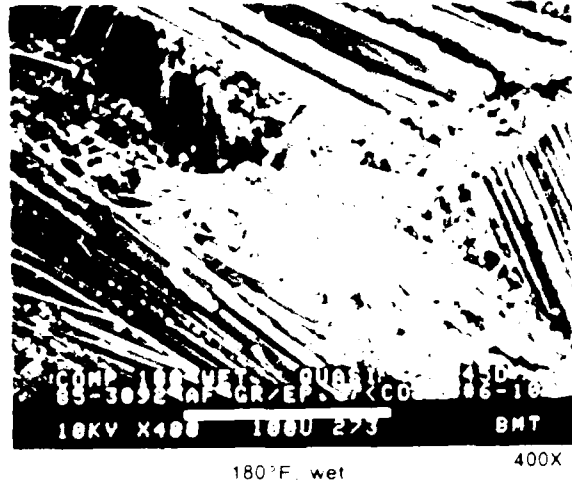
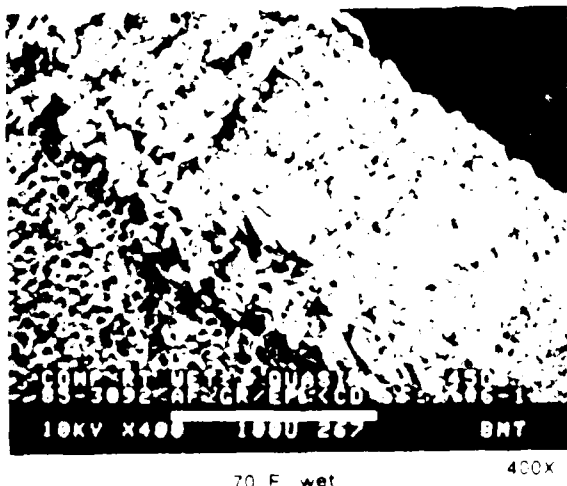
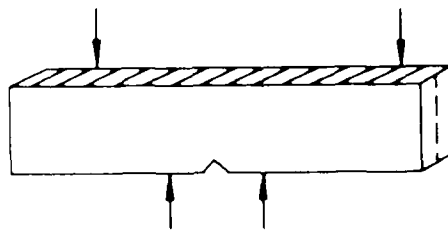


270°F wet

Figure 34 SEM Fractographs of 180 deg laminate - impression by four-point bend at 70°F, 180°F, and 270°F wet

SEM photomicrographs

Fracture type	Translaminar mode I compression
Ply layup	[0, 45, 90] 16S
Test type	Four-point bend • Test conditions • Fiber end fracture
Material	Hercules 3501-6 177°C cure AS4 fibers



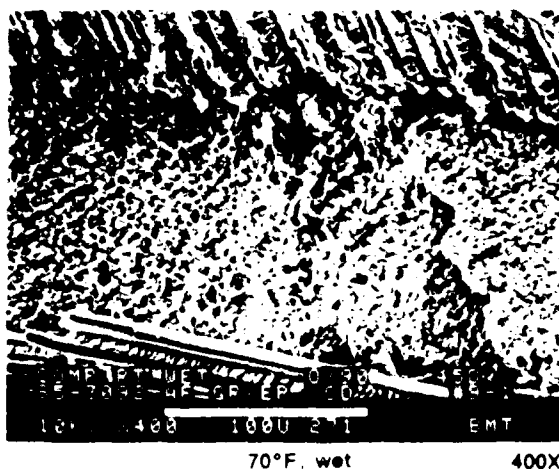
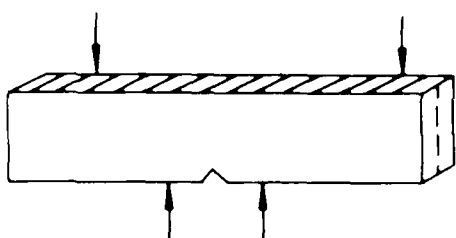
Mechanically induced
crack direction

Figure 35 SEM Fractographs of Quasi-isotropic Laminate Compression Failures Produced at 70°F, 180°F, and 270°F Wet

60
55
50
45
40
35
30

SEM photomicrographs

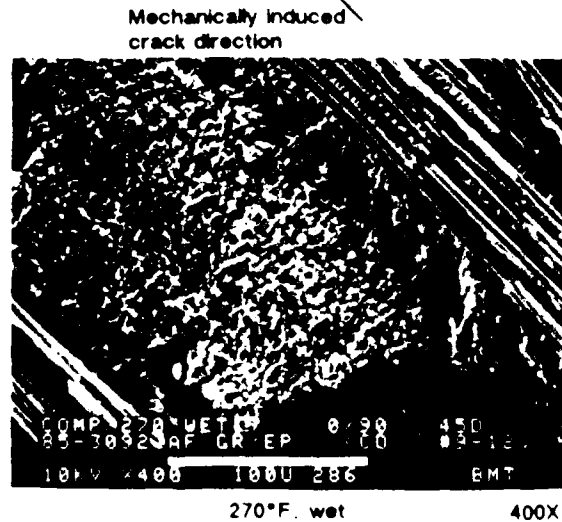
Fracture type	Translaminar mode I compression
Ply layup	[0/90]16S
Test type	Four-point bend
• Test condition	Wet
• Fracture	Fiber end
Material	Hercules 3501-6/177°C cure AS4 fibers



70°F, wet 400X



180°F, wet 400X



270°F, wet 400X

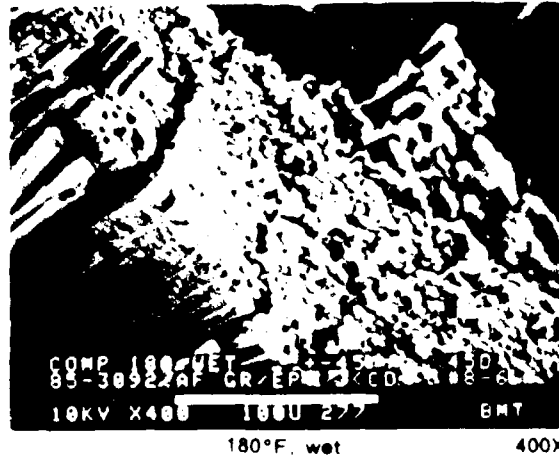
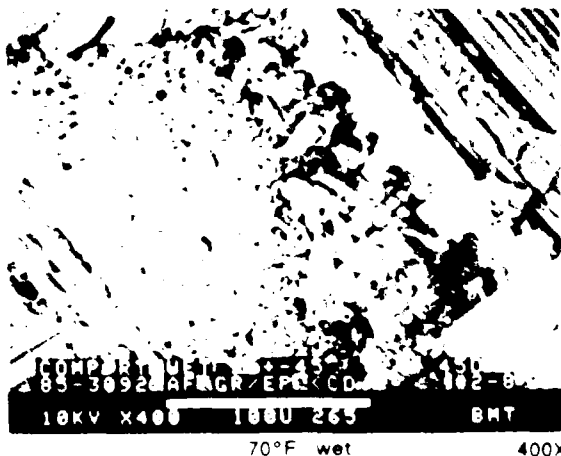
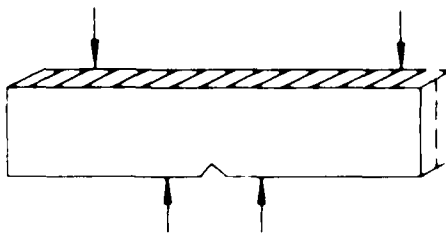
Mechanically induced
crack direction

Figure 36. SEM Fractographs of 0/90-deg Laminate Compression Failures
Produced at 70°F, 180°F, and 270°F, Wet

6-870236 036

SEM photomicrographs

Fracture type	Translaminar mode I compression
Ply layup	[+45/-45] 16S
Test type	Four-point bend
• Test condition	Wet
• Fracture	Fiber end
Material	Hercules 3501 6 177°C cure AS4 fibers



Mechanically induced
crack direction

Figure 37 SEM Fractographs of +45/-45 deg Laminate Compression Failures Produced at 70°F, 180°F, and 270°F Wet

6 B70236 031

recognition of details at any finer level. These observations are consistent with those previously reported for specimens failed without absorbed moisture. In comparing failure modes at this level, no difference in failure mode is recognizable due to absorbed moisture.

In summary, for compression failures the following conclusions can be drawn.

- Compression as a mode of failure can be easily identified by a flattened topography characterized by extensive surface damage and fiber microbuckling.
- Increasing test temperature, while increasing the size of compression failure (in specimens with bending) produces no discernable changes in fracture topography. Similarly, absorbed moisture produces no recognizable alteration in failure appearance.
- The orientation and appearance of translaminar fracture features do not correspond with the direction of induced fracture.

These findings indicate that for compression failures, the direction of crack propagation and environment at failure cannot be determined based on translaminar fractographic examinations. In part, this result is not surprising given the process under which compression failure occurs and the subsequent postfailure damage typically generated. However, it should be noted that delaminations induced by compression failure can provide areas of fractographic evidence suitable to identify the direction of failure and subsequent origin area (see paragraph 5.13, Compression After Impact).

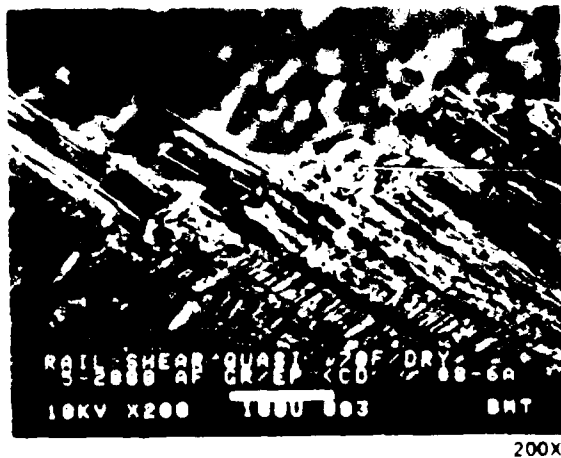
5.5 Translaminar Mode II Rail Shear

Rail shear (inplane transverse shear) specimens exhibited a similar behavior in that the predominant mode of failure consisted of compression damage and fiber microbuckling. However, these failures exhibited a much rougher overall topography with clusters, and often isolated fibers, protruding from the plane of fracture. In addition, extensive fiber matrix disbonding was also observed. As with compression failures, the occurrence of these features was not observed to be dependent on either failure temperature or absorbed moisture.

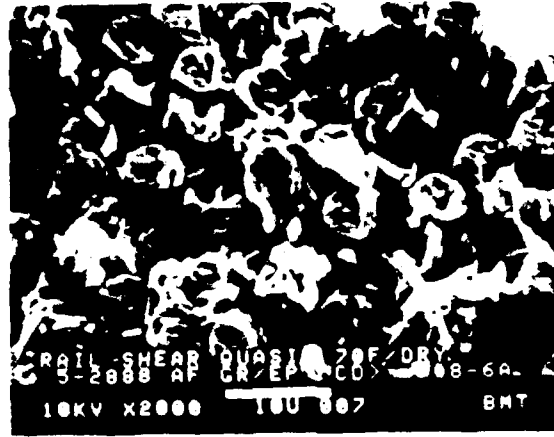
Prior to a discussion on rail shear fracture characteristics, it is appropriate to review the basic behavior exhibited by specimens during test. As discussed in previous reports, rail shear developmental testing resulted in both a specimen redesign and a narrowing in

SEM photomicrographs

Fracture type	Translaminar mode II shear
Ply layup	[0 45 90] 16S
Test type	Side-notched rail shear
• Test conditions	70°F dry
• Fiber end fracture	
Material	Hercules 3501-6:177°C cure AS4 fibers



Mechanically induced
crack direction



Mechanically induced
crack direction

200X

Tilted 180 deg from
the photo on the left

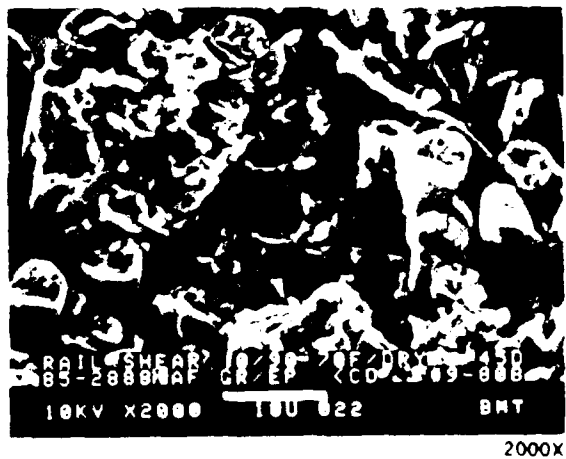
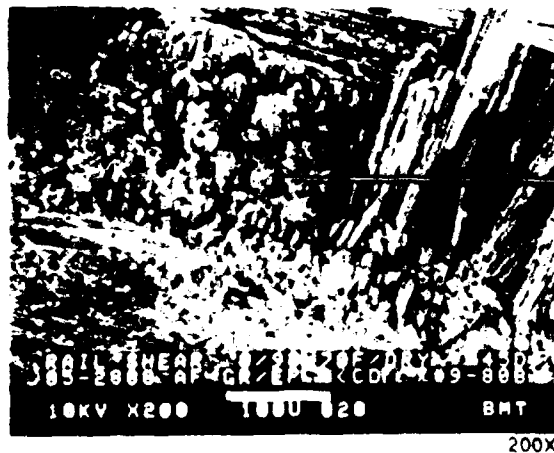
General topography exhibits features characteristic of both compression and flexural fiber failure.

Figure 38 SEM Fractographs Illustrating Morphology of 70°F Dry 0/90 deg
Laminate Rail Shear Failure

6-B70236-038

SEM photomicrographs

Fracture type	Translaminar mode II shear
Ply layup	[0 .90] 16S
Test type	Side-notched rail shear
• Test conditions	70°F, dry
• Fracture	Fiber end
Material	Hercules 3501-6/177°C cure AS4 fibers



Mechanically induced
crack direction

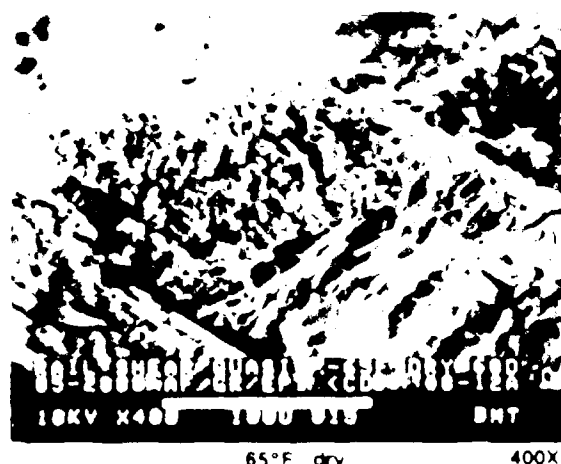
General topography exhibits features characteristic of both compression and flexural fiber failure

Figure 39 SEM Fractographs illustrating Morphology of 70°F Dry Quasi-Isotropic Laminate Rail Shear Failure

6-B70236 039

SEM photomicrographs

Fracture type	Translaminar mode II shear
Ply layup	[0.45.90] 16S
Test type	Side-notched rail shear
• Test condition	Dry
• Fracture	Fiber end
Material	Hercules 3501-6 177°C cure AS4 fibers



Mechanically induced
crack direction

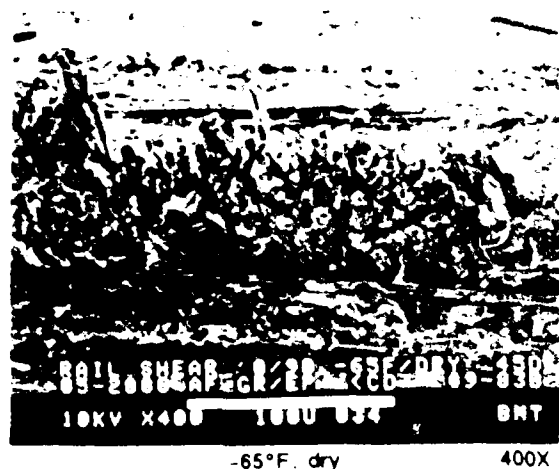


Fig. 4. Low Magnification Fractographs Illustrating Morphology of Quasi-Static Shear Failures Produced at 65°F, 180°F, and 270°F Dry.

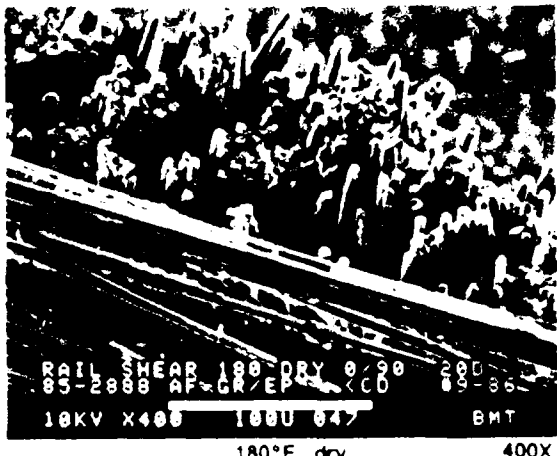
EBT 23E 140

SEM photomicrographs

Fracture type	Translaminar mode II shear
Ply layup	[0.90] 16S
Test type	Side-notched rail shear
• Test conditions	Dry
• Fracture	Fiber end
Material	Hercules 3501-6/177°C cure AS4 fibers

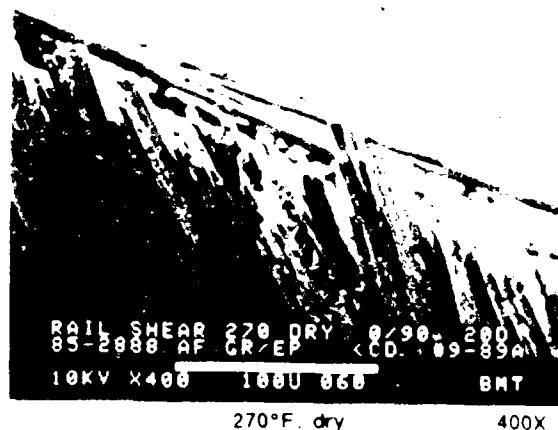


-65°F, dry 400X



180°F, dry 400X

Mechanically induced
crack direction



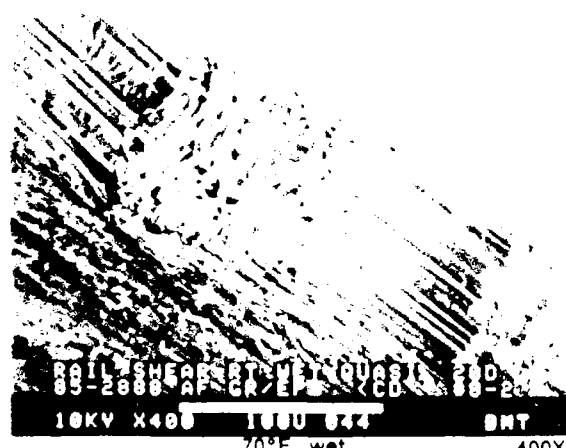
270°F, dry 400X

Figure 41 Low Magnification Fractographs Illustrating Morphology of 0/90-deg Rail Shear Failures Produced at -65°F, 180°F, and 270°F, Dry

6-B70236-041

SEM photomicrographs

Fracture type	Translaminar mode II shear
Ply layup	[0 45 90]16S
Test type	Side-notched rail shear
• Test conditions	Wet
• Fracture	Fiber end
Material	Hercules 3501-6 177°C cure AS4 fibers



Mechanically induced crack direction

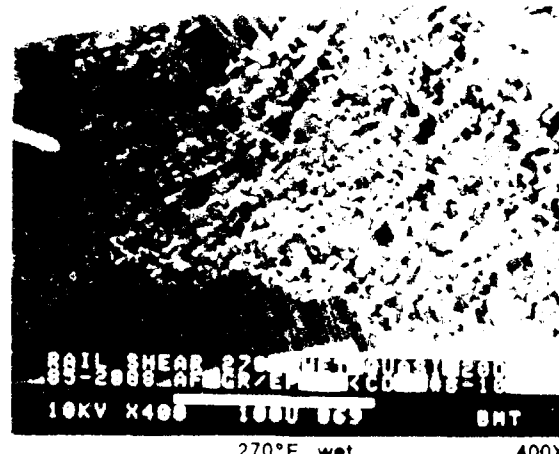
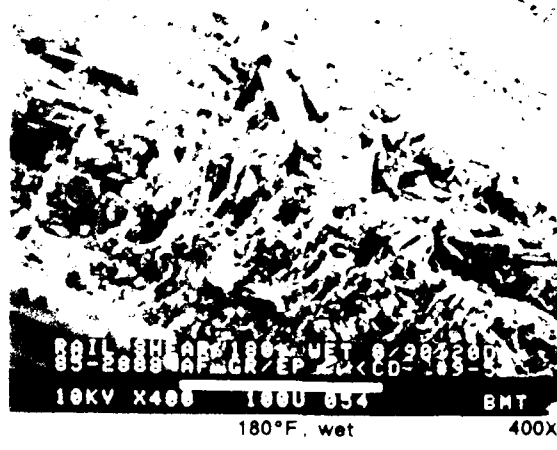
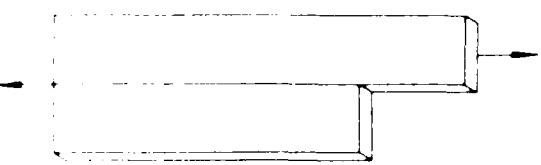


Figure 42 Low Magnification Fractographs Illustrating Morphology of Quasi-Isotropic Rail Shear Failures Produced at 70°F, 180°F, and 270°F, Wet

6-B70236-042

SEM photomicrographs

Fracture type	Translaminar mode II shear
Ply layup	[0, 90]16S
Test type	Side-notched rail shear
• Test conditions	Wet
• Fracture	Fiber end
Material	Hercules 3501-6 177°C cure AS4 fibers



Mechanically induced crack direction

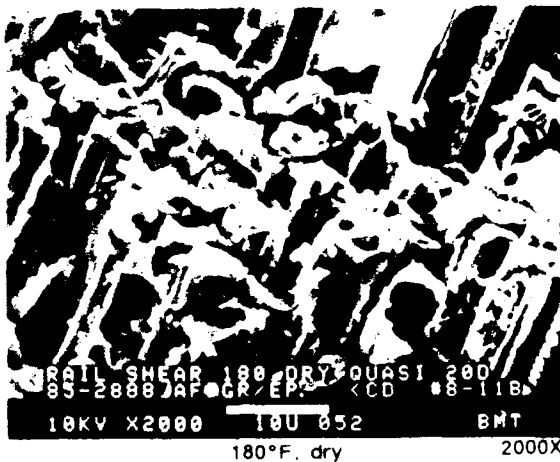
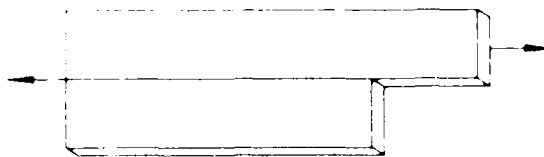


Figure 43 Low Magnification Fractographs Illustrating Morphology of 0-90-deg Rail Shear Failures Produced at 70°F, 180°F, and 270°F Wet

6-B70236-043

SEM photomicrographs

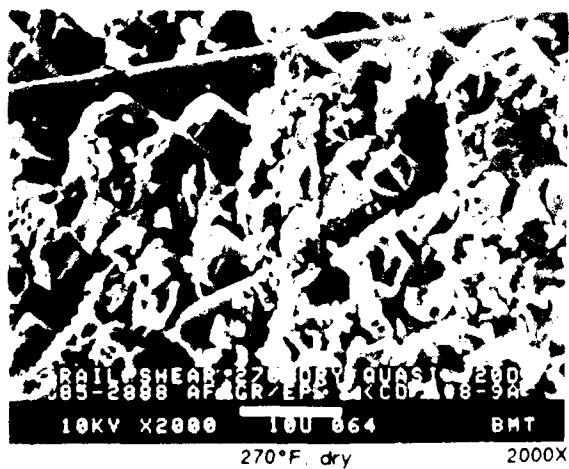
Fracture type	Translaminar mode II shear
Ply layup	[0, 45, 90] 16S
Test type	Side-notched rail shear
• Test conditions	Dry
• Fracture	Fiber end
Material	Hercules 3501-6 177°C cure AS4 fibers



-65°F, dry 2000X

180°F, dry 2000X

Mechanically induced crack direction



270°F, dry 2000X

Figure 44: Detailed Fracture Characteristics of Quasi-Isotropic Rail Shear Laminates Failed at -65°F, 180°F, and 270°F Dry

6-870236-044

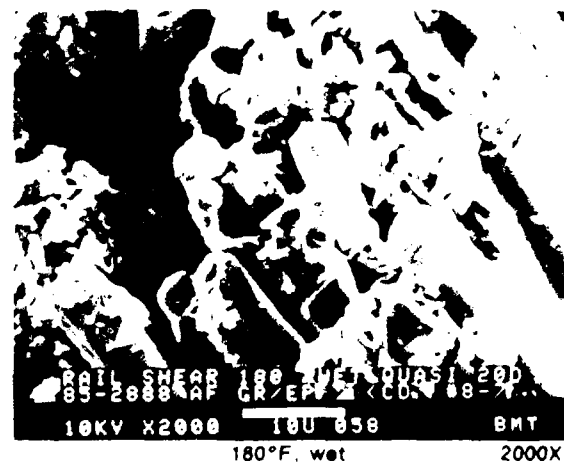
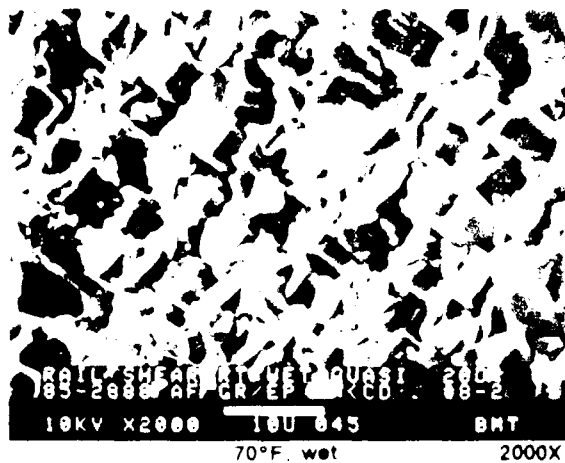
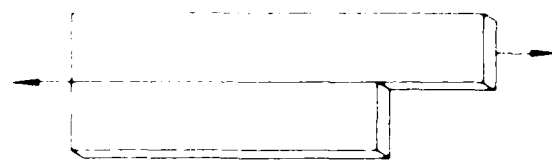


Figure 45. Detailed Fracture Characteristics of 0/90-deg Rail Shear Laminates Failed at -65°F, 180°F, and 270°F, Dry

6-B70236R1-045

SEM photomicrographs

Fracture type	Translaminar mode II shear
Ply layup	[0, 45, 90] 16S
Test type	Side-notched rail shear
• Test conditions	Wet
• Fracture	Fiber end
Material	Hercules 3501-6 177°C cure AS4 fibers



Mechanically induced crack direction

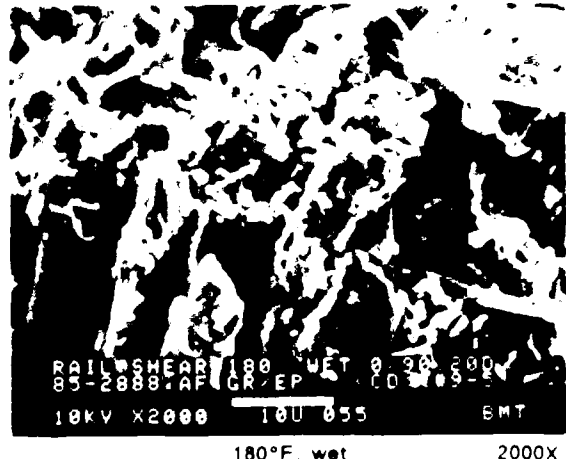
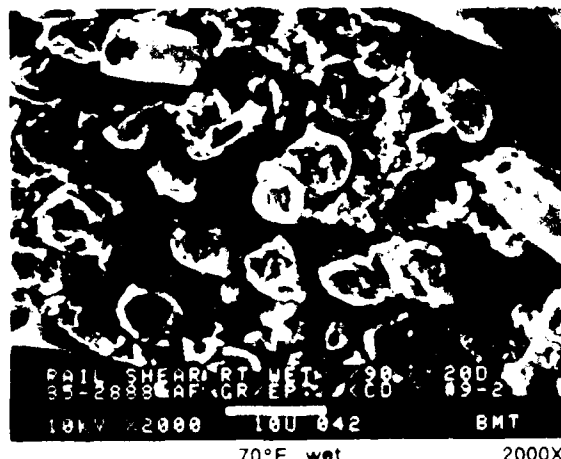


Figure 46 Detailed Fracture Characteristics of Quasi-Isotropic Rail Shear Laminates Failed at 70°F, 180°F, and 270°F, Wet

6-B70236-046

SEM photomicrographs

Fracture type	Translaminar mode II shear
Ply layup	[0, 90] 16S
Test type	Side-notched rail shear
• Test conditions	Wet
• Fracture	Fiber end
Material	Hercules 3501-6 177°C cure AS4 fibers



Mechanically induced crack direction



Figure 47. Detailed Fracture Surface Characteristics of 0/90-deg Rail Shear Laminates Failed at 70°F, 180°F, and 270°F, Wet.

6-B70236-047

the number of laminate orientations planned for test. In its final configuration, the specimen and layups tested were observed to produce progressive notch induced fracture. While this behavior produced failure as intended, it also was noted to produce significant crack compression due to motion between the two specimen halves. This behavior is significant in that both shear and compression loads were in operation at the time of failure.

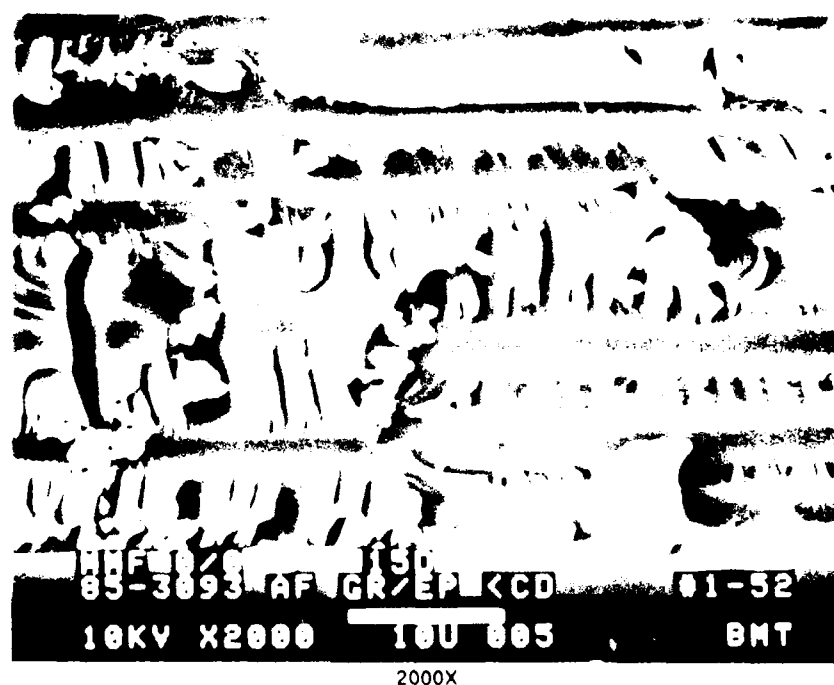
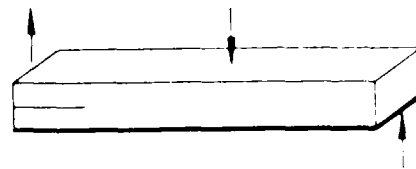
The presence of both shear and compression loads at failure were discernable in the fracture morphology exhibited by both quasi-isotropic and 0/90 laminate specimens. Figures 38 and 39 illustrate the fracture features characteristic of each laminate. In general, the overall fracture topography exhibited compression surface damage with occasional areas of pulled out fibers. In comparison, this topography tended to be more irregular than that characteristic of Mode I translaminar compression. Closer inspection revealed individual fiber fracture occurred by fiber microbuckling, as in compression. In observing a large number of areas, no correspondence of the direction of microbuckle failure and the induced crack direction was apparent. However, as shown in figure 38, conditions of extensive fiber-matrix separation in the lateral direction were prevalent in many locations with individual fibers spread apart from one another. Lateral separation of these fibers probably occurs in response to resolved and lateral tensile stresses developed as a result of shear displacement.

In perspective, the failure morphology characteristics of translaminar shear exhibits local failure modes representative of compressive and tensile separation. In general, this result is not surprising given the inability of either the fiber or matrix material to yield by a shear process. With respect to carrying out a failure analysis, the findings presented suggest that while shear failures can be identified, doing so may be difficult due to their similarity with compression fractures. More significantly, as with compression, fractographic features by which the direction of fracture can be identified do not appear to exist. However, in a similar manner to compression, secondary induced delaminations may provide a means of overcoming this problem for applied failure analyses.

As illustrated in figures 40 through 47, translaminar failures produced under shear did not exhibit any pronounced sensitivity to either environment or absorbed moisture. Figures 40 through 43 illustrate the gross fracture topography of specimens failed at 270°F wet and dry, 180°F wet and dry, 70°F wet and -65°F dry. For each

SEM photomicrograph

Fracture type	Interlaminar mode I and II
Ply layup	[0, 0] 12S
Test type	Mixed mode fracture (MMF)
• Test conditions	Dry (70°F)
• Fracture between	0 0 plies
Material	Hercules 3501-6 177°C cure AS4 fibers



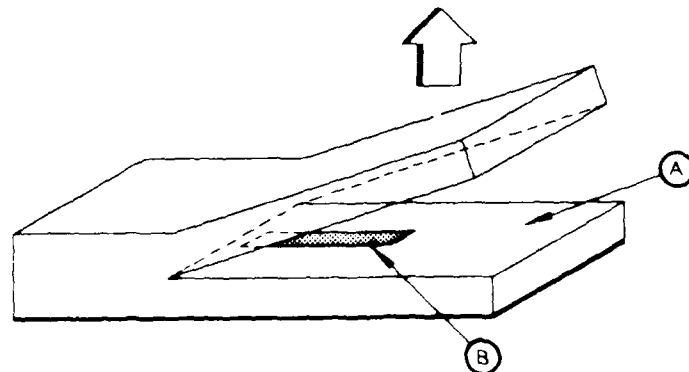
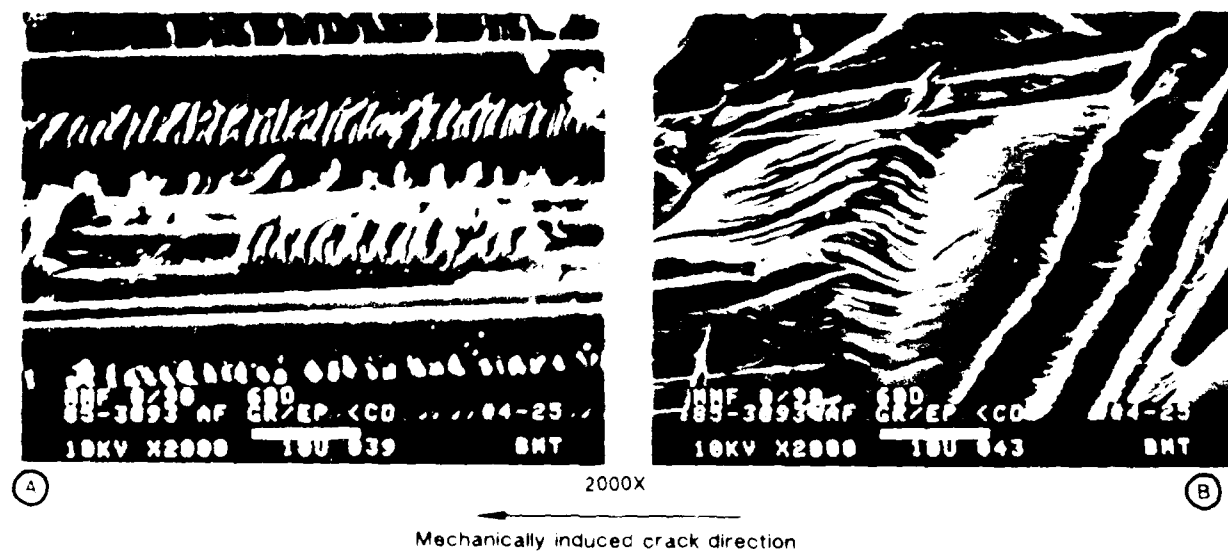
Mechanically induced crack direction

Note: Hackles and scallops formed by mechanisms A and B are illustrated.

Figure 48. Mixed Mode Fracture Morphology for 0-deg Laminate

SEM photomicrographs

Fracture type	Interlaminar mode I and II
Ply layout	(0°/90°)S
Test type	Mixed mode fracture (MMF)
• Test conditions	70°F
• Fracture between	0-90 plies
Material	Hercules 3501-6 177°C cure AS4 fibers



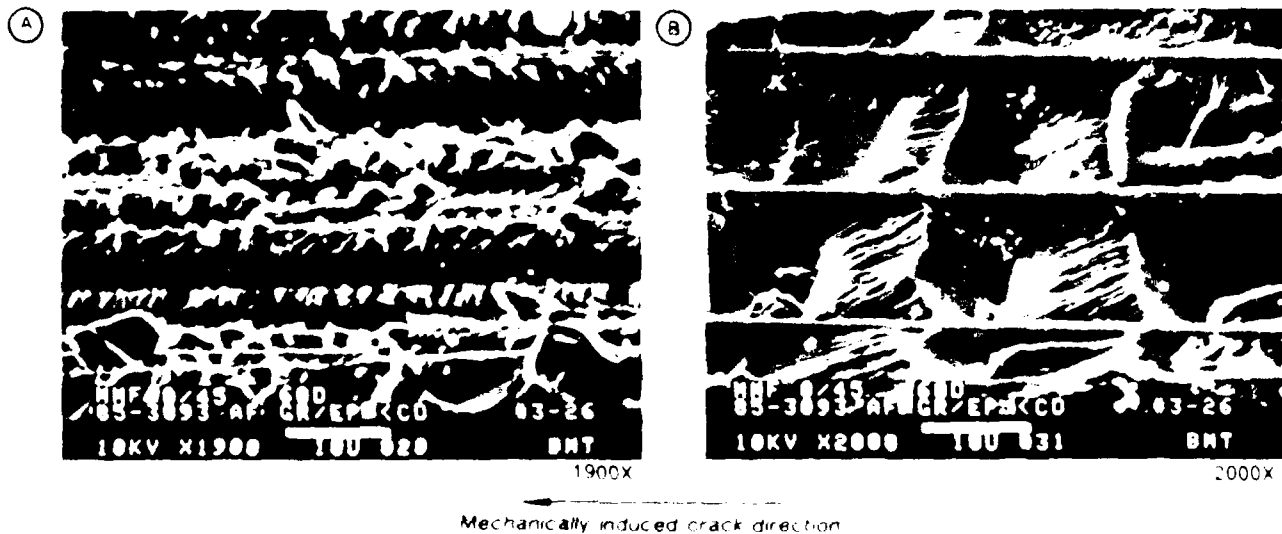
Note: Area A exhibited hackles formed by mechanism B, whereas area B exhibited river marks oriented coincident with, as well as opposite to, the induced direction of propagation.

Figure 49. SEM Fractographs Illustrating Mixed Mode Fracture of 0/90-deg Laminate

6-B70236R1-49

SEM photomicrographs

Fracture type	Interlaminar mode I and II
Ply layup	0°/45°/0°
Test type	Mixed mode fracture (IMMF)
Test conditions	2C, F, dry
Fracture between	0.45 plies
Material	Hercules 3501 & 117°C cure AS4 fibers



Mechanically induced crack direction

Note: Area A exhibited hackles formed by mechanism A whereas area B exhibited river marks coincident with as well as opposite to the induced direction of propagation

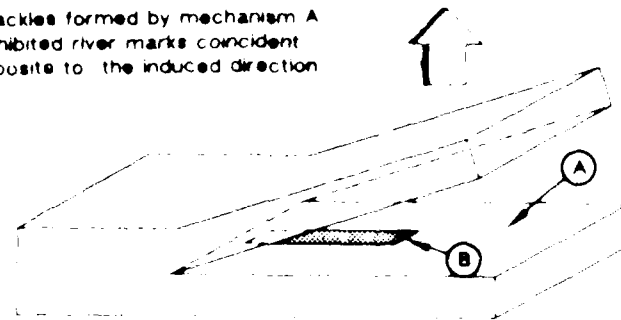
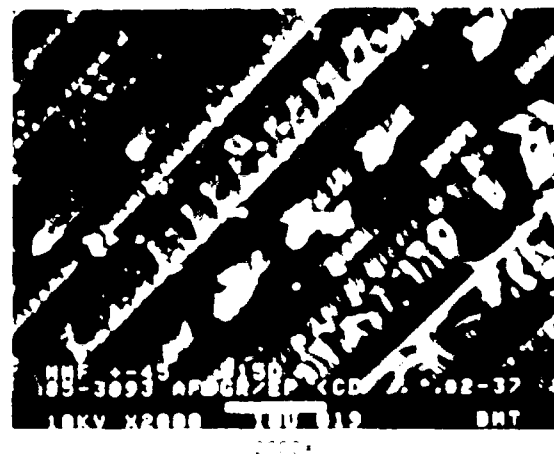


Figure 50 SEM Fractographs Illustrating Mixed Mode Fracture of 0/45-deg Laminate

6-B70236R1-50

SEM photomicrograph

Fracture type	Interlaminar mode I and II
Fly layup	+45/-45 deg/CS
Test type	Mixed mode fracture (MMF)
• Test conditions	Dry (RM), 70 F
• Fracture between	+45/-45 plies
Material	Hercules 3501 E 171°C cure A94 fibers



Mechanically induced crack direction

Figure 51 SEM Fractograph Illustrating Mixed Mode Fracture Morphology Characteristic of +45/-45-deg Laminate

6 B70236R1-51

environmental condition a mixture of compressive and tensile fracture is visible. Conditions of compression are evident at low magnifications by the existence of flattened areas with associated surface damage. At higher magnifications additional features indicative of compression, such as fiber microbuckling and detailed damage are apparent (see figures 44 through 47). As previously described for 70°F dry failures, irregular conditions of fiber pull out as well as lateral fiber-matrix disbonding are apparent at both levels of inspection. With regard to both environment and also absorbed moisture, no specific alterations in either compressive or tensile generated features are apparent. While some specimens may exhibit more of one failure characteristic than another (see figure 42), this behavior was not found to occur in a consistent manner.

5.6 INTERLAMINAR MIXED MODE FLEXURAL (MMF)

Examination of mixed mode specimens (57% Mode I, 43% Mode II) was aimed at examining the effect of complex load states on those singular failure characteristics identified for the 100% Mode I tension (DCB) and 100% Mode II shear (ENF) specimens.

Figures 48 through 51 illustrate the characteristic features of interlaminar failures produced under mixed mode loading. In general, the dominant morphology generated is that characteristic of Mode II shear. For a failure between adjacent 0-degree plies a relatively even mixture of hackles and scallops was observed (figure 48). With reference to earlier studies of pure Mode II failures, relatively little difference appears to exist. Hackle separation (for this interfacial failure condition) occurs by both mechanisms A and B, with the hackle platelets tilted parallel to the direction of induced propagation. This means that the hackle platelets can be tilted with, or opposite to, the direction of crack growth.

Mixed mode separation for several of the other crossply orientations (0/90 and 0/45) produced an interesting mixture of Mode II and Mode I fracture areas. The majority of separation occurred predominantly by Mode II fracture (see figures 49 and 50). Consistent with the 0-degree laminate specimen the overall morphology of these hackles exhibited no difference from that described previously for pure Mode II induced delaminations. With the exception of the 0/90 laminate, hackle separation for both 0/45 and +45/-45 laminates occurred predominantly by mechanism A (figures 50 and 51). Hackle separation for the 0/90 laminate occurred by mechanism B. These results

indicate that the factors controlling the dominance of one mechanism over another are not well understood. As a result, the assignment of a singular crack direction based on hackle tilt appears to be questionable. However, for failure analysis purposes the assignment of a nonsingular (parallel) crack direction may be adequate for origin identification purposes.

As indicated in figures 49 and 50, several areas of Mode I fracture were evident on each specimen. Typically, this morphology occurred in those areas where groups of fibers have been pulled from the main fracture plane. These areas of Mode I fracture exhibited river marks oriented both coincident with, as well as opposite to, the direction of crack propagation (see figure 49). This basic behavior appears to be understandable based upon how these areas of fracture are formed. As indicated earlier, these areas correspond to regions of fiber pull out. As schematically illustrated in figure 52, areas of pull out occur when local crack divergence produces fiber bridging across the crack tip. Under continued opening displacement such bridged areas can extend areas of delamination both toward, as well as away from, the direction of crack propagation. In terms of carrying out a failure analysis, this behavior can generate spurious directions of crack growth. However, examining a large number of fracture areas by optical microscopy should provide a means of averaging out such spurious areas and identifying the general direction of crack growth.

5.7 INTERLAMINAR MODE I FATIGUE

The following paragraphs describe the morphology and failure characteristics of Mode I tension interlaminar fatigue specimens. The Mode I fatigue fracture surfaces exhibited a flat topography typical of Mode I interlaminar static specimens. Microscopic features such as river marks and resin microflow were found to coincide with the direction of induced crack growth. Optical and SEM microscopy were used to identify "striations" indicative of cyclic loading.

Following testing, visual examination of the fracture surface revealed a faint set of "beach marks" which indicated the beginning and end of the slow growth fatigue region. Macroscopically, the fatigue region was identical to the static growth region, namely, flat, smooth, and shiny. Optical microscopy revealed river marks and resin microflow typical of static fractures. These features were found to be coincident with the induced

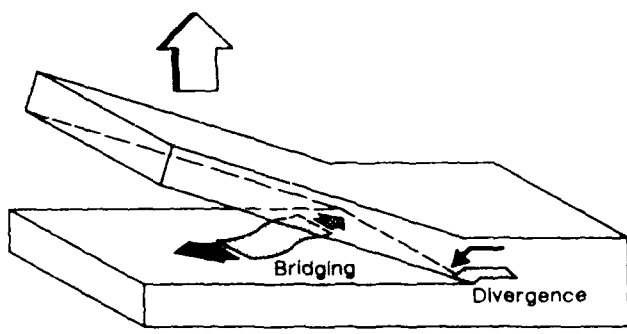


Figure 52. Schematic Showing Formation of Reverse Crack Directions Because of Out-of-Plane Crack Divergence and Subsequent Crack Tip Bridging

6-B70236R2-52

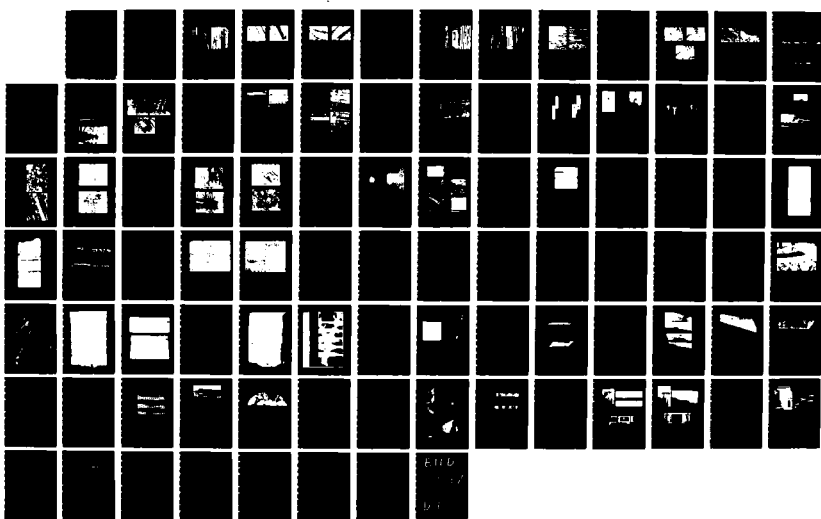
AD-A184 468 FAILURE ANALYSIS OF COMPOSITE STRUCTURE MATERIALS(U)
BOEING MILITARY AIRPLANE CO SEATTLE WA B SMITH ET AL
27 MAY 87 AFVAL-TR-87-4801 F33615-84-C-5010

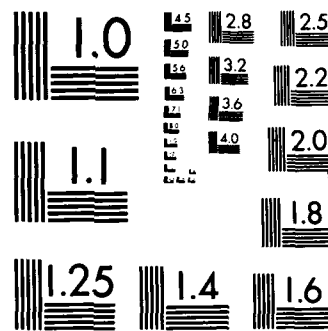
2/2

UNCLSSIFIED

F/G 11/4

NL





MICROCOPY RESOLUTION TEST CHART
NATIONAL BUREAU OF STANDARDS-1963-A

crack growth direction, indicating that crack mapping is a viable microscopic technique for determining crack growth directions and origin locations for Mode I fatigue.

Optical and SEM microscope examinations of the fatigue region identified only a few striations in the resin fracture zones. No striations were identified in the fiber-matrix interface zones. These resin striations were similar in appearance to fatigue crack growth increments in metallic materials, however they were very faint. Figures 53 and 54 present optical and SEM fractographs of these isolated regions exhibiting striations. There is localized evidence that much finer, closely spaced striations are present when seen with high magnification SEM analysis. These striations are topographically extremely shallow, and are most likely at or near the threshold of formation (see figure 55). The presence of these finer striations indicates that the larger, more readily visible striations are a result of an instantaneous increase in loading at the crack tip. Since the cyclic testing was constant amplitude, the larger striations are most likely due to load shedding from adjacent areas along the crack front.

Specialized SEM analytical techniques were developed to identify and characterize the very faint striations. Plan view, or 0-degree tilt inspection did not reveal the presence of striations. A specimen tilt greater than 60 degrees and specimen rotation of approximately 45 degrees was required to optimize striation resolution.

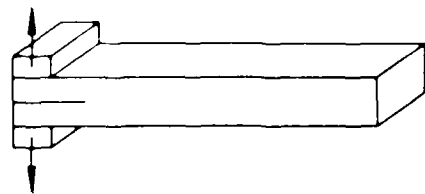
5.8 INTERLAMINAR MODE II FATIGUE

The Mode II fatigue fracture surfaces exhibited the rough topography typical of Mode II interlaminar static specimens investigated earlier in the program. Microscopic features such as hackles and resin microflow were present. Optical microscopy was used to identify striations indicative of cyclic loading.

Following testing, visual examination of the fracture surface revealed arc shaped beach marks, indicative of changes in crack growth and the shape of the crack front as it progressed across the specimen. Each fatigue specimen was tested under two different loading conditions, one having a slightly larger stress amplitude at the crack tip. Each loading condition was performed for 3500 constant amplitude cycles. Macroscopic inspection of the fracture surface also revealed a milky appearance. This is due to light scattering and translucence from the hackle formations.

Optical photomicrographs

Fracture type	Interlaminar mode I tension
Ply layup	[0, 0] 12S
Test type	DCB (fatigue)
• Test condition	70°F
• Fracture between	0/0 plies
Material	Hercules 3501-6/177°C cure AS4 fibers



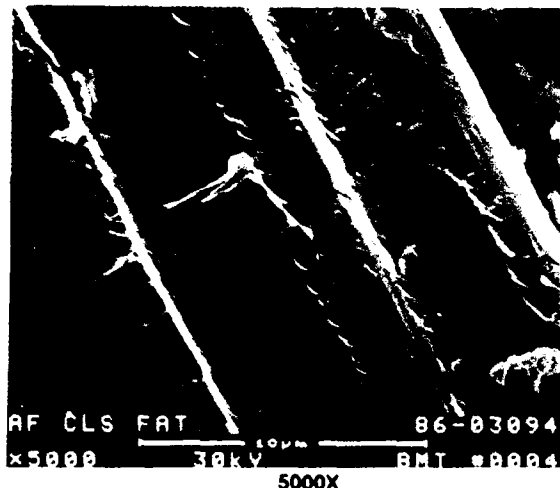
Note: Only a few striations are evident.

Figure 53. Optical Photomicrographs of Fatigue Crack Growth Region for the 0/0 Interface Mode I DCB Specimen

6-B70236-53

SEM photomicrographs

Fracture type	Interlaminar mode II shear
Ply layup	[0] 24
Test type	Fatigue CLS
• Test conditions	70°F, 60% to 20% maximum static fracture stroke
Material	Hercules 3501-6/177°C cure AS4 fibers



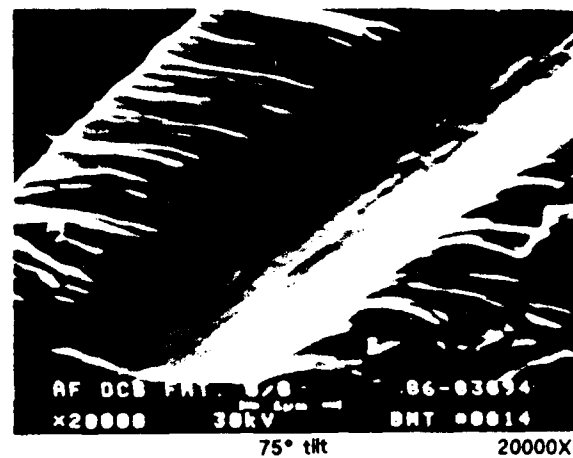
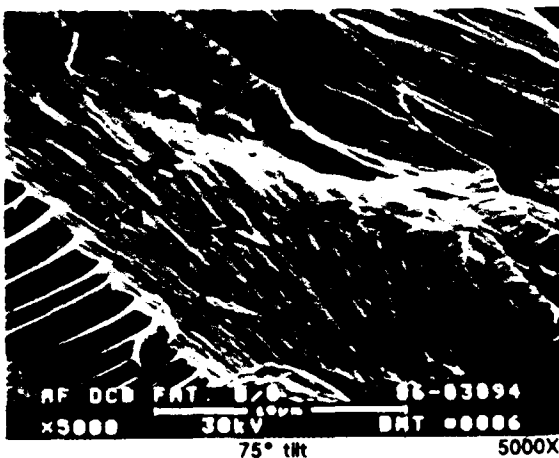
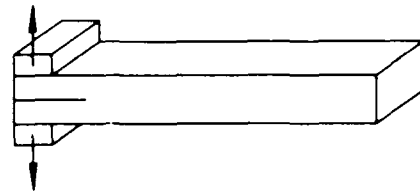
Cyclic loading ranged from 60% to 20% maximum static fracture stroke.

Figure 54. SEM Photomicrographs of Typical Fatigue Striation Formation of Mode II CLS Specimen

6-B70236R1-054

Optical photomicrographs

Fracture type	Interlaminar mode I tension
Ply layup	[0, 0] 12S
Test type	DCB (fatigue)
• Test condition	70°F
• Fracture between	0/0 plies
Material	Hercules 3501-6/177°C cure AS4 fibers



The left photo is in the resin fracture region, while the right photo presents the fiber-matrix interface region.

Figure 55. High Magnification SEM Photomicrographs of Regions That Exhibit Faint Striations

6-B70236-055

As stated previously, optical microscopy of the 0/0 interface specimen fatigue region revealed striations. These striations, or parallel sets of curved lines, were found at the fiber-matrix interface region either at the surface of a single fiber, or at a trough or groove from which a fiber separated (see figures 56 and 57). No striations were evident at the resin regions between fibers, either in the hackled or scalloped surfaces.

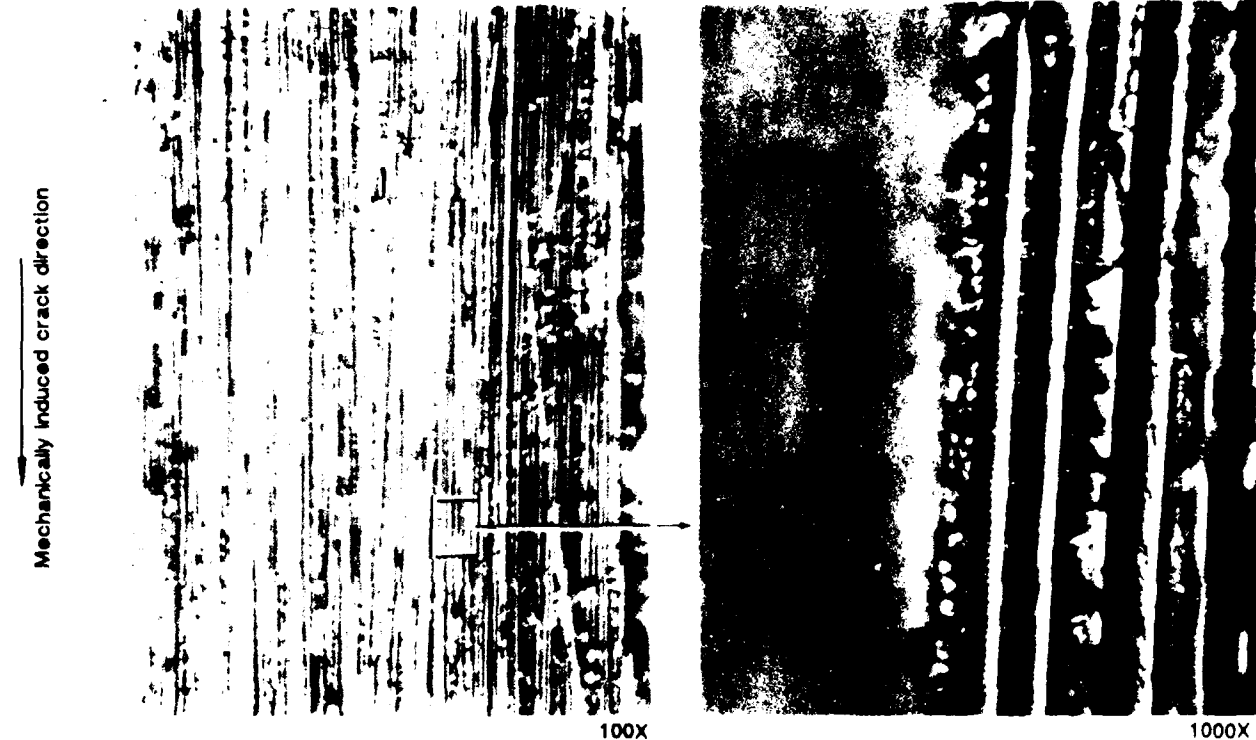
Inspection of crossply interfaces did not reveal striations in fiber-matrix interface regions on fibers other than those oriented in the 0-degree direction, parallel to induced crack growth (see figure 58).

The striations were not easily found nor readily apparent from initial inspection with the optical microscope. Previous Boeing IR&D studies of Mode II fatigue specimens indicated that identification of striations was a difficult task, even at loadings that were much higher than used in this program (95% G_{max} versus 60% and 80% G_{max}). Since we knew cyclic growth occurred, careful inspection was performed. This inspection was much more detailed and intensive than we would normally use during typical crack mapping procedures. We have learned that when performing fractographic analysis, an inspector must be aware of the difficulties of identifying evidence of cyclic loading; and if one suspects such an environmental condition, a slow, careful inspection is usually required.

As stated previously, the striations were found to occur along the fiber-matrix interface. Closer inspection revealed that the spacing between striations would greatly vary over the length of a fiber, as much as an order of magnitude differences within a single field of view at 600X magnification. This is quite different from that found in metallic materials that undergo cyclic crack growth. Metals, most likely due to their more homogeneous nature, tend to exhibit fairly evenly spaced striations, from which striation counts can be obtained. These graphite/epoxy specimens, on the other hand, are found to exhibit a great inconsistency and range, indicative of load shedding and the meniscus type crack front due to interaction at the crack tip and the fibers. This inconsistency prevents an investigator from performing a striation count to determine the total number of cycles along a crack. One may, however provide an average, or range of growth rates, from which simple qualitative comparisons may be made for stress analysis. Previous studies at Boeing have indicated that striation spacing increased with increased level of loading amplitude (G_{max}) during cyclic testing. These results indicate that an investigator can tell the stress analyst whether cracking

Optical photomicrographs

Fracture type	Interlaminar mode II shear
Ply layup	[0, 0] 12S
Test type	Fatigue CLS
• Test conditions	70°F
• Fracture between	0/0 plies
Material	Hercules 3501-6/177°C cure AS4 fibers



Note the finely spaced striations present along a fiber-matrix groove.

Figure 56. Optical Photomicrographs of Intended Fracture Plane Between 0-deg Plies for the CLS Fatigue Specimen (100X and 1000X)

6-B70236R1-056

Optical photomicrographs

Fracture type	Interlaminar mode II shear
Ply layup	[0, 0] 12S
Test type • Test conditions • Fracture between	Fatigue CLS 70°F 0/0 plies
Material	Hercules 3501-6/177°C cure AS4 fibers



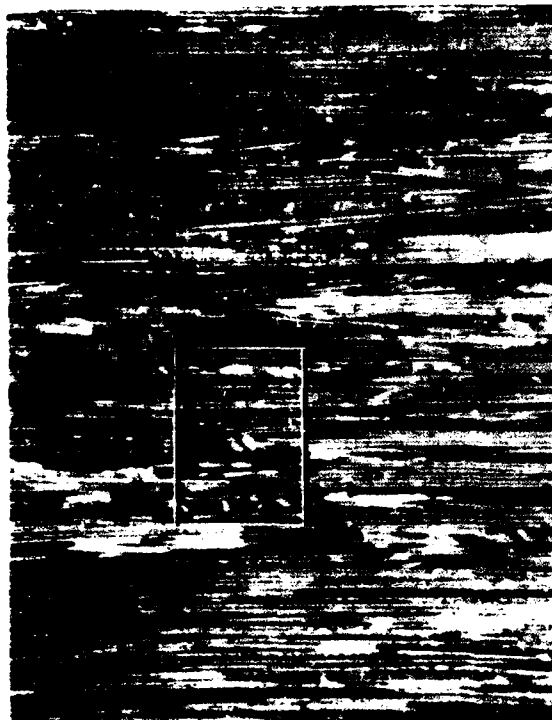
Note the large variation in striation spacing, both along each fiber and between the two adjacent fibers.

Figure 57. Optical Photomicrographs of Intended Fracture Plane Between 0-deg Plies for the CLS Fatigue Specimen (400X and 1000X)

6-B70236-057

Optical photomicrographs

Fracture type	Interlaminar mode II shear
Ply layup	[0, 0] 12S
Test type • Test conditions • Fracture between	Fatigue CLS 70°F 0/90 plies
Material	Hercules 3501-6/177°C cure AS4 fibers



100X



400X

No striations were identified on the fibers oriented in the 90-deg direction.

Figure 58. Optical Photomicrographs of Intended Fracture Plane Between 0/90-deg Plies for the CLS Fatigue Specimen (100X and 400X)

6-B70236-058

progressed by high cycle/low stress fatigue or by low cycle/high stress loading conditions.

Following optical microscopy, SEM examination of the fracture surfaces involved more detailed, high magnification analysis and photo documentation of specific salient features and trends. SEM analytical techniques were developed to further reveal the faint striation details present on the fracture surface. Two major changes in specimen angulation resulted in significantly better resolution described as follows:

- Tilting the specimen beyond 60° tilt with respect to the incident beam to increase striation contrast.
- Rotating the specimen such that the fibers were oriented at approximately minus 30-degree rotation (from vertical) to the viewing screen so the secondary electron detector received the highest signal.

Figure 59 presents a comparison of a single field at 0-, 30-, and 65-degree tilts. Note that the striations are not resolvable or high enough contrast to identify in the 0- and 30-degree tilts.

Optical microscopy did not identify striations in the lower amplitude fatigue cycle region (20% to 60% maximum). SEM analysis using high tilts and optimum specimen rotation resulted in identification of striations which were much finer and closer spaced than those found in the high amplitude region (40% to 80% maximum). Additionally, these striations were very inconsistent in spacing. As with metals, this observation suggests fatigue crack growth is at, or very near, the threshold of striation formation. At low stress intensities of the crack tip, slight variations in localized loading (due to the load shedding nature of the fibers) can cause inconsistent crack front behavior as illustrated in figure 60.

Figure 61 presents the consistent behavior of striation formation found in the higher amplitude fatigue cycle region (40% to 80% maximum stroke). As anticipated, striation spacing is much greater than the very fine striations in the low amplitude specimens (20% to 60% maximum stroke) presented in figure 60. The conclusion made is that an increase in G_{max} with constant ΔG results in an increase in striation spacing, similar to the effect found in metals and increasing K_{max} with constant ΔK .

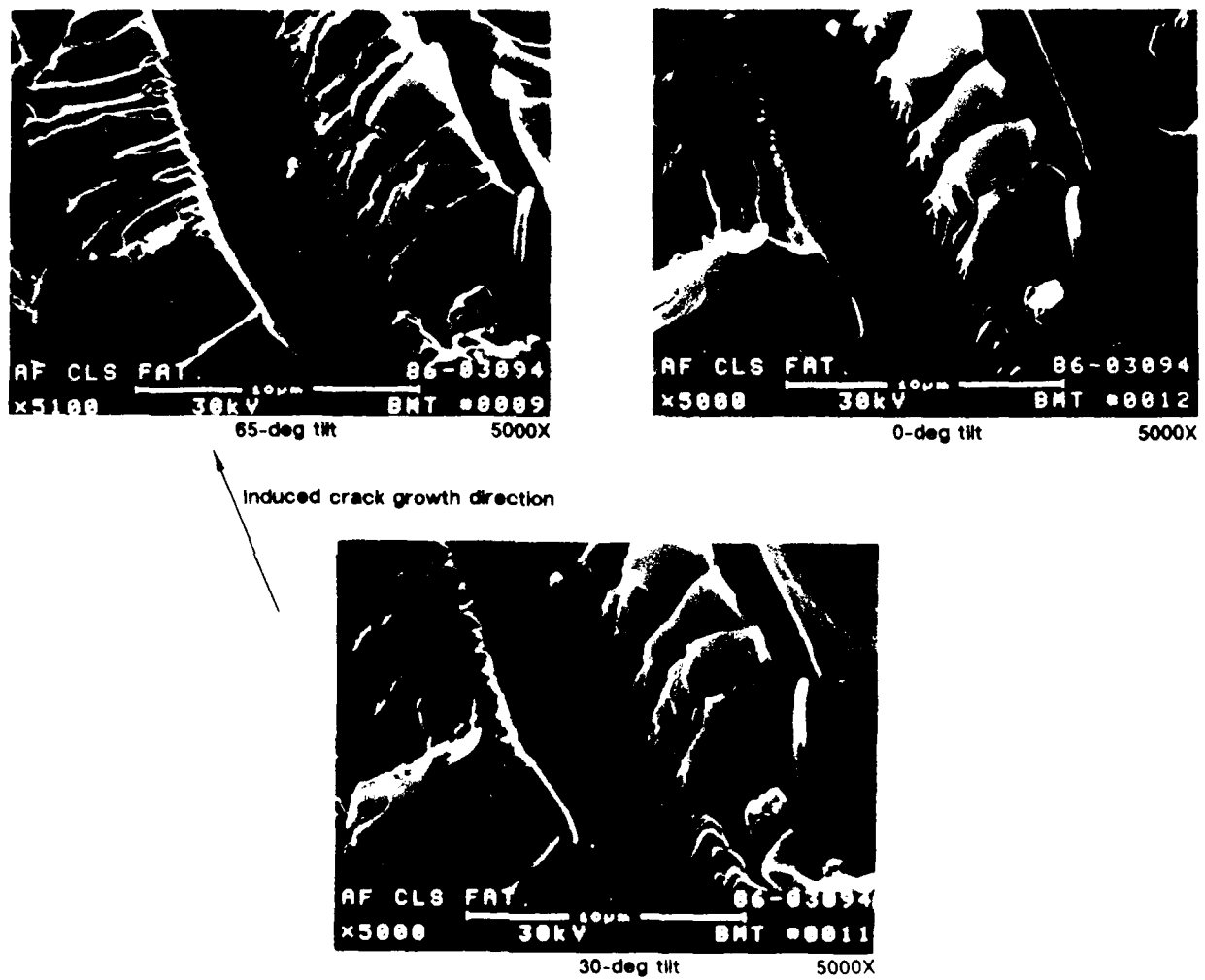
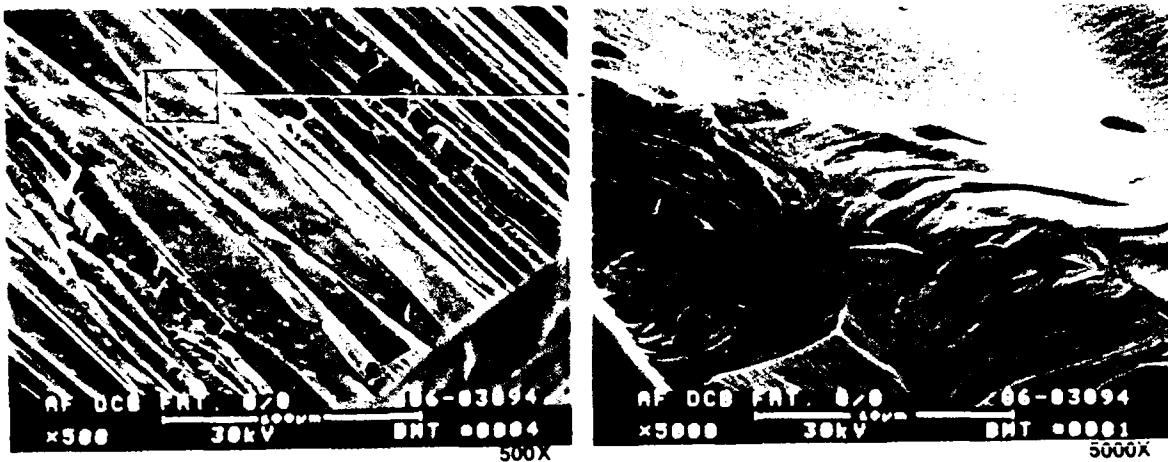
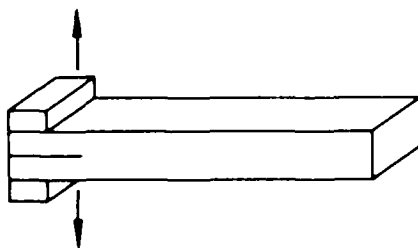


Figure 59. SEM Photomicrographs of Effect of Tilt on Striation Resolution

6-B70236-059

SEM photomicrographs

Fracture type	Interlaminar mode I tension
Ply layup	[0, 0]12S
Test type	DCB (fatigue)
• Test conditions	70°F
• Fracture between	0/0 plies
Material	Hercules 3501-6/177°C cure AS4 fibers



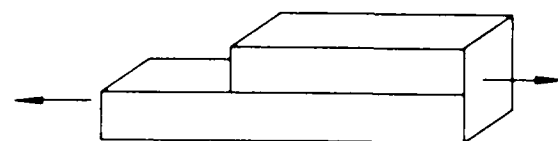
Note smooth fracture topography and faint striations in right photo.

Figure 60. SEM Photomicrographs of Effect of Tilt on Striation Resolution (500X and 5000X)

6-B70236-060

SEM photomicrographs

Fracture type	Interlaminar mode II shear
Ply layup	[0] 24
Test type • Test conditions	Fatigue CLS 70°F, 80% to 40% maximum static fracture stroke
Material	Hercules 3501-6/177°C cure AS4 fibers



Cyclic loading ranged from 80% to 40% maximum static fracture stroke.

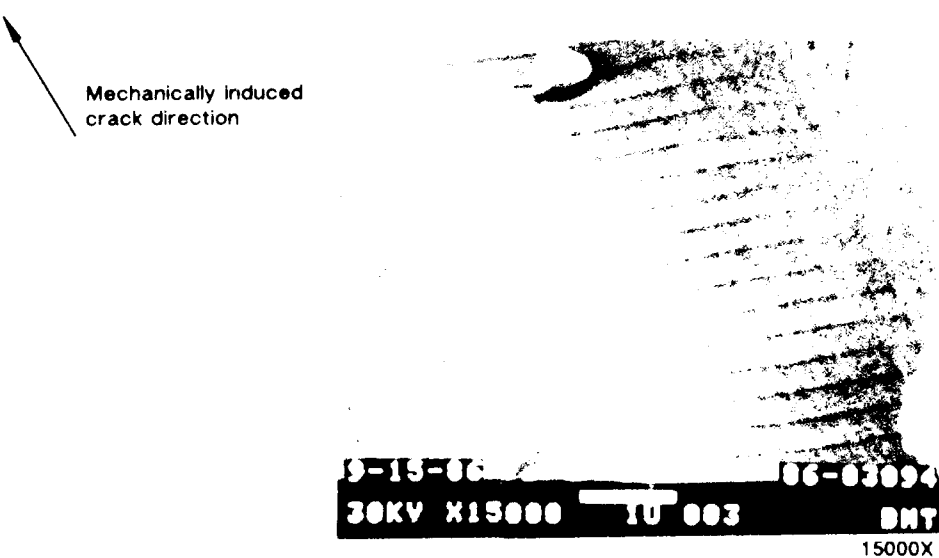


Figure 61. SEM Photomicrographs of Typical Fatigue Striation Formation of Mode II CLS Specimen

6-B70236R1-061

5.9 LAMINATE FLEXURE

Specimens failed under laminate flexure proved interesting in that pronounced differences in failure mode occurred for each specimen layup. Figure 62 illustrates each of these failure modes. As shown, failure of the 0/90 and quasi-isotropic laminates occurred along the tensile surface and involved both translaminar splitting and delamination. In contrast, failure of the 0-degree specimen occurred through the full specimen thickness with very little delamination. Failure of the +45/-45 specimen occurred without any identifiable conditions of fracture. This condition clearly illustrates the inadequacy of trying to characterize all flexural failures based on the appearance of 0-degree coupons as some authors have attempted.

5.9.1 0-Degree Layup

Failure of this specimen was found to occur through a combination of tensile and compression fiber fracture. As illustrated in Figure 63, distinct zones of each failure mode were observed separated by a line corresponding approximately to the specimen neutral axis. The detailed examination of each of the failure zones revealed the following conditions:

- Extensive microbuckling and postfracture damage in compression failure modes.
- Tensile fiber fracture and pull out in tensile fiber areas.

In a manner similar to the singular translaminar compression failure specimens previously evaluated within this program, detailed examinations of the compressive failure surface revealed no morphological clues as to the direction of crack growth. However the tensile fracture zone exhibited features corresponding to the direction of crack growth. As illustrated in Figure 63, examination of the tensile area of fracture reveals a coarser pattern of lines running between the specimen edge and neutral axis. These lines appear analogous to ratchet lines often described in metals, where these lines are formed by the intersection of parallel zones of crack growth. Given this interpretation, these optical lines (see figure 63) suggest that crack initiation occurred at multiple locations along the specimen tensile surface and progressed inwards towards the specimen center. Evidence supporting this interpretation can be seen in figure 64 in which the direction of individual fiber breakage was found to occur parallel to the ratchet lines and towards the specimen centers.

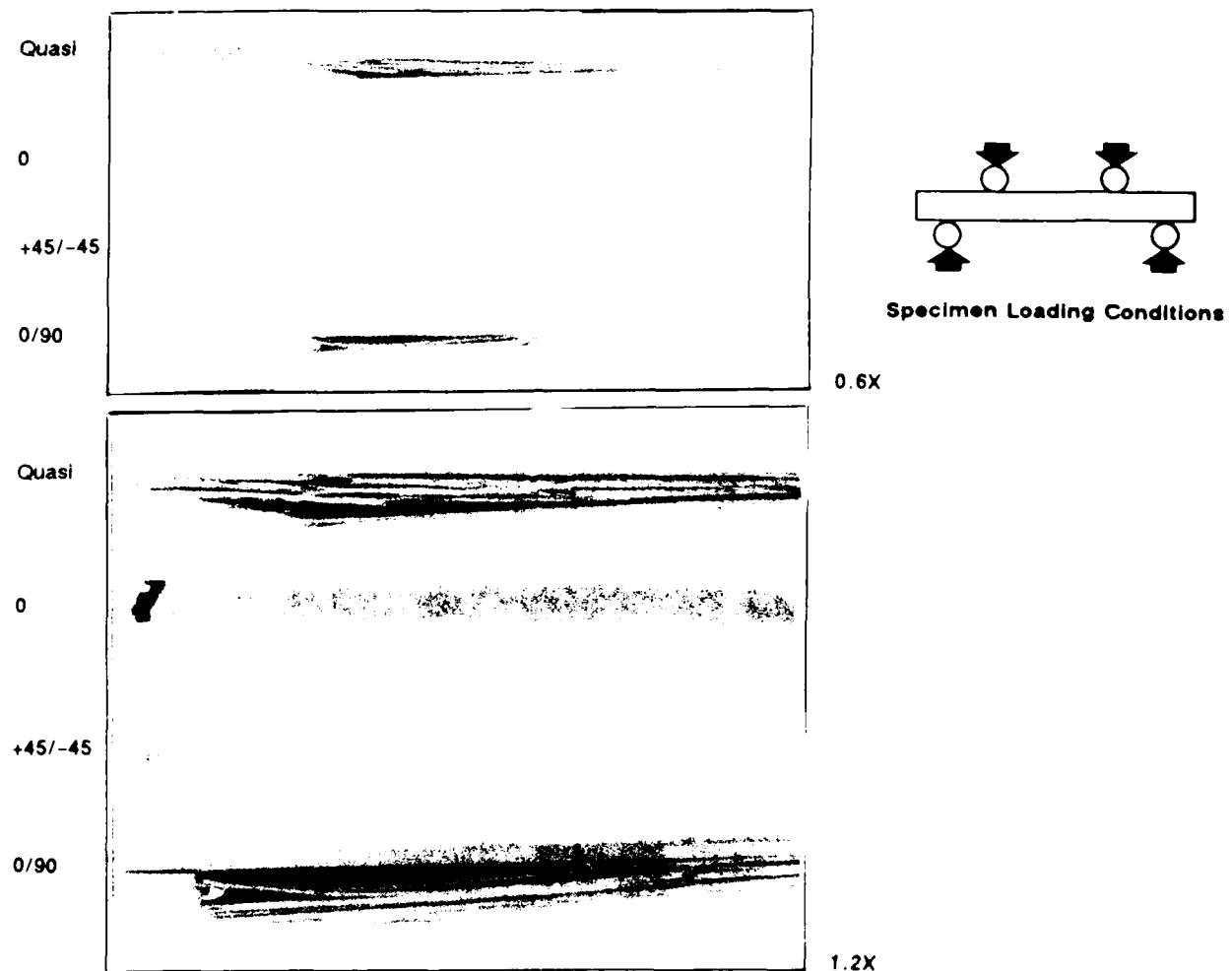


Figure 62. Overall Macrographs of Laminate Flexure Specimens

6-B70236-062



Notice the distinct fracture morphology difference between the tensile and compression regions.

Figure 63. Macrograph of Fracture Surface From the Unidirectional 0-deg Laminate Flexure Specimen

SEM photomicrographs

Fracture type	Translaminar/interlaminar
Ply layup	[0]32
Test type	Laminate flexure
• Test conditions	70°F
• Fracture	Fiber end
Material	Hercules 3501-6/177°C cure AS4 fibers

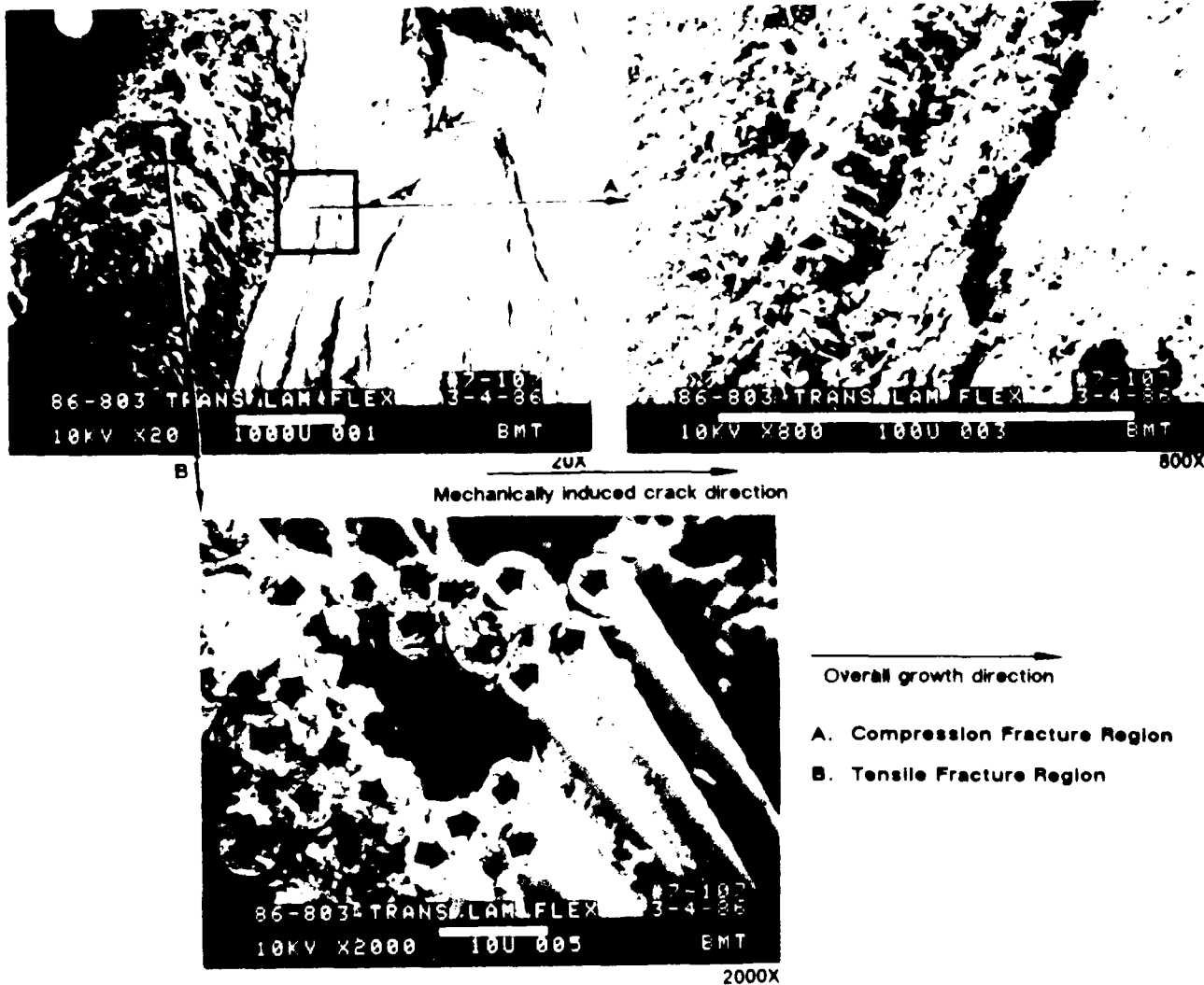
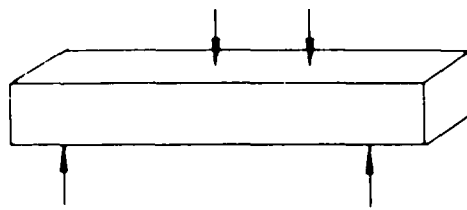


Figure 64. SEM Photomicrographs of Unidirectional 0-deg Laminate Flexure Specimen

6-B70236R1-064

In general, the fracture behavior of this specimen illustrates several notable considerations. First, ratchet lines appear to be a viable means of macroscopically determining the direction of tensile fiber fracture. This observation is particularly helpful because the scanning electron microscopic examination of fiber end fracture directions is tedious and time consuming. Secondly, line origins (multiple origins along one edge) exist in composites. This finding, while in itself not particularly surprising, demonstrates that potential investigators should be aware that crack initiation does not necessarily initiate at a single point. Thirdly, the dual compression/tension failure mode illustrates the limitations of our analysis methods. Since an origin for the compression fracture surface was unable to be identified, it remains unclear whether the tensile origins occurred before or after compression failure initiation. As a result, an accurate reconstruction of the sequence of failure could not be accomplished.

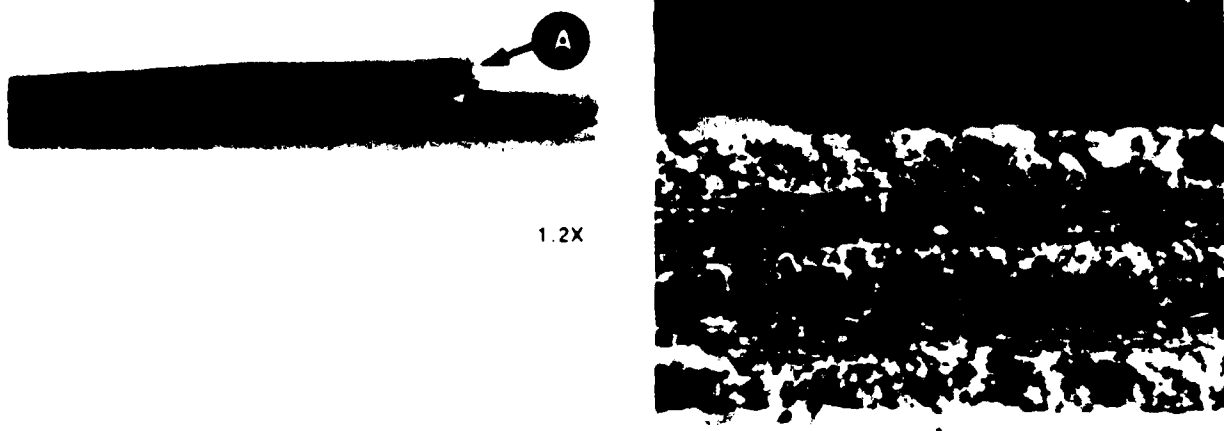
5.9.2 0/90 and Quasi-Isotropic Laminates

As shown in figure 62, both the 0/90 and the quasi-isotropic laminates exhibited similar failure modes. Failure of these specimens typically involved the following characteristics:

- Translaminar tensile failure from the tensile loaded surface toward the specimens neutral axis.
- Extensive delamination of the plies located on the tensile side of the beam neutral axis.

In examining the translaminar tensile failure portion of these specimens, many of the same features noted for all the 0-degree specimens were also observed. As shown in figure 65, ratchet marks are apparent along the specimen outer surface on those fibers oriented longitudinally along the specimen axis. These ratchet marks indicate that tensile fiber fracture initiation occurred at multiple origins along the outer surface and that crack propagation progressed inwards towards the specimen center.

Inspection of delaminations on the tensile side of the specimen revealed that propagation occurred by inplane Mode II shear fracture. As presented in figure 66, scallop and hackle type features were observed throughout the specimen fracture surface. The direction of crack propagation for these features were assigned utilizing the same methods described for the compression after impact specimen. As shown,



A Ratchet lines can be seen in the trans-laminar fiber-end view of the 0-deg plies in the tensile fracture region. 60X

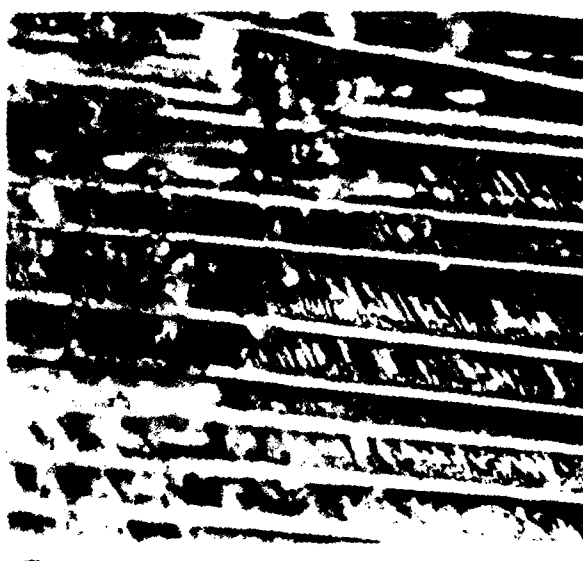
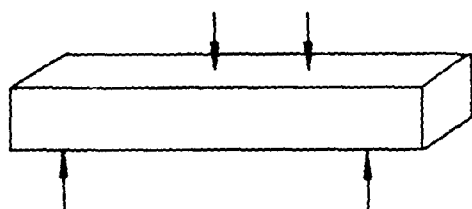
Figure 65. Photomacrographs of 0/90 Laminate Flexure Specimen

6-B70236R1-065

Optical photomicrographs

Fracture type	Translaminar/Interlaminar
Ply layup	[0, 90]16S
Test type	Laminate flexure
• Test conditions	70°F, dry
• Fracture between	0/90 plies
Material	Hercules 3501-6/177°C cure AS4 fibers

Mechanically induced crack direction

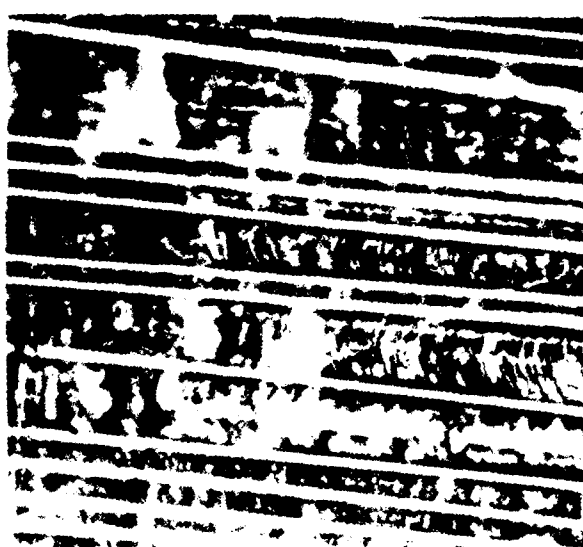


400X



Legend:

- Mode I tension dominated crack growth direction
- ↔ Mode II shear dominated crack growth directions



400X

Figure 66. Interlaminar Fracture Surface Characteristics of the 0/90 Laminate Flexure Specimen

6-B70236R1-066

delamination was found to initiate adjacent to the translaminar tensile fracture and progress axially down the specimen length.

The above findings represent a complex failure condition likely to be encountered in many routine failure analyses where both delaminations and translaminar failures exist together. In order to reconstruct the sequence of such failures, the analyst must determine which of these failure modes occurred first. For the samples described above, the logical order of failure consists of translaminar tensile failure followed by delamination. This order appears logical since each delamination was initiated along the translaminar failure and progressed away from it, rather than towards it.

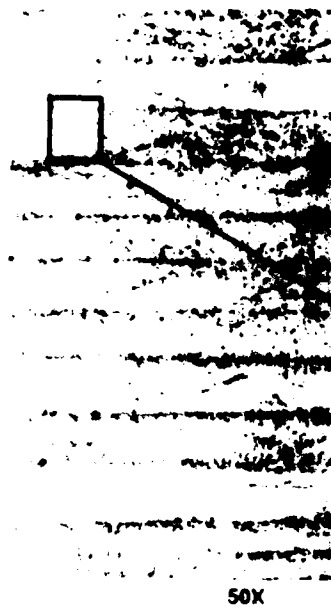
5.9.3 +45/-45 Laminates

As discussed earlier, failure of this laminate orientation did not produce any discernable conditions of fracture. As a result detailed fractographic analyses of this specimen were not carried out. However, in order to better understand this specimen's behavior, optical cross sections were prepared parallel to the specimen axis. As illustrated in figure 67, examination of this specimen revealed multiple intralaminar microcracks parallel to the direction of fiber reinforcement. No interlaminar cracks were identified between the laminate plies.

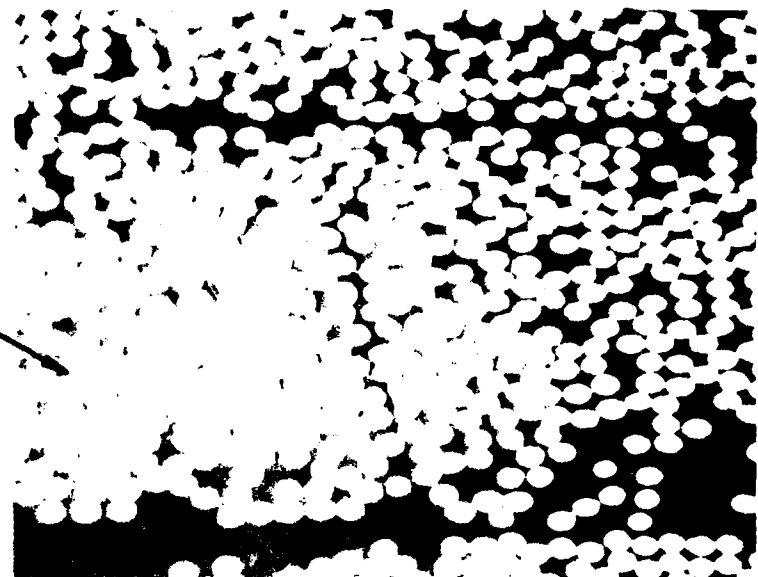
5.10 FASTENER-FILLED-HOLE (Tension and Compression)

The following paragraphs describe results of characterization of the fracture morphology and failure of the fastener-filled-hole tension and compression specimens. The tension specimens were found to exhibit fastener head pull out, delamination of surface plies around the hole, and lack of delamination in the central ply region. Similarly, the compression specimens had extensive translaminar damage associated with fastener head pull out and slight surface delaminations. For the compression specimen, the central plies were found to exhibit extensive delamination that resulted in compression buckling and macro kinking near the hole. These differences were visually identifiable and thus allowed identification of specific loading type (compression or tension) at failure.

These specimens were fabricated from a 32 ply quasi-isotropic laminate. A titanium 3/16-in flush head Hi-Lok fastener was used to hold two plank sections with a 2-in



50X



400X

Testing damage was limited to localized intralaminar cracking within the plies.

Figure 67. Optical Photomicrographs of Cross Sections From the +45/-45 Laminate Flexure Specimen

6-B70236-067

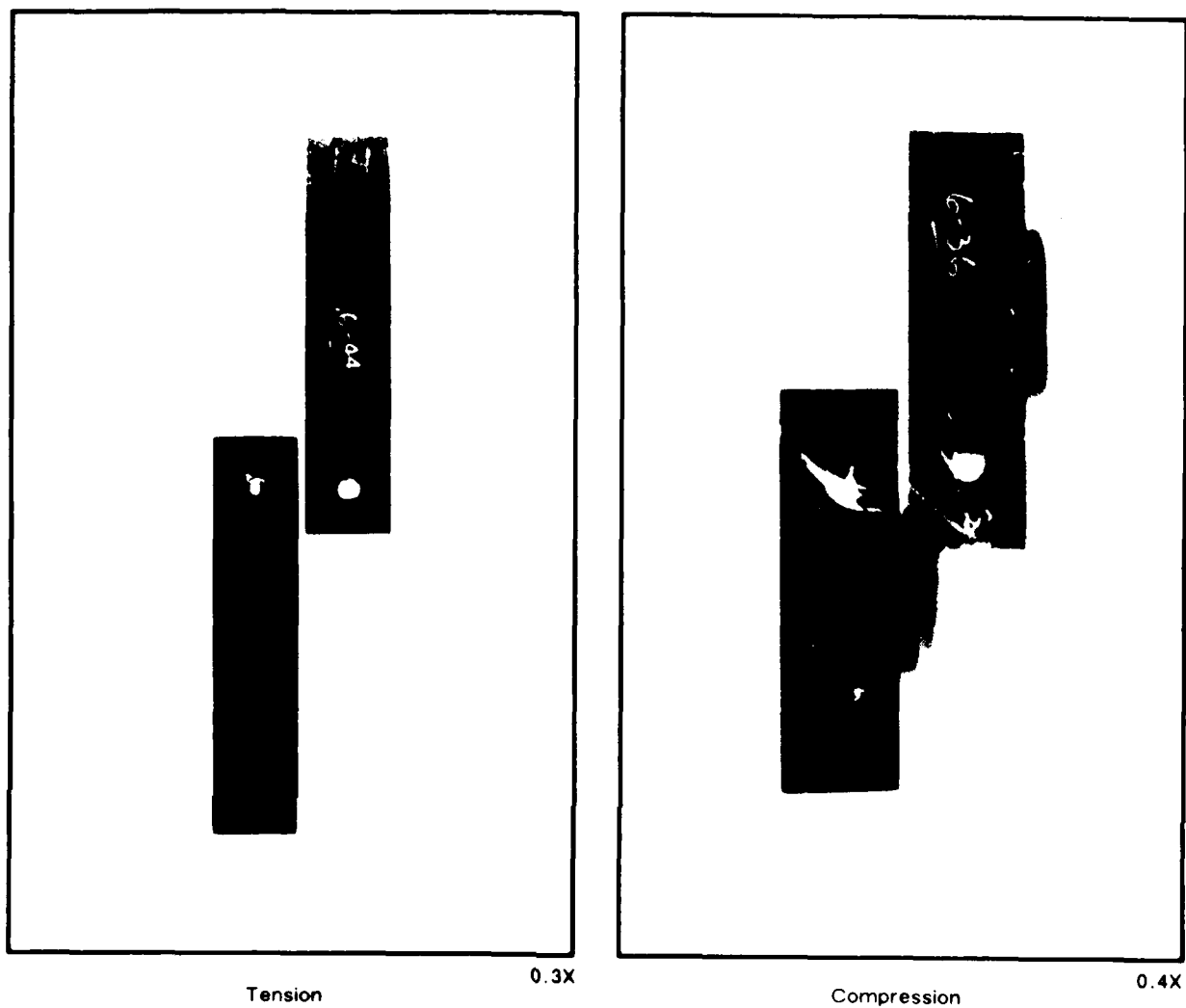
overlap. Figure 68 presents the tension and compression overall photos following testing. Testing involved loading until joint failure, usually when the fastener had rotated and was pulled through a plank. Visual inspection of the tension specimen revealed extensive through-thickness translaminar bearing fracture where the fastener was dragged through the laminate during testing, as shown in figure 69. The direction of this damage with respect to the fastener hole was found to indicate the direction of axial loading (in this case, tension). As can be seen, a few surface plies were found to be delaminated and pushed up from the surface. No internal delamination damage was visually identified. Further cross sectional optical inspection indicated internal ply damage was restricted to the immediate fastener pull out region. The side view illustrated in figure 70 shows the lack of central ply delamination damage for the tension specimen.

As found for the tension specimen, the compression specimen exhibited extensive translaminar damage associated with fastener pull out. Similarly, the direction of axial loading for the compression specimen could be identified by the location of damage with respect to the fastener hole (see figure 69). During specimen testing, which required several minutes to fail the specimen at 0.05 in/min crosshead rate, visual inspection indicated that the fastener head rotated and was being pulled through the laminate. Near the completion of testing, the laminate started to delaminate within the central plies within each plank, followed by plank failure from compression buckling, with visual kinking, as shown in figure 70.

Results from these specimens indicated that the direction of fastener joint loading could be identified, both by the direction of fastener pull out damage and evidence of central ply laminate delaminations for the compression specimen. For this complex fracture condition, it was found that visual macroscopic analysis provided all necessary evidence to properly perform failure analysis, particularly since delaminations did not play a key role in providing failure modes, sequences or causes.

5.11 DRILL BREAKOUT

The drill breakout specimens exhibited extensive backside breakout damage. The backside delaminations exhibited mixed mode failure morphology (initiating at the bore edge) and machining debris was lodged into the delamination cracks. Optical and SEM analyses were performed to characterize the damage region. Backside delaminations,



Note: The planks were separated for photo documentation.

Figure 68. Overall Photomacographs of the Fastener-Filled-Hole Tension and Compression Specimens Following Testing



Tension

1.5X



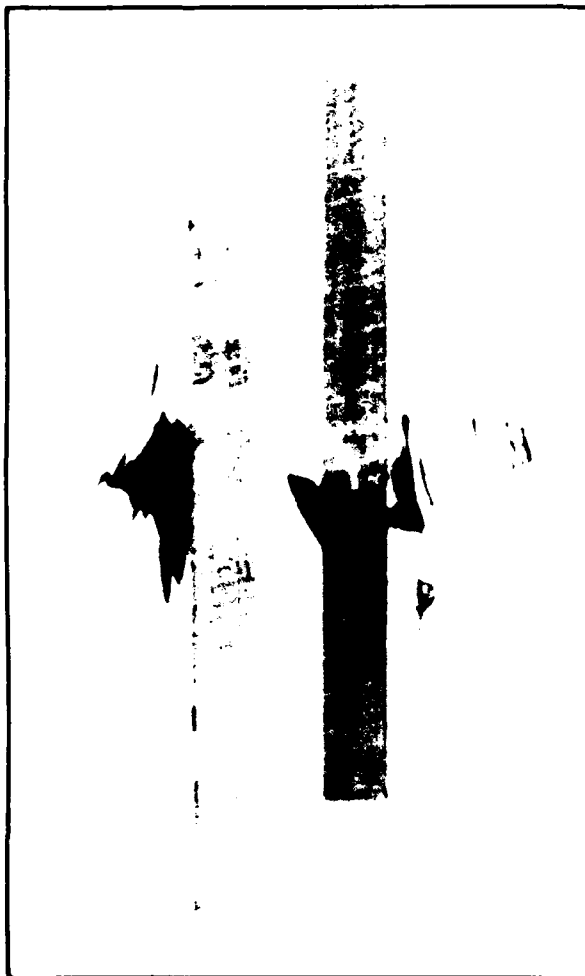
Compression

1.5X

Note: Notice extensive translaminar damage from fastener pull out.

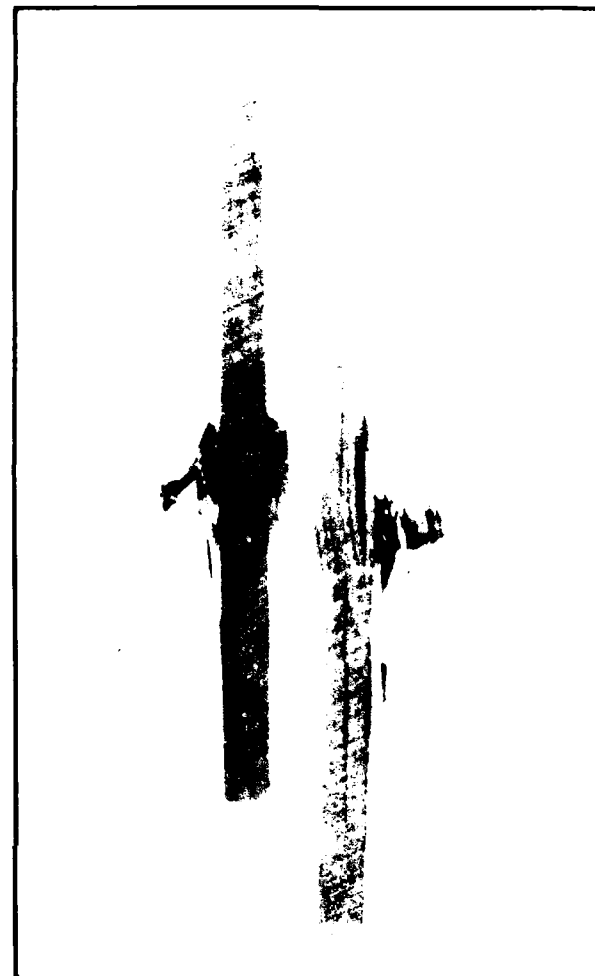
Figure 69. Damage to Fastener-Filled-Hole Tension and Compression Specimen

6-B70236-69



Tension

2.0X



Compression

1.7X

Note: Notice lack of internal ply damage on tension specimen and extensive compression buckling of the right plank of the compression specimen.

Figure 70. Edge View of Fastener-Filled-Hole Tension and Compression Specimens

visually identifiable, often extended more than 0.50-in from the hole edge (see figure 71).

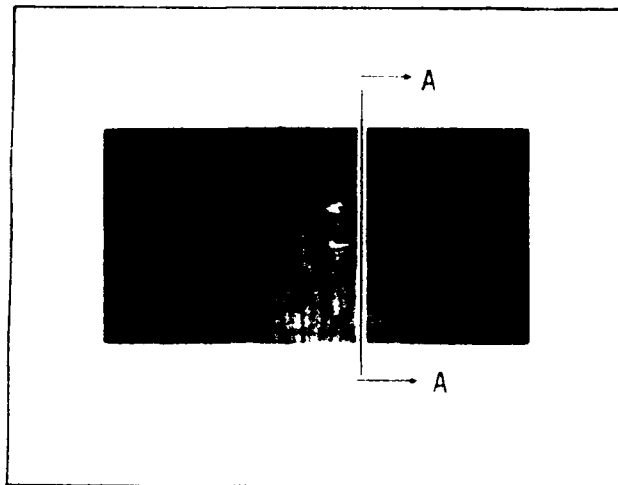
Optical microscopy consisted of examination of delamination surfaces and cross sections through the laminate. The cross sections showed delaminations were not confined to the bottom few plies, and that damage occurred on as many as seven plies from the back surface, as shown in figure 71. Optical examination and SEM microscopy of several of the largest delamination surfaces identified slightly tilted hackles (lamellar resin platelets), similar to those identified for the interlaminar MMF specimens. Many fractured resin particles were present on all surfaces, sometimes actually entirely covering the delamination surface. Although all delaminations exhibit a small amount of resin "dust" due to the fracture process, the massive amount of dust on the drill breakout specimens is most likely due to the drilling process. The features of hackles and machining debris are presented in figure 72.

5.12 INTERLAMINAR DEFECT/CONTAMINATION, MODES I AND II

Interlaminar defect/contamination specimens exhibited unique and easily distinguishable features representative of each defect type. The three defect/contamination types were:

- Voids-produced by lack of autoclave pressure during cure processing.
- Teflon-produced by wiping the prepreg plies at the desired delamination interface with a Teflon paddle.
- Frekote-produced by spraying Frekote on the prepreg plies at the desired delamination interface during laminate layup.

Figure 73 illustrates the fracture surface morphology characteristic of delaminations produced in the void defect specimens. The voids were identified by both optical and SEM examination as semielliptical regions, with a large range in size. High magnification SEM inspection of the void region revealed a smooth, featureless, resin surface, with underlying fibers. The fracture surface surrounding the void regions exhibited a matrix fracture morphology typical of the induced mode (that is, DCB Mode I had river marks and ENF Mode II exhibited hackles). Therefore the effect of voids on the fracture process itself appeared to be minor, mostly a reduction in surface area involved in matrix fracture. Crack propagation directions for Mode I were coincident with the direction of imposed macroscopic fracture. The fracture mode for the DCB



Note: The photo above illustrates the extent of backside damage around the drilled hole and the right photo below presents cross-section A-A.

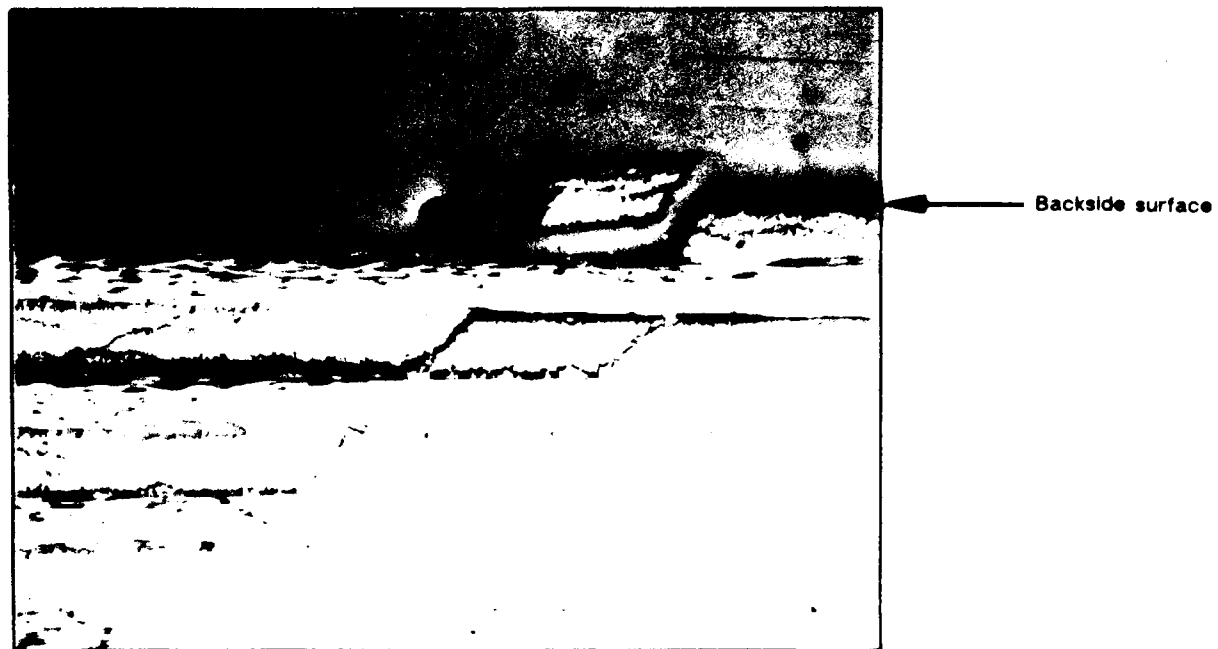
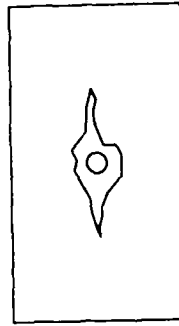


Figure 71. Visual and Optical Details From the Drill Breakout Specimen

6-B70236R2-71

SEM photomicrographs

Fracture type	Interlaminar mode I tension
Ply layup	[0, 0]16S
Test type	Drill breakout
• Test conditions	Dry 0/0 piles
• Fracture between	
Material	Hercules 3501-6/177°C cure AS4 fibers



Note: In the right photo, the fracture surface is entirely covered with resin debris from the drilling operation.

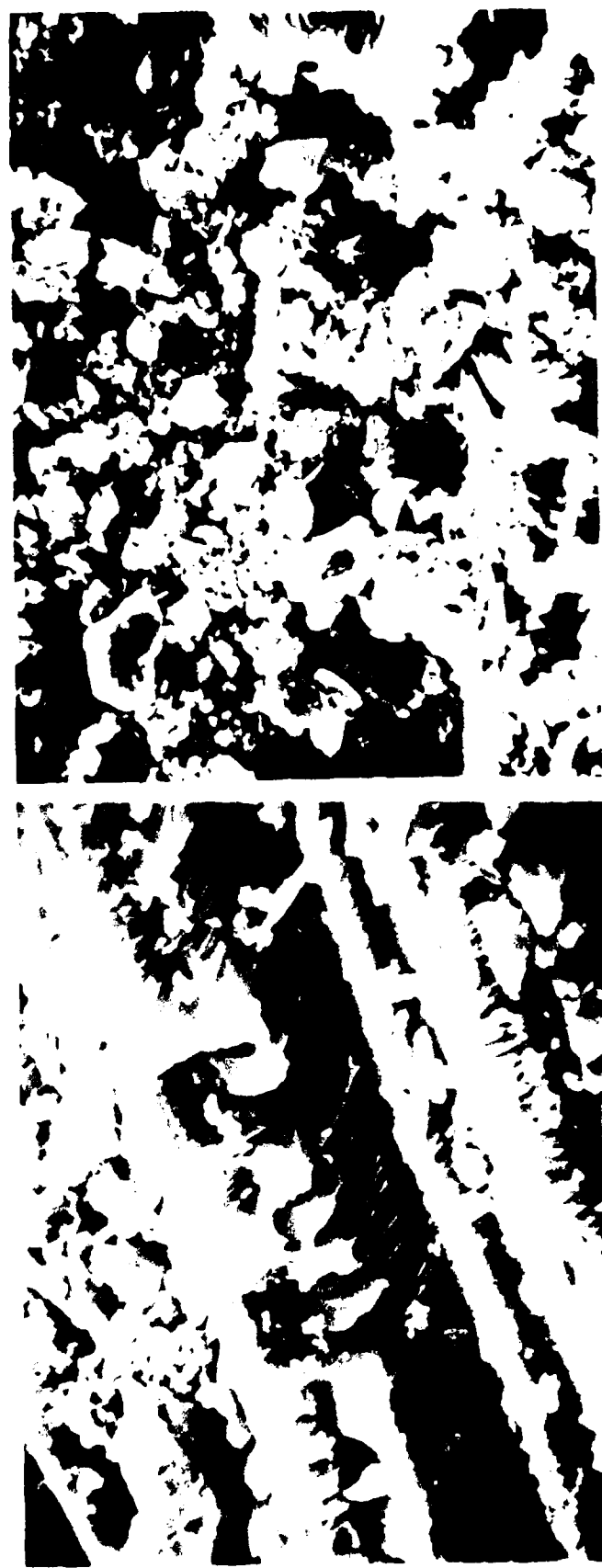
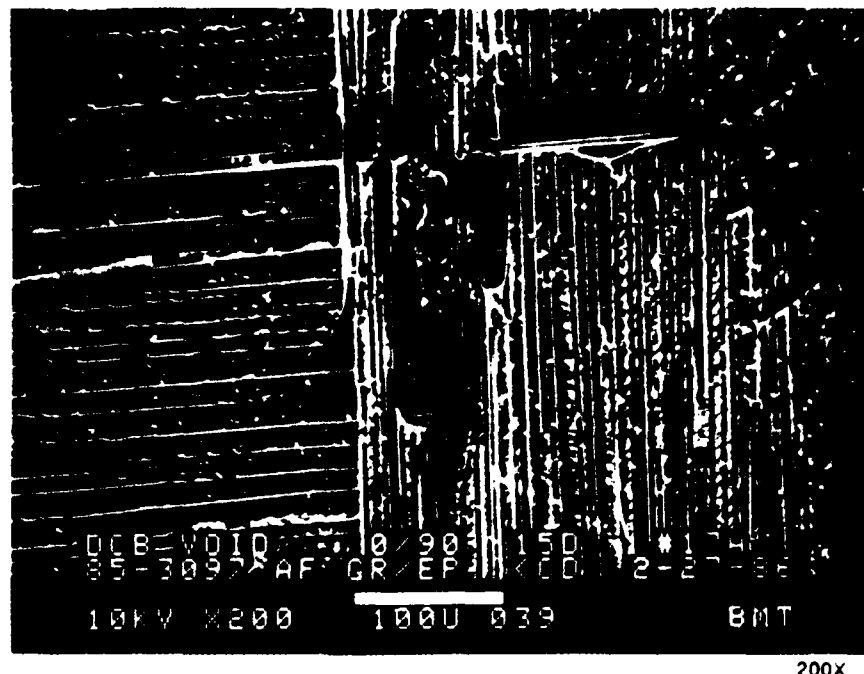
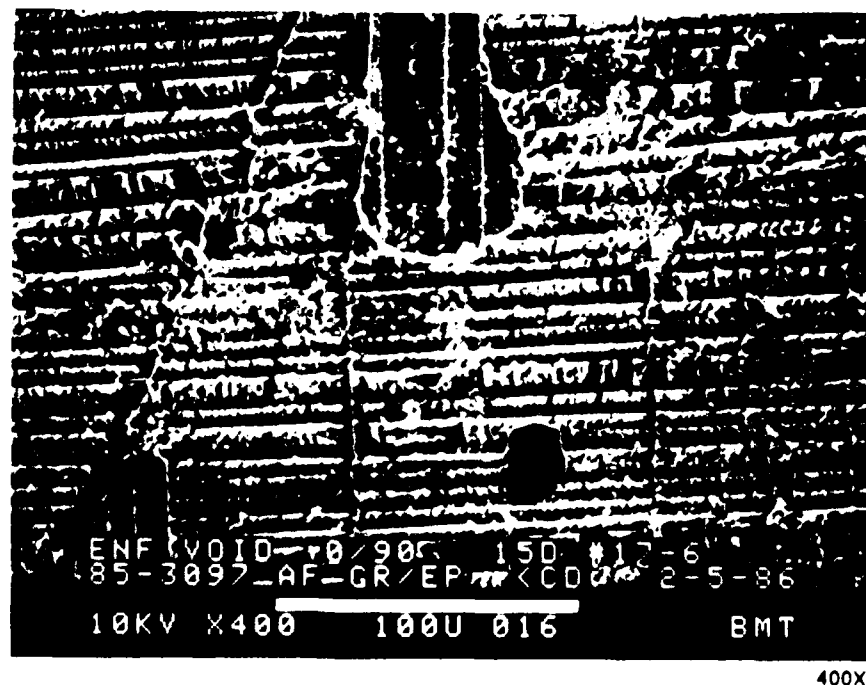


Figure 72. SEM Photomicrographs of Typical Delamination Surface Features for the Drill Breakout Specimen



(a) DCB Mode I 0/90 Cross-Ply Interface

Induced crack growth direction



(b) ENF Mode II 0/90 Cross-Ply Interface

Note: The elliptical shaped regions are voids.

Figure 73. Typical Fracture Surface Morphology of Void Defect Specimens

6-B70236-73

and ENF specimens were easily identified using the methods developed earlier on singular failure mode specimens.

Figure 74 illustrates the fracture surface morphology characteristic of delaminations produced in the Teflon defect specimens. The localized Teflon coated regions were characterized as interconnected and fibrous appearing, without resin fracture features. The fibrous appearance was elongated in the direction of wiping of the Teflon paddle during panel layup. The matrix resin fracture surface surrounding the Teflon regions exhibited morphologies typical of the Mode I and Mode II fracture conditions for the DCB and ENF specimens, respectively. Using river mark patterns in the uncontaminated regions, the crack propagation directions for the Mode I tension specimens were found to propagate in the direction of imposed macroscopic testing (away from the FEP implant).

Figure 75 presents the typical fracture surface morphology found on delaminations produced with Frekote defect conditions. The localized Frekote fracture regions were characterized as interconnected and very smooth, without resin fracture features, indicative of adhesive type separation. As found for the other defect types, the surrounding resin matrix exhibited typical fracture morphologies for both the DCB and ENF specimens. Additionally, crack propagation directions for the Mode I specimens were found to be coincident with the observed direction of imposed macroscopic crack growth.

To conclude, optical and SEM analysis of the defect specimens identified the following characteristics:

- Each defect type was easily identifiable and distinguishable from one another.
- Each defect type exhibited localized regions which lacked resin fracture features, indicative of little or no fracture toughness.
- Mode I crack propagation directions were determinable through the use of mapping river mark patterns in the unaffected regions.
- The imposed load states of fracture were identifiable and could be differentiated from one another (Mode I versus Mode II).



(a) DCB Mode I 0/90 Cross-Ply Interface
Induced crack growth direction

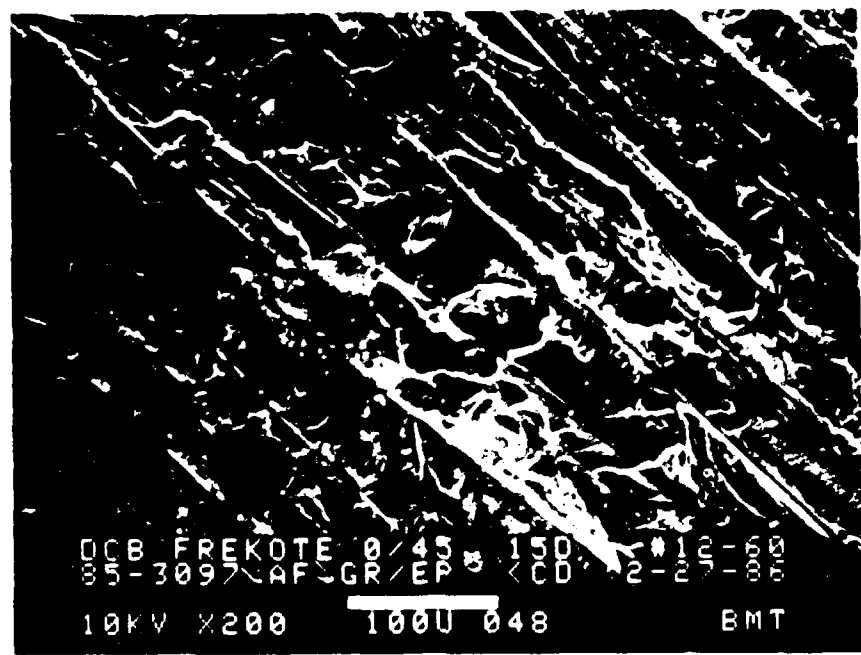


(b) ENF Mode II 0/90 Cross-Ply Interface

Note: The fibrous regions contain smeared Teflon, which does not exhibit fracture details.

Figure 74. Typical Fracture Surface Morphology of Teflon Defect Specimens

6-B70236R1-074



(a) DCB Mode I 0/45° Cross-Ply Interface

Induced crack growth direction

200Y



(b) ENF Mode II +45/-45° Cross-Ply Interface

Figure 75. Typical Fracture Surface Morphology of Frekote Defect Specimens

6-B70236R1-075

5.13 COMPRESSION AFTER IMPACT (CAI)

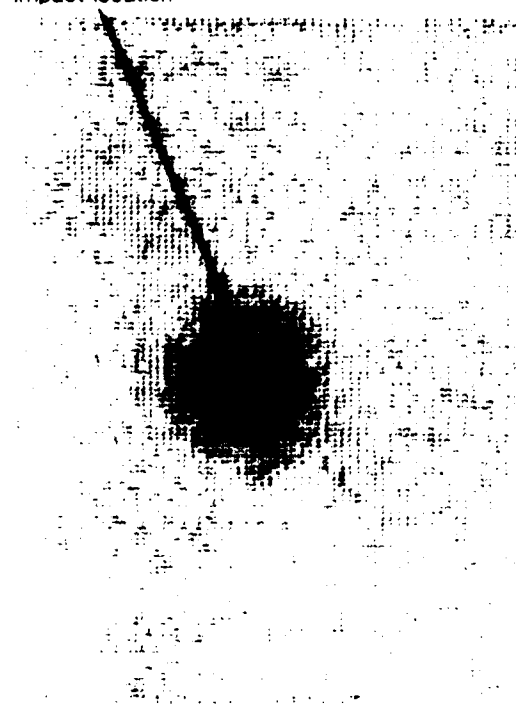
In general, composite materials are particularly sensitive to damage generated by foreign object impact. This sensitivity is most dramatic under axial compression where reductions in strength in excess of 50 percent can occur at moderate impact energy levels. Because of this sensitivity, notch or damage initiated compression failure represents one of the more common failure modes likely to be encountered for inservice structures.

As part of task 3, the analysis of CAI specimens evaluated the degree to which singular failure characteristics and analysis methods could be translated to more complex failure conditions similar to those likely to be encountered in real world failure analyses. The analyses methods developed on singular failure specimens in task 3A were found to be applicable. By utilizing these methods, the microscopic load state of failure was identified and the point of origin was located.

Each compression after impact specimen was analyzed with a particular emphasis on identifying the point of failure initiation. Figure 76 illustrates the extent of delamination created by impact and after failure from axial compression testing. Failure of the panel occurred across the full specimen width, encompassing approximately 1.0- to 1.5-in wide band. Delaminations within the specimen interior were exposed for examination by sectioning through the damage area indicated by TTU inspection. To help in the examination of a large number of areas, detailed optical microscopy fracture surface inspections were performed at magnifications ranging from 200X to 1000X. This procedure allowed approximately 20 to 30 locations/in² to be examined in detail.

Typical optical fractographs of the delamination surfaces are shown in figure 77. As illustrated, fracture morphologies ranging from pure Mode I tension to pure Mode II shear were apparent. In general, areas of Mode I separation were most prevalent adjacent to the outer specimen edges. For these areas, distinct river marks were evident as shown in fractograph A (see figure 77). Proceeding in from the edge, these river marks took on a relatively fine appearance (see fractograph B, figure 77). By varying the focal plane of examination this fine structure was found to correspond to tilting of the planes of fracture located between each river mark. The distinct river mark structure and lack of platelet formation indicates this area to be closer to Mode I

Impact location



Before Compression Testing



After Compression Testing

Panel before and after compression testing. Dark areas indicate internal damage.

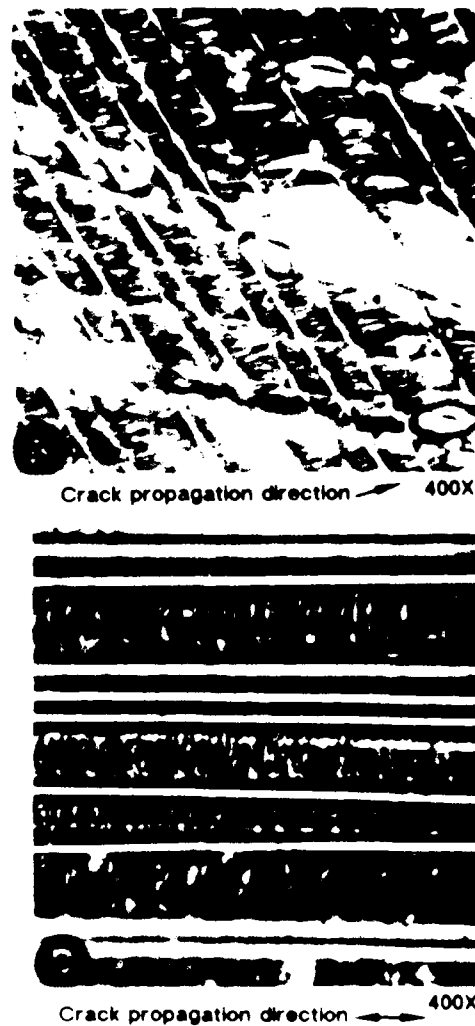
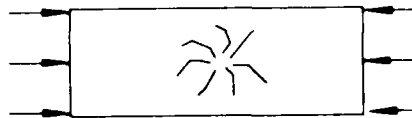
Figure 76. Through-Transmission Ultrasonic Scan of Compression After Impact

6-B70236R1-76



Optical photomicrographs

Fracture type	Interlaminar/translaminar
Ply layup	[0, 45, 90] 16S
Test type • Test conditions	Compression after impact 70°F dry
Material	Hercules 3501-6/177°C cure AS4 fibers



Crack propagation directions are illustrated under each fractograph.

Figure 77. Typical Optical Fractographs Taken From Excised Delamination Surfaces of Compression After Impact Specimen

6-B70236R1-077

tension than Mode II shear. For both of these types of morphology (fractographs A and B) the direction of crack propagation was assigned in the direction of river mark coalescence.

Closer to the specimen center a more shear dominated fracture morphology was observed. As indicated in fractographs C and D (see figure 77), a variety of scalloped features were apparent. In the case of fractograph C, distinct branches and resin microflow were also observed running in a unified direction. This appearance matches that characteristic of Mode II shear failures produced for +45/-45 and 0/45 interfacial fractures. Since relatively few hackles were observed in this area, fracture was assumed to occur predominately by interlaminar shear (mechanism A).

Consistent with this mechanism, the direction of crack propagation was assigned in the direction of river mark coalescence resin microflow, as illustrated in figure 77.

At the specimen center (fractograph D, figure 77) a mixture of both scallops and hackles were observed. While this fractograph illustrates scallops oriented transverse to the specimen axis, a wide variety of orientations were actually observed. Since this central area exhibited a random mixture of both hackles and scallops, shear separation occurred through a combination of both mechanisms A and B. Consistent with this interpretation, a crack direction paralleling the path of actual propagation was assigned as shown in figure 77.

Based upon the above examinations a map of microscopic crack directions was generated. As illustrated in figure 78, crack propagation was found to run from the panel center towards the specimen free edge. This behavior suggests that fracture initiation occurred at the central impact zone. Based upon the morphology of fracture along this path, crack initiation appears to have occurred under predominantly Mode II shear loads during the impact event—whereas crack growth during compression testing involved both mixed and Mode I tension conditions. These results indicate that mapping the direction of interlaminar fracture appears feasible when a large number of areas are examined. Furthermore, the interlaminar load state at failure can be identified for even relatively complex failure situations.

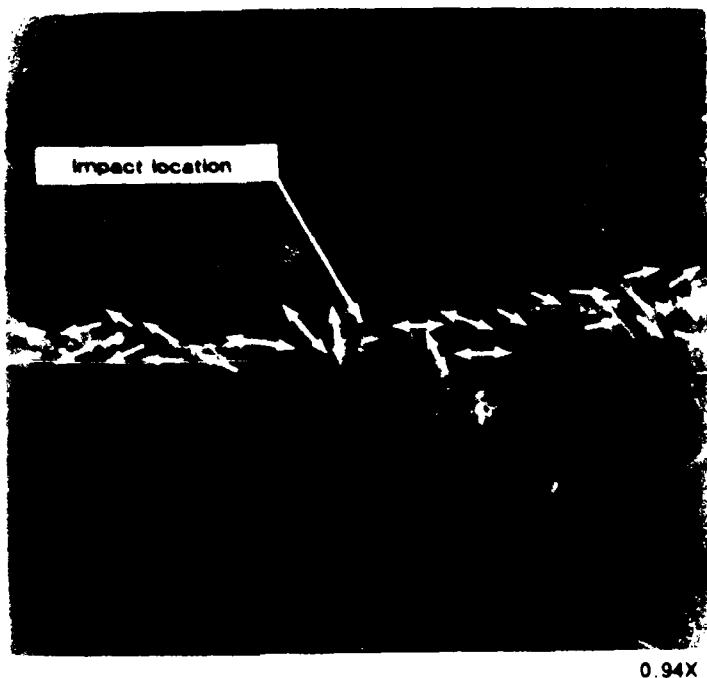


Figure 78. Typical Crack Directions Observed on Compression
After Impact Panel Using Optical Fractography

6-B70236-078

5.14 TEXAS A&M SUBCONTRACT—IN SITU SEM

5.14.1 Overview/Approach

During this program, a subcontract was provided to Dr. Walter Bradley of Texas A&M University. The intent of the investigation was to further understand the fracture mechanisms involved during the delamination process, with primary emphasis aimed toward the determination of the significance of hackles. In particular, the question of whether the hackle orientation could be used to infer crack growth direction (as sometimes had been claimed). The following paragraphs are an edited executive summary of the final report submitted by Dr. W. L. Bradley and Mr. C. R. Corleto of Texas A&M. Final comments are provided by Boeing.

The approach used in this study was to observe the delamination fracture process of a graphite/epoxy composite material, during real time and postmortem observations in the scanning electron microscope. Then a comparison of these observations was done to give a better insight into the correct interpretation of the significance of fractured surface features..

5.14.2 Experimental Procedures

Split laminate specimens (3.81-cm long, 0.508-cm wide, and 0.114-cm thick) and end-notch flexure specimens (3.048-cm long, 0.508-cm wide, and 0.114-cm thick) were cut from an 8 ply unidirectional precracked panel of Hercules AS4/3501-6 graphite/epoxy composite. Specimen dimensions were determined by the space allowed on the tensile stage of the SEM and by using stable crack growth criteria for the case of the end-notch flexure specimens (Carlson and Gillespie, 1985). All the specimens were polished with 0.3 grit aluminum powder and cleaned ultrasonically.

Mode I and Mode II observations of the delamination fracture process were determined using real time observations in the SEM. Mode I delamination was achieved by pushing a wedge into the precracked portion of the split laminate specimens, using the tensile stage of the SEM. The wedge was sufficiently blunt to ensure that it remained well away from the crack tip, giving essentially pure Mode I loading (see figure 79). Mode II delamination was achieved by means of a specially designed three-point bend fixture installed to the tensile stage of the SEM (see figure 80). To confirm that these real

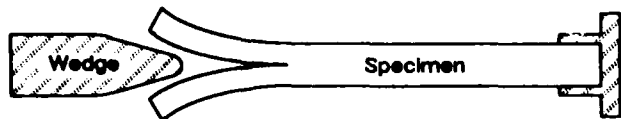


Figure 79. Mode I Delamination (Wedge)

6-B70236R1-079

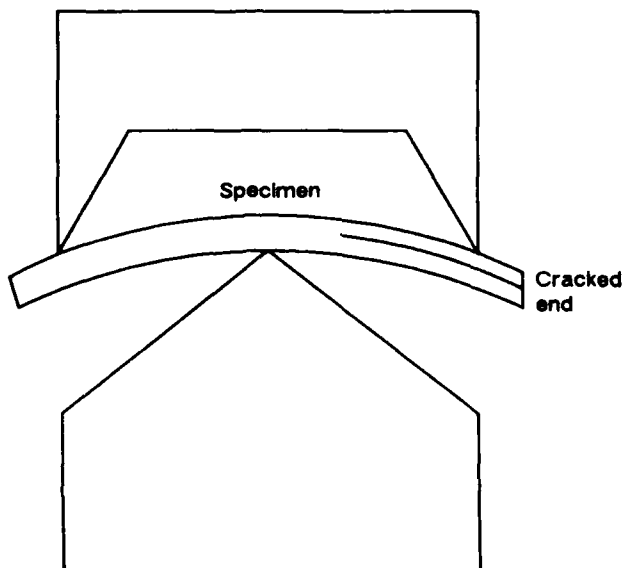


Figure 80. Mode II Delamination (Cracked End)

6-B70236R1-080

time observations of both Mode I and Mode II delamination were representative of the bulk delamination behavior, postmortem studies of the fractured surfaces were performed.

The studies were performed with a JEOL JSM 35 SEM. All surfaces observed were coated with a 200-angstrom thick gold/palladium film to minimize charging effects associated with the nonconductive nature of the epoxy matrix of the composite. The experimental results were recorded on both video tape and on standard Tri-X film.

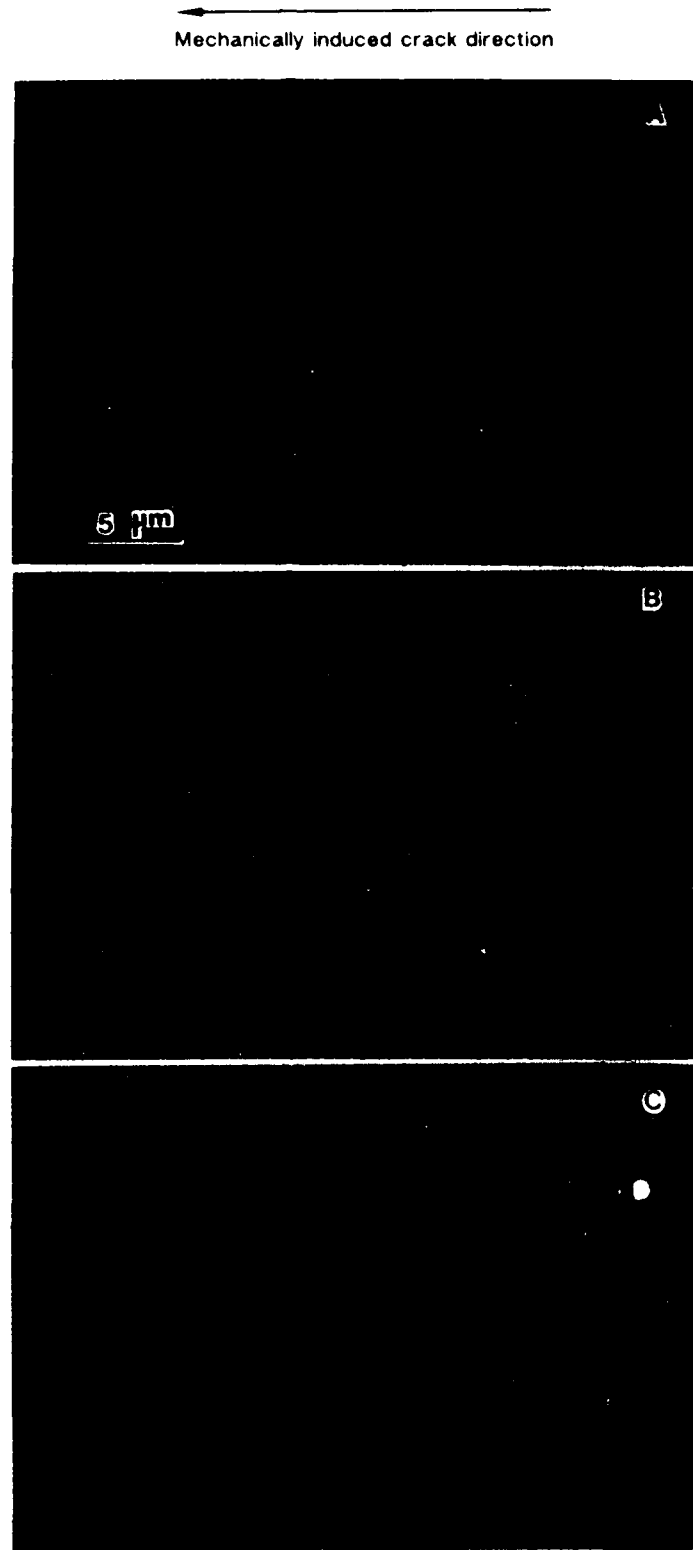
5.14.3 Results

- **In situ Fractography**—The micrographs in figure 81 are realtime observations of Mode I delamination of AS4/3501-6 graphite/epoxy. The damage zone occurs ahead of the crack tip. This damage zone is characterized by extensive microcracking of the resin extending at least 90 μm ahead of the macroscopic crack tip. Crack propagation occurred via microcrack coalescence and interfacial debonding. Microcrack coalescence was mainly observed in resin rich areas, although occasionally the crack tended to quickly jump to the fiber-matrix interface even in these regions.

The damage zone ahead of the macroscopic crack of AS4/3501-6 graphite/epoxy under real time Mode II delamination observations revealed that the damage zone extended much further ahead of the crack tip (at least 200 μm) than the damage zone observed for pure Mode I loading.

Three stages in the macroscopic crack extension and the concurrent hackle formation can be seen in figure 82. First, microcracks start to form at approximately 45-degrees to the plane of the plies (figure 82a). Second, macroscopic crack extension occurs as the microcracks begin to coalesce forming the hackles (figure 82b), increasing the fractured surface area (figure 82c). Third, matrix separation occurs.

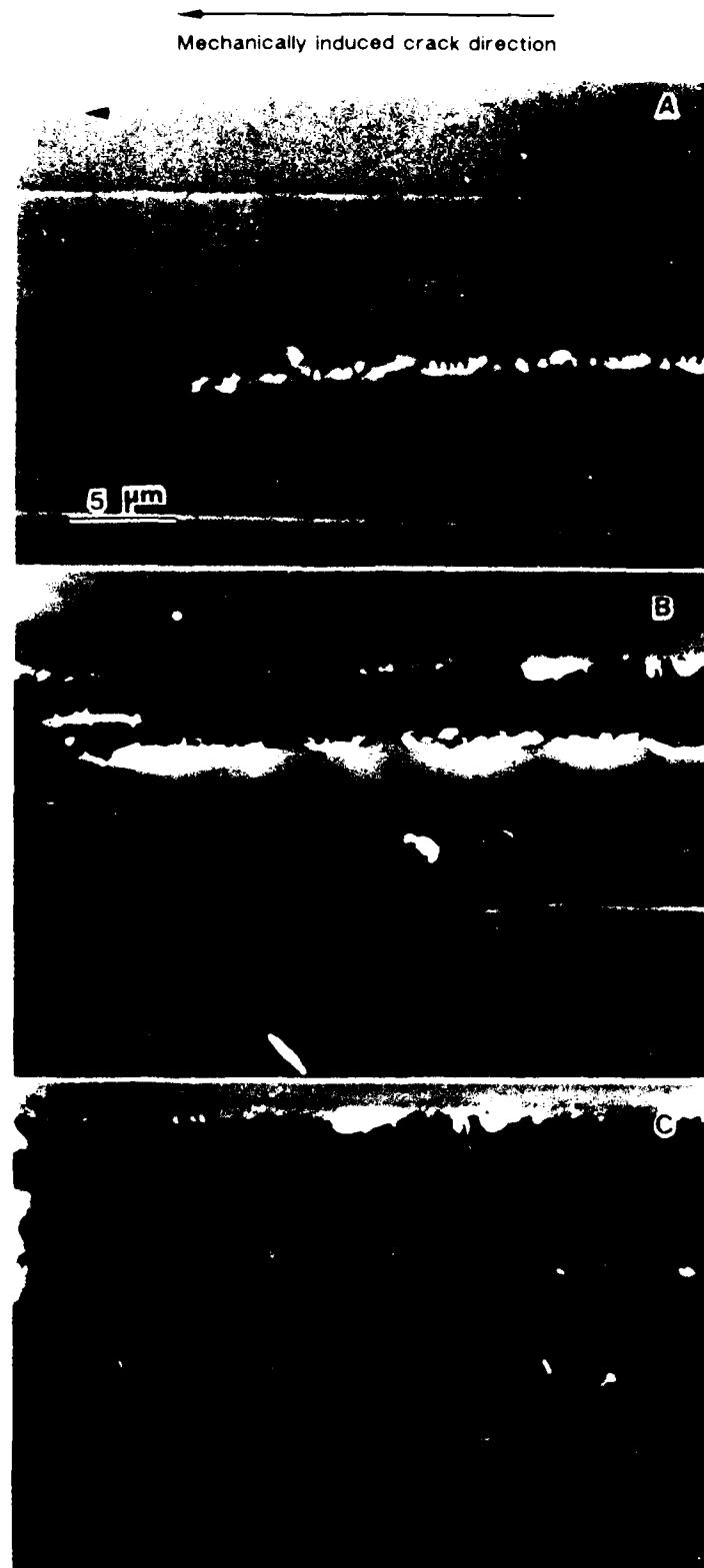
Figure 83 shows the fully formed hackles once coalescence of the microcracks has occurred resulting in crack advance past this point. During this process, some resin deformation must have accompanied the formation of hackles as the gap between adjacent hackles results from rotation at the base when the microcrack



Damage zone ahead of the crack tip of AS4/3501-6 graphite-epoxy.
Microcracking is the major damage observed. 3000X.

Figure 81. Mode I In-Situ Delamination (Damage Zone)

6-B70236R2-081



Three stages in crack propagation. (A) Microcracking early stage in hackle formation. (B) microcrack coalescence. (C) increase in fractured surface area. 3000X.

Figure 82. Mode II In-Situ Delamination (Three Stages)

6-B70236R2-082

SEARCHED INDEXED SERIALIZED FILED



SEARCHED INDEXED SERIALIZED FILED
APR 11 1968

SEARCHED INDEXED SERIALIZED FILED APR 11 1968

APR 11 1968 783

coalescence occurs. Note how the final hackle orientation (figure 83d) is steeper than the 45-degree angle of orientation of the initial microcracks from which the hackles form (figure 82a). No clear indication of crack growth direction is given by the hackle orientation of the fractured surfaces. Arrows on upper left corner of all figures indicate crack growth direction, that is from right to left.

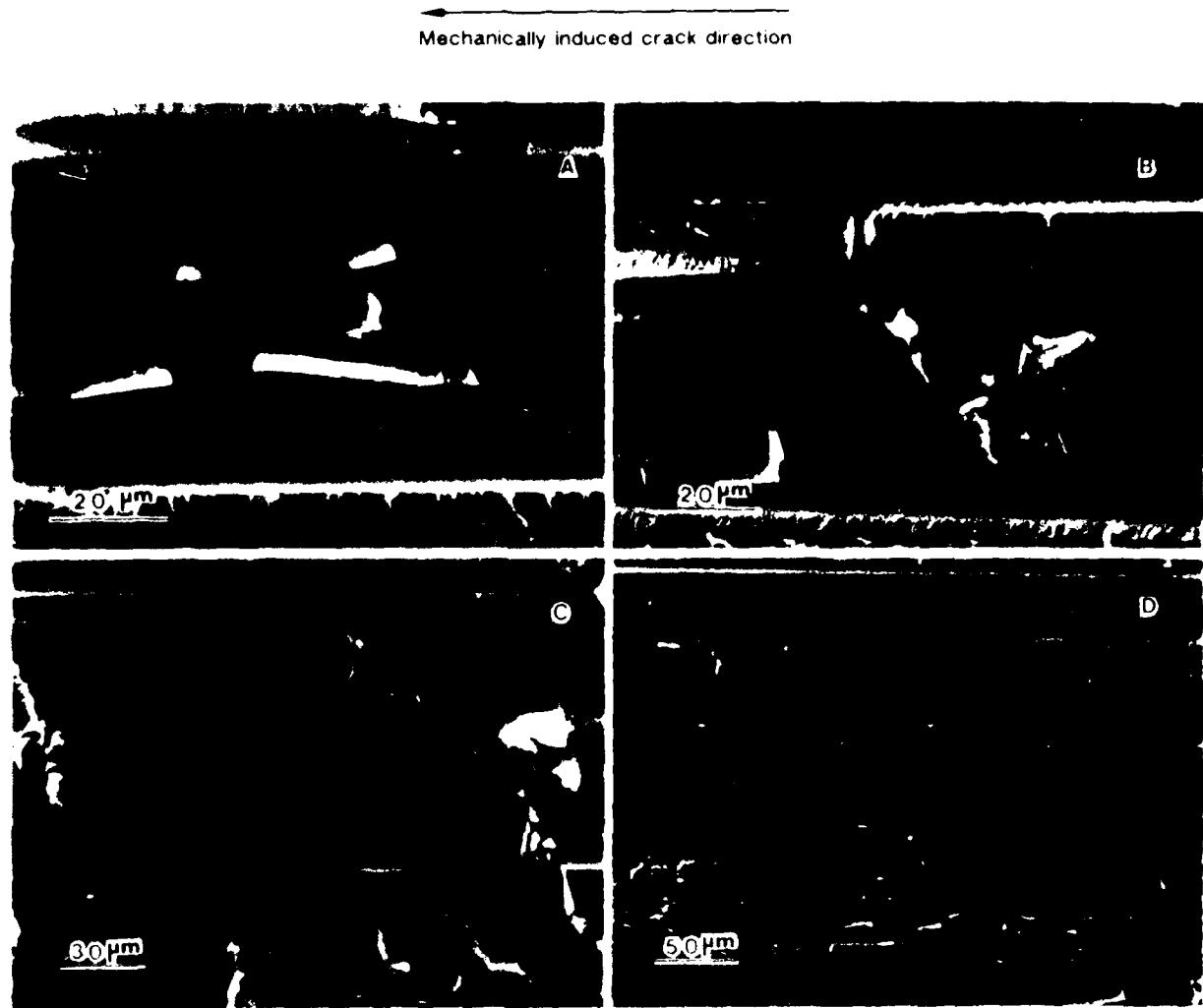
- **Postmortem Fractography**—Figure 84 represents Mode I delamination postmortem fractography of the fractured surface. Figure 85 shows the postmortem fractography of Mode II delamination. (Note that the general fracture morphology is essentially identical to that identified during tasks 2A and 3A of this program).

In order to assure that microcracking observed was not a result of microcracking in the gold/palladium coating, a specimen was coated after it was loaded under Mode I delamination, and then examined. Results indicated that the resin intrinsically undergoes microcracking during loading.

- **Discussion**—As shown previously, the damage zone ahead of the crack tip for Mode II delamination extended at least twice as long as the damage zone for Mode I loading. This is possibly because for Mode II, the resin rich region between plies behaves like a soft material between rigid platens with all of the strain being localized in this region.

The extensive microcracking observed in the damage zone for both Mode I and Mode II delamination indicated that a considerable amount of energy was being dissipated in this process. Good agreement has been found between the angle at which microcracking forms (in situ observations) relative to the macroscopic load state, namely, a shallow or nonexistent angle for Mode I and a steep angle (sometimes beyond 45-degrees) for Mode II.

Though not specifically studied in the project, the authors have found in other studies that the incidence of hackle formation is much influenced by resin ductility, with more brittle resins giving the most distinct hackle formation during the fracture process. These are to be expected since hackles are the end product of coalesced microcracks, and ductile resins do not tend to microcrack.

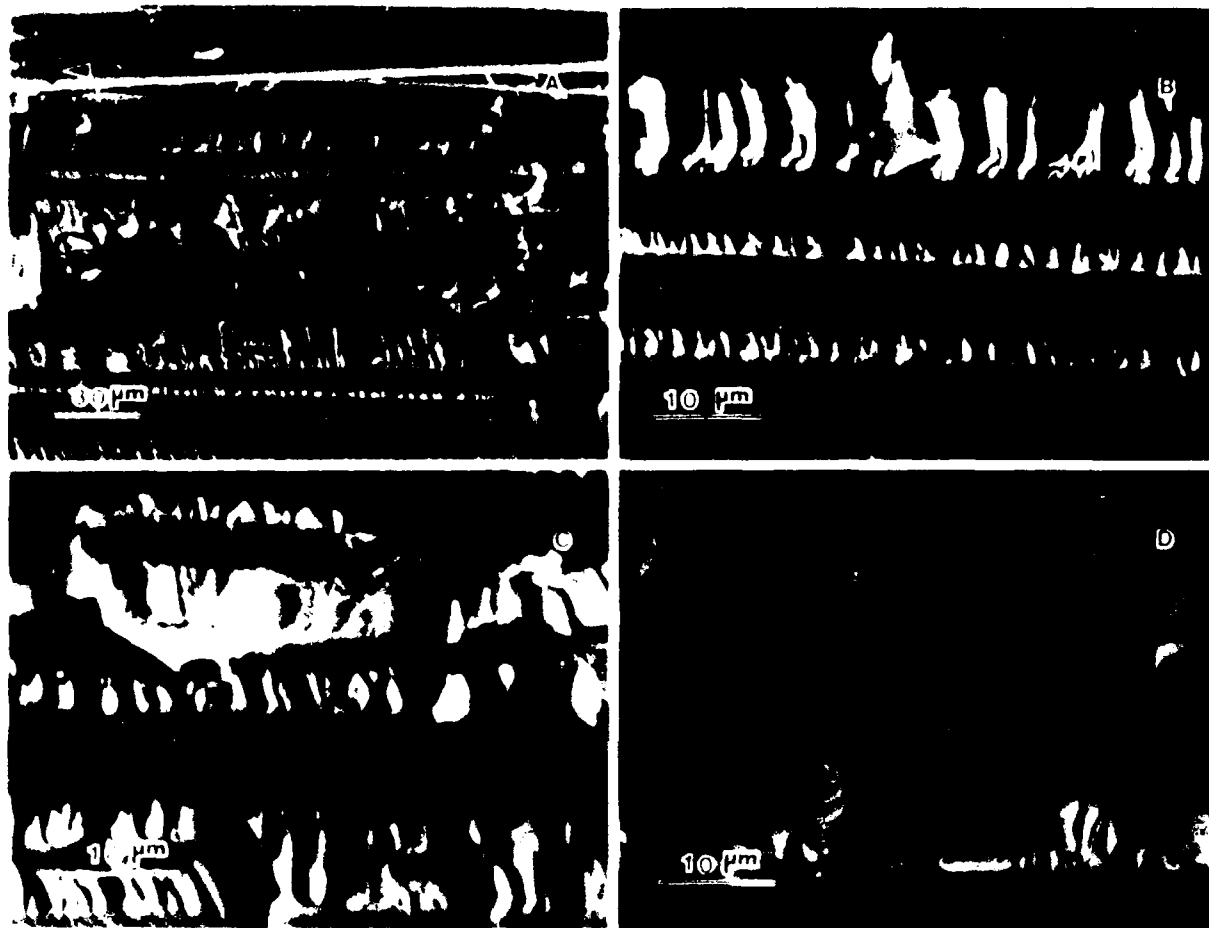


Fractured surface from middle of specimen. (A) 1000X. (B) 1000X, shallow hackle formation. (C) 500X. (D) 300X

Figure 84. Interlaminar Mode I Postmortem Fractography

6-B70236R1-084

Mechanically Induced crack direction



Extensive hackle formation. Micrographs taken from the middle of specimen. (A) 500X. (B) 2000X. (C) 2000X. (D) 2000X

Figure 85. Interlaminar Mode II Postmortem Fractography (Hackle Formation)

6-B70236R2-085

- **Comments (Boeing)**—This work has been found to directly corroborate the efforts by Boeing within task 2A and 3A of this program for studies regarding interlaminar DCB (Mode I) and ENF (Mode II) specimens. It should be again noted that these investigations by Texas A&M were performed on unidirectional tape (zero ply orientation relative to crack growth), in which hackles were also found by Boeing to be created under both mechanisms A and B. Research by Boeing in this program indicated that certain ply orientations (relative to crack growth) exhibited a tendency to fracture by mechanism A, in which the hackles separated primarily on one side of the crack. For these orientations (0/90, +45/-45, and 0/45) the hackles tilted in the direction of crack propagation. See the interim report from this program for details (AFWAL-TR-86-4033).

It is clear at this point that further studies are required to understand the factors relative to hackle separation by mechanism A or B. Investigations are planned for the Air Force sponsored program F33615-86-C-5071, in which efforts will attempt to more closely evaluate the Mode II interlaminar fracture mechanism, so that important features such as river marks, resin microflow, and hackle tilt can be used with confidence by an investigator to determine crack propagation directions.

6.0. TASK 5: VERIFICATION AND DEMONSTRATION ON FAILED COMPONENTS

The objective of task 5 was to demonstrate and evaluate the failure analysis logic sequences (FALNs), the various analytical techniques, and the overall capability to adequately define the cause of failure. During the performance of this task, the cause of failure of three composite structural components was successfully determined. The FALNs and the various analytical techniques developed within this program were used to identify the sequence of failure, the origin locations, the loading conditions, and the direction of crack propagation for the following structural components:

- V-22 Osprey full scale wing test box.
- NASA HiMAT test wing.
- I-beam.

Figures 86 through 90 present the resulting FALNs after application and final revision. Only slight changes were made to the original major FALN and each of the sub-FALNs.

The successful results obtained during the postfailure analyses investigations suggested that the technology has come a long way since it was started in the late 1970's. Through efforts within this program as well as other research programs from the scientific community, it is evident that many of the analytical instruments and methods are approaching the capability currently available for metal failure analysis. The primary deficiency evident through actual application of the various techniques on failed components, such as those evaluated in task 5, is that many of the interpretive methods are still in the infancy stages. Although the capability to understand the microscopic fracture mechanisms and the characteristic microscopic fracture features is rapidly evolving from programs such as this, future efforts need to be aimed at the lower magnification fracture analysis capability such as macroscopic analysis.

The results from each of the three postfailure analysis investigations are presented below. For each component, the results are presented in the order that the investigation progressed, with the analytical techniques and interpretations provided. The JVX full scale wing test box comprised a major investigation, with extensive, detailed, and time consuming analysis. This involved a large amount of effort in each of the analytical disciplinary areas including expensive stress analysis and replicate component testing. At the other end of the spectrum, the I-beam analysis was relatively quick and involved a much lower cost. This was primarily due to the much

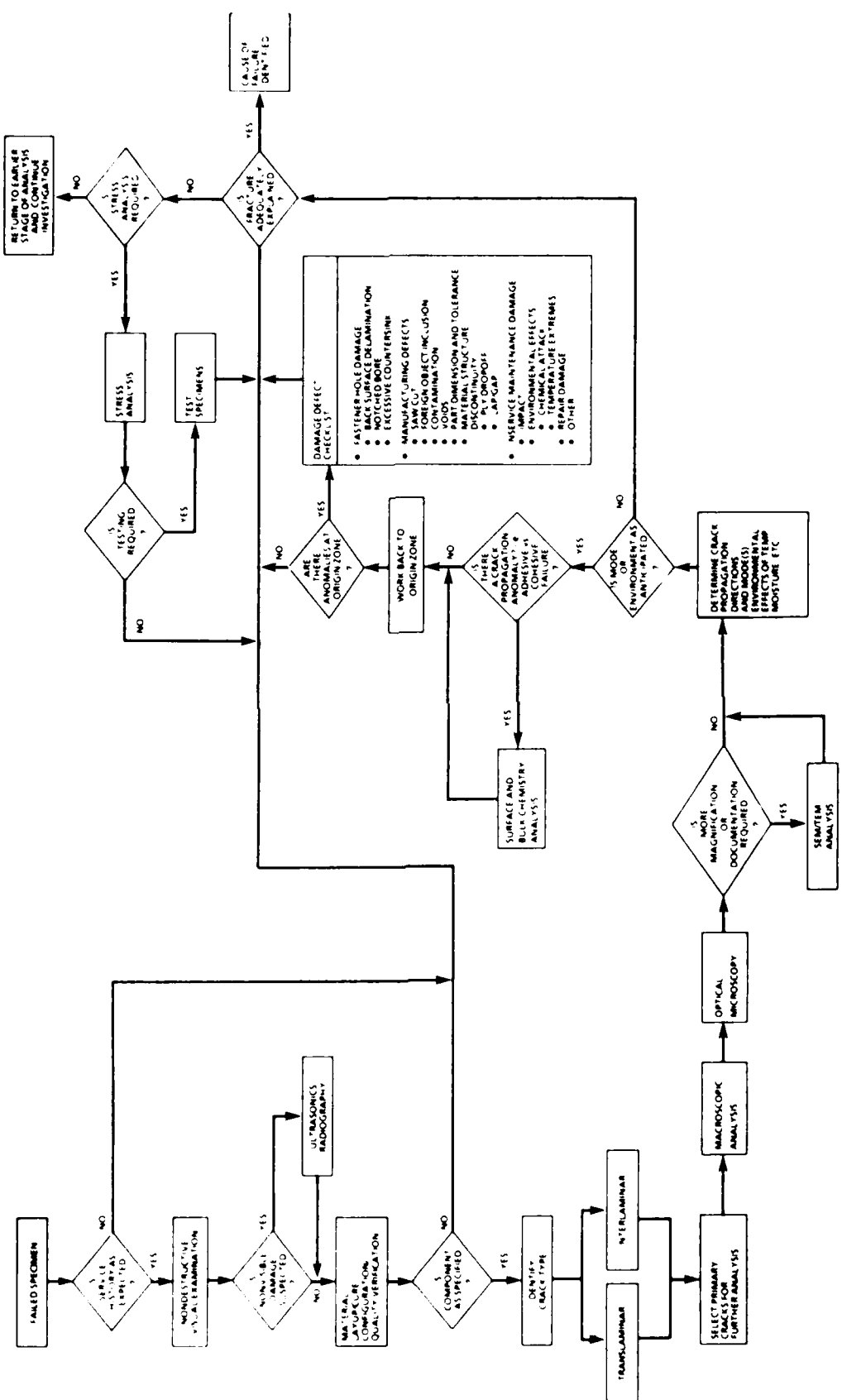


Figure 86. Detailed Failure Analysis Logic Network (FALN)

6-870236B1-086

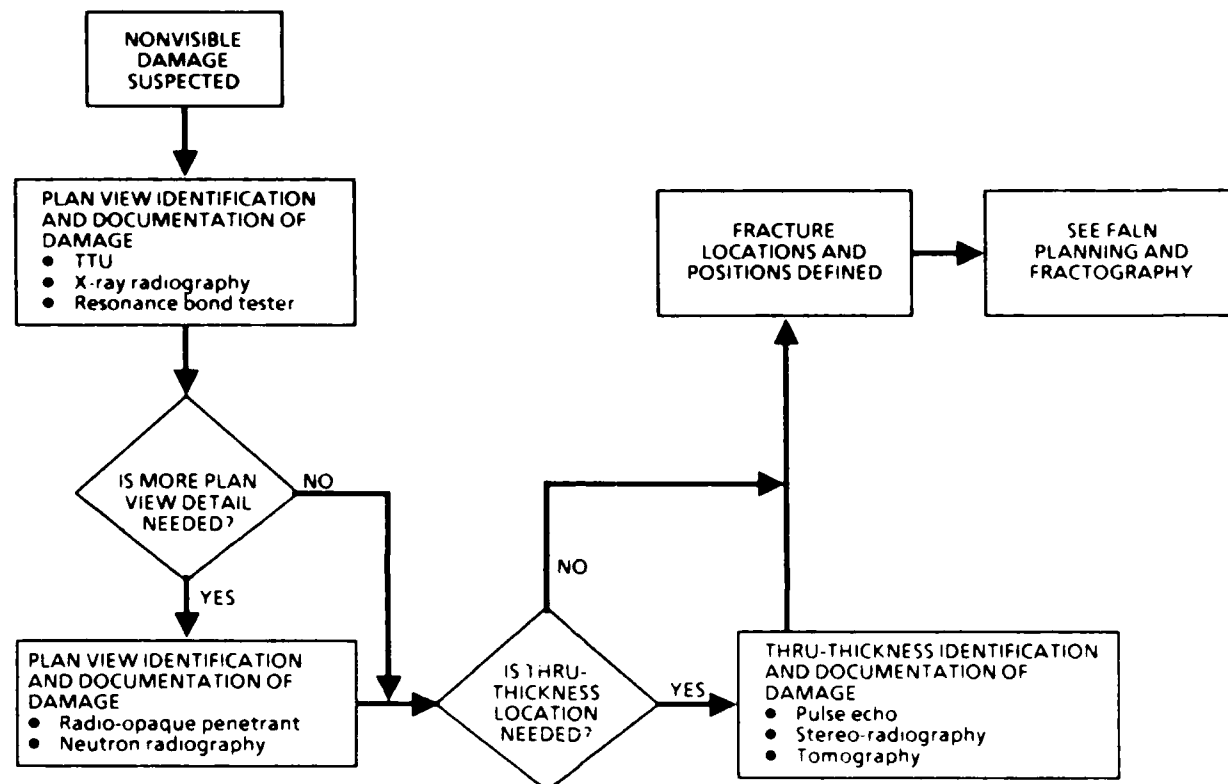


Figure 87. Nondestructive Evaluation Sub-FALN

6-B70236-087

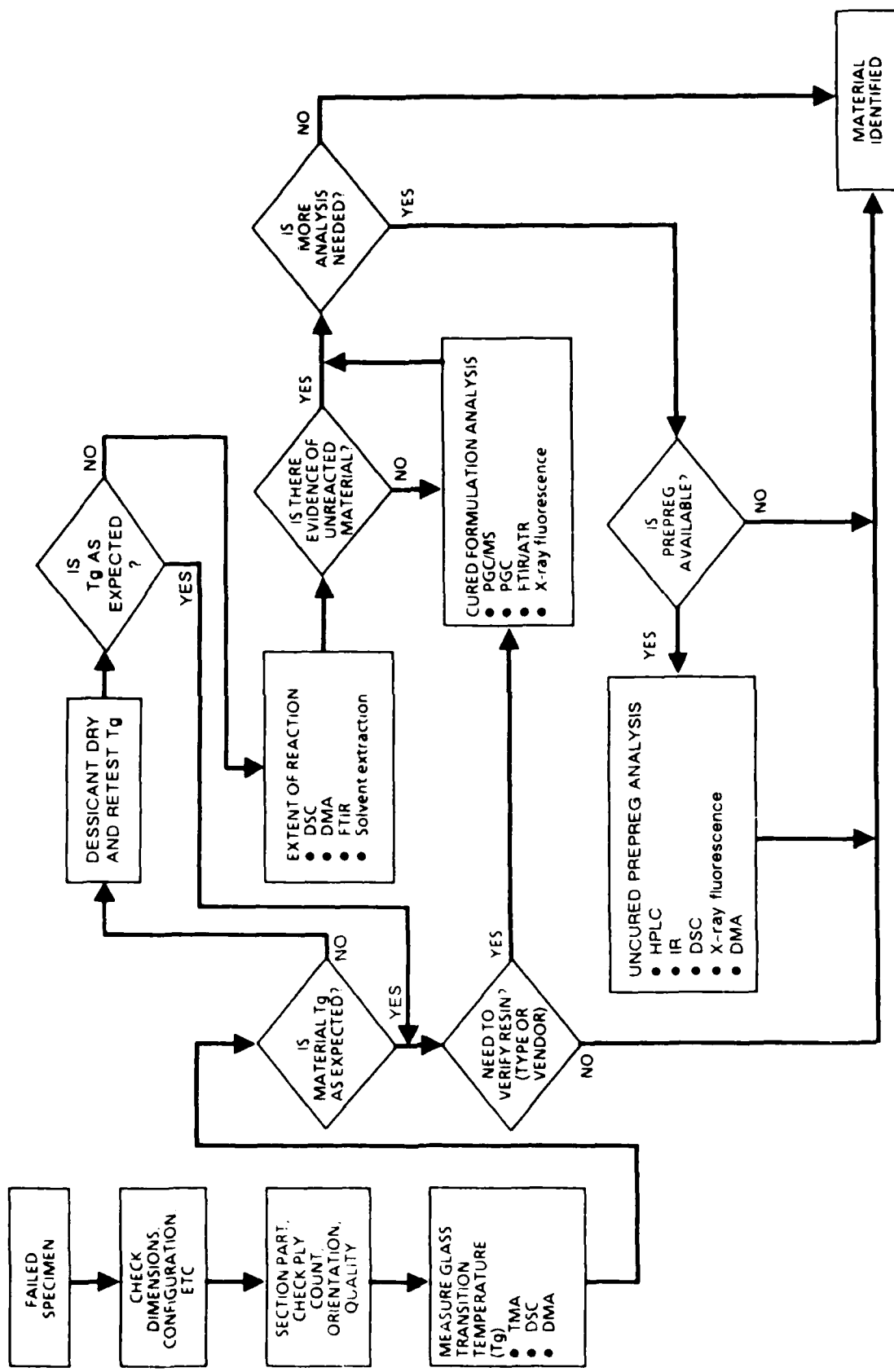


Figure 88. Material Verification Technique Sub-FALN

6-B70236-088

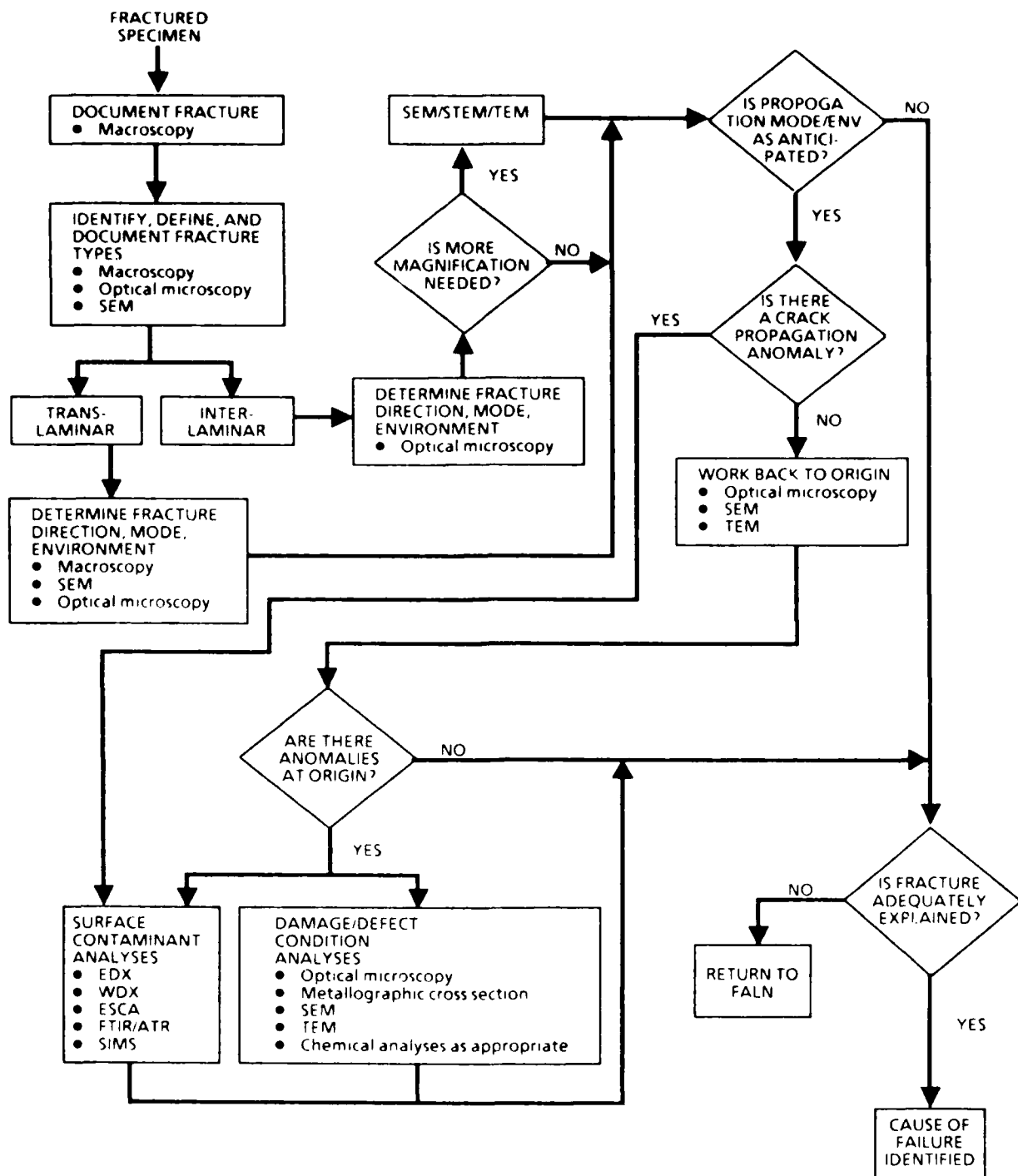
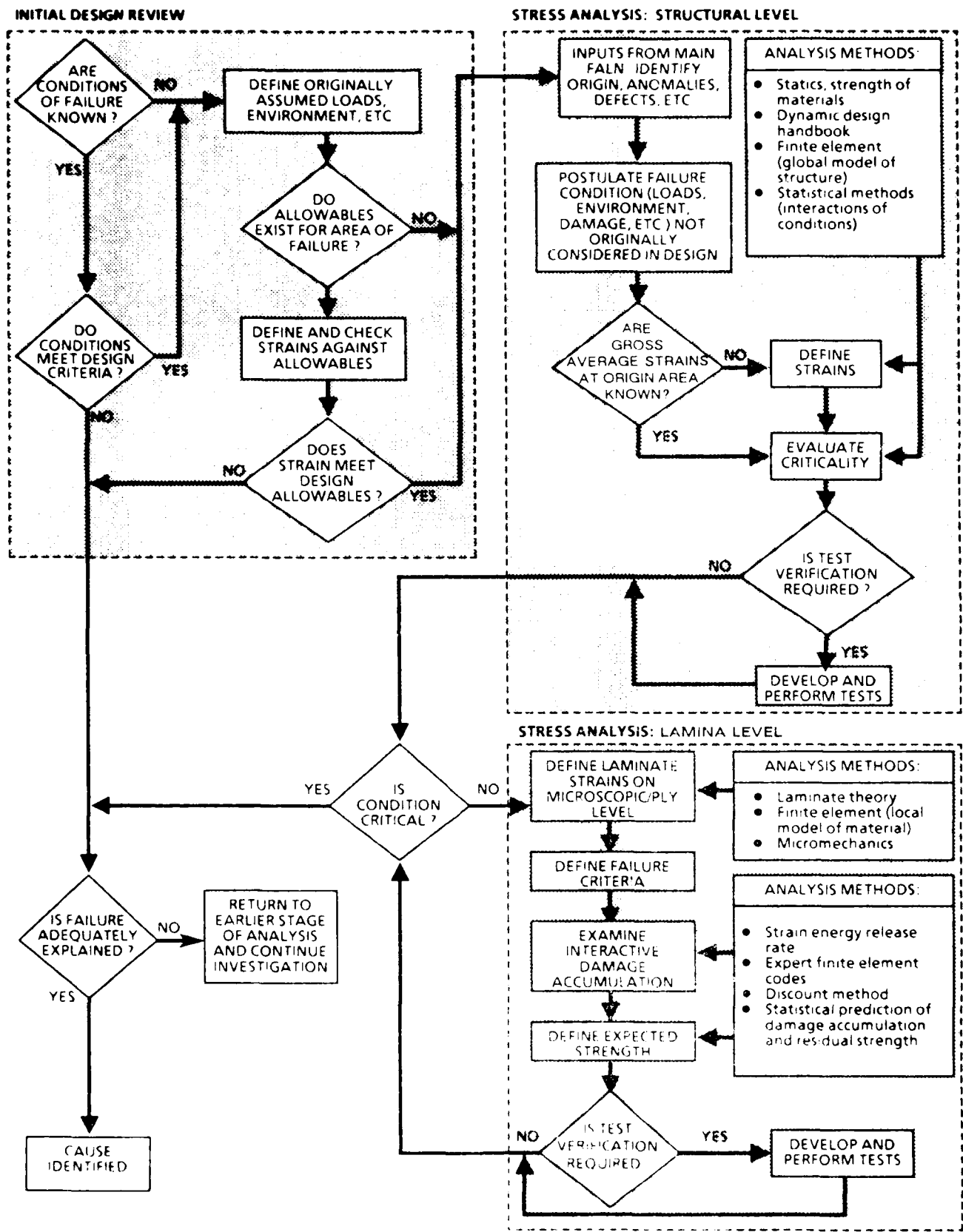


Figure 89. Fractography Diagnostic Technique Sub-FALN

6-B70236-089



Volume 17 Number 4 August 1993

6-B70236-090

smaller scale than the JVX test box; however, a majority of the investigation involved macroscopic and visual inspections of the fracture surfaces and provides some insight into the great value of lower magnification analysis techniques.

6.1 JVX V-22 OSPREY FULL SCALE WING TEST BOX

Analysis of the wing box was initiated after premature fracture occurred during testing of the structure. Figure 91 illustrates the central portion of the structure immediately following fracture, with the cracking occurring in the center bay region. Discussions with the test and design engineers indicated that the loading conditions were applied to simulate upward and aft bending of the outboard ends of the box, so as to create a maximum compressive stress at the upper skin surface. The construction was found to be a stringer stiffened skin with front and rear spars, and with ribs fabricated entirely from graphite/epoxy tape. At that time, the manufacturing data regarding the specific materials, processes, design as well as the intended operational envelope were collected.

6.1.1 Nondestructive Evaluation

Initial visual inspections of the damage region were carried out to identify the areas of visible fracture or deformation. As shown in figure 92, the upper skin surface exhibited a branching translaminar crack across the entire surface (severing all five stringers) and compression type translaminar fracture morphology for both the skin and stringers (as indicated by the flat fracture appearance). This macroscopic translaminar branching most likely indicated the gross overall fracture direction, such that the cracking progressed across the skin from the rear spar region in a chordwise direction toward the front spar. The translaminar cracking intersected the trailing edge of the skin at a radius for a runout of an overhanging tab. Extensive delamination was evident on each side of the translaminar cracking, often wedged open from mating fracture surface overrun during compression loading. Figure 93 presents the underside of the upper skin surface, at the trailing edge tab region, illustrating the type and extend of damage.

The front and rear spars (see figure 94) were also cracked, each exhibiting vertical translaminar fractures that appeared to be a continuation of the upper skin fracture. The spar webs were delaminated around the translaminar cracks, with extensive buckling indicative of a compressive load at failure.

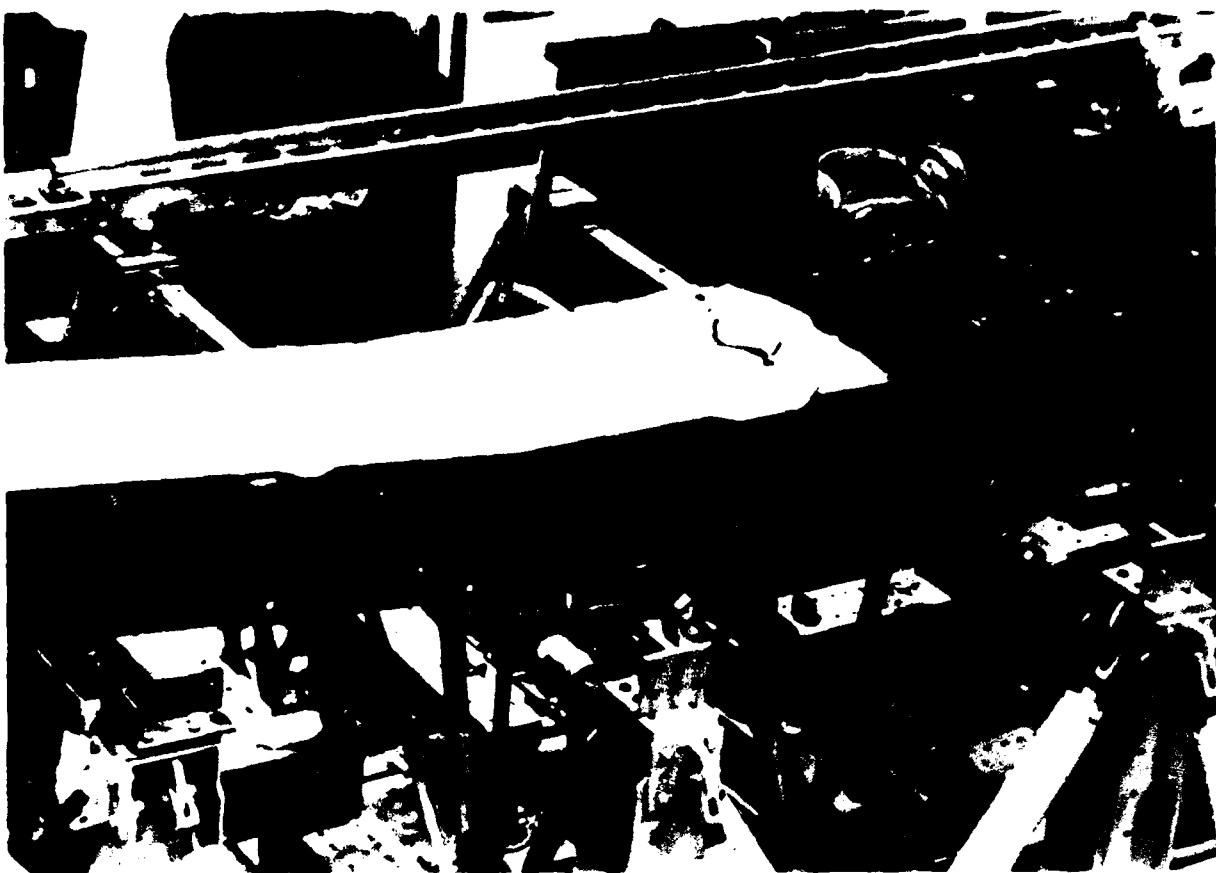


Figure 91. Central Portion of JVX V-22 Central Wing Test Box

6-B70236-091

6-B70236-092

Figure 92. JVX Wing Test Box Upper Skin Surface

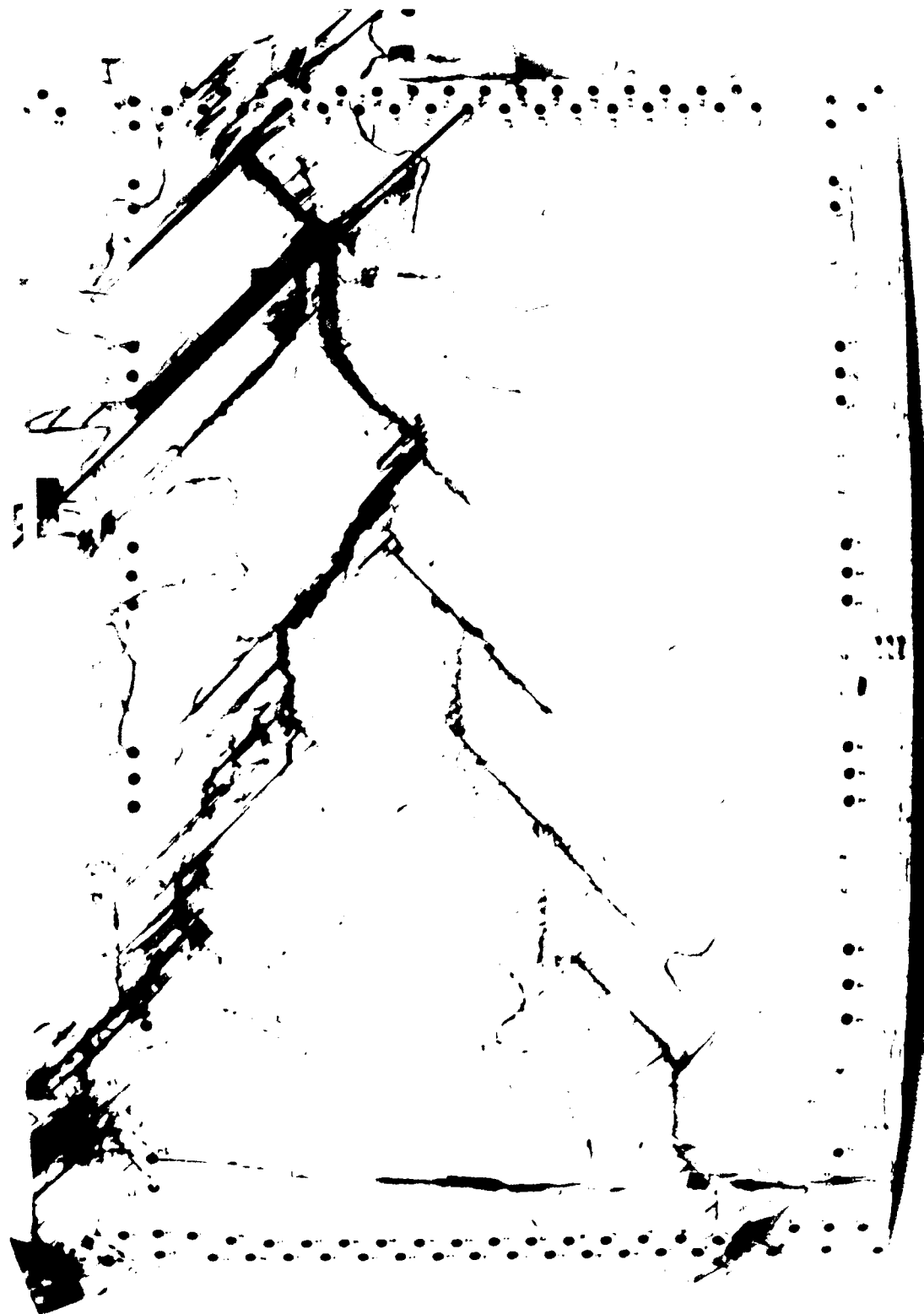
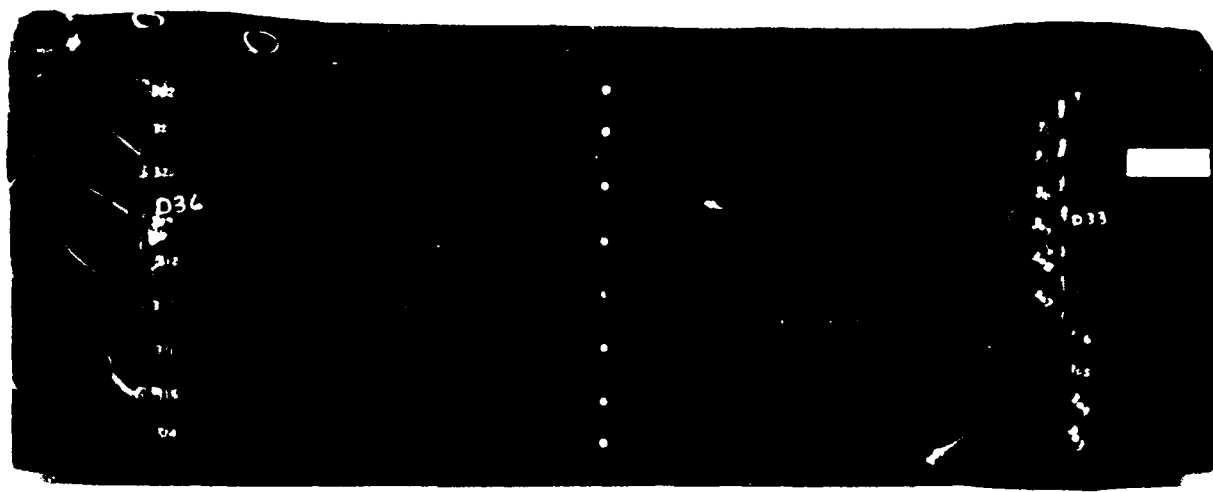


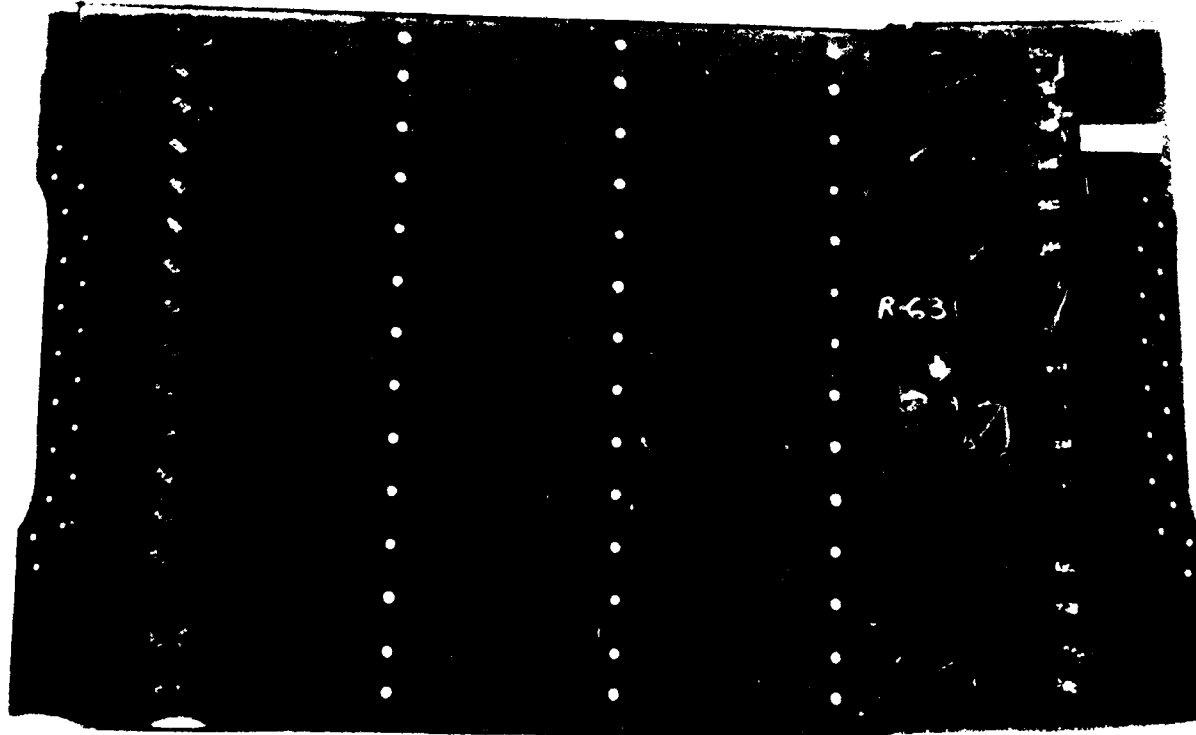


Figure 93. JVX Wing Test Box Inner Side of Upper Skin Surface

6-B70236R1-093



Front Spar



Rear Spar

Figure 94. JVX Wing Test Box Front and Rear Spars

6-B70236-094

The lower skin surface, shown in figure 95, was damaged in a similar manner to the upper skin, although to a lesser extent. The skin buckling also indicated a compressive loading. Because the stress prior to fracture was supposed to be tensile, the neutral axis between tension and compression must have shifted to below the lower skin surface during the failure process. As a result of these visual observations, it appeared that damage in the upper skin and spars occurred prior to cracking in the lower skin.

Nondestructive evaluation (NDE) was then performed to determine the extent of nonvisible damage. While still intact as a complete structure, the entire wing box was subjected to hand held pulse echo inspection. This allowed determination of the extent of delamination surrounding the translaminar fracture as well as checking the remaining structure for any other damage that may have either contributed to, or occurred during, the failure. The outline of the delaminations surrounding the translaminar fractures as indicated by pulse echo are visible in figures 91 through 95.

Following the visual inspections and photo documentation, the damaged central wing box portion was cut out and the major components (skins, ribs, spars, etc.) were separated from one another. During component breakdown, each fastener was carefully removed and examined for proper fabrication and installation. No damage or incorrect manufacturing anomalies were identified related to fastening. Following removal of the skins, spars, and ribs in the failure region, each of these components were subjected to C-scan TTU inspections to more accurately appraise the extent of delaminations. As shown in figure 96, the upper skin surface damage at the trailing edge tab radius was easily defined. Suspecting damage such as small translaminar cracking at the radius on the other side of the tab, radio opaque penetrant X-ray inspection was performed in this region, however no damage was present.

6.1.2 Materials Characterization

Materials characterization involved performance of the following tests on all components (listed with a brief summary of the results):

- Degree of cure (T_g) using TMA flexural method; $T_g = 191^{\circ}\text{C}$ to 201°C (indicating a proper cure at 180°C specification minimum).
- Resin content using density gradient column method; acceptable 33.8% to 34.9% by weight (35% prepreg).

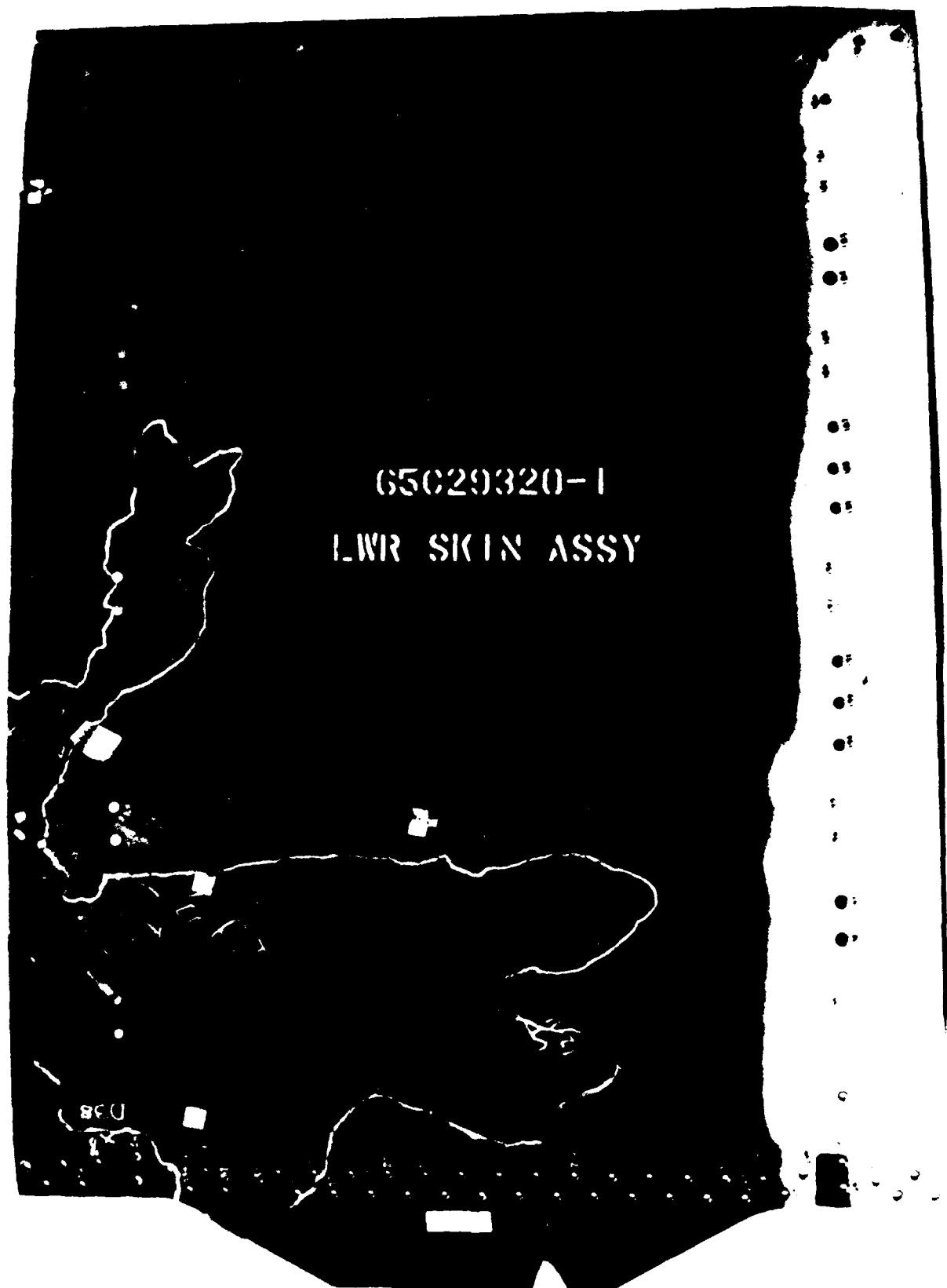


Figure 95. JVX Wing Test Box Lower Skin Surface

6-B70236-095

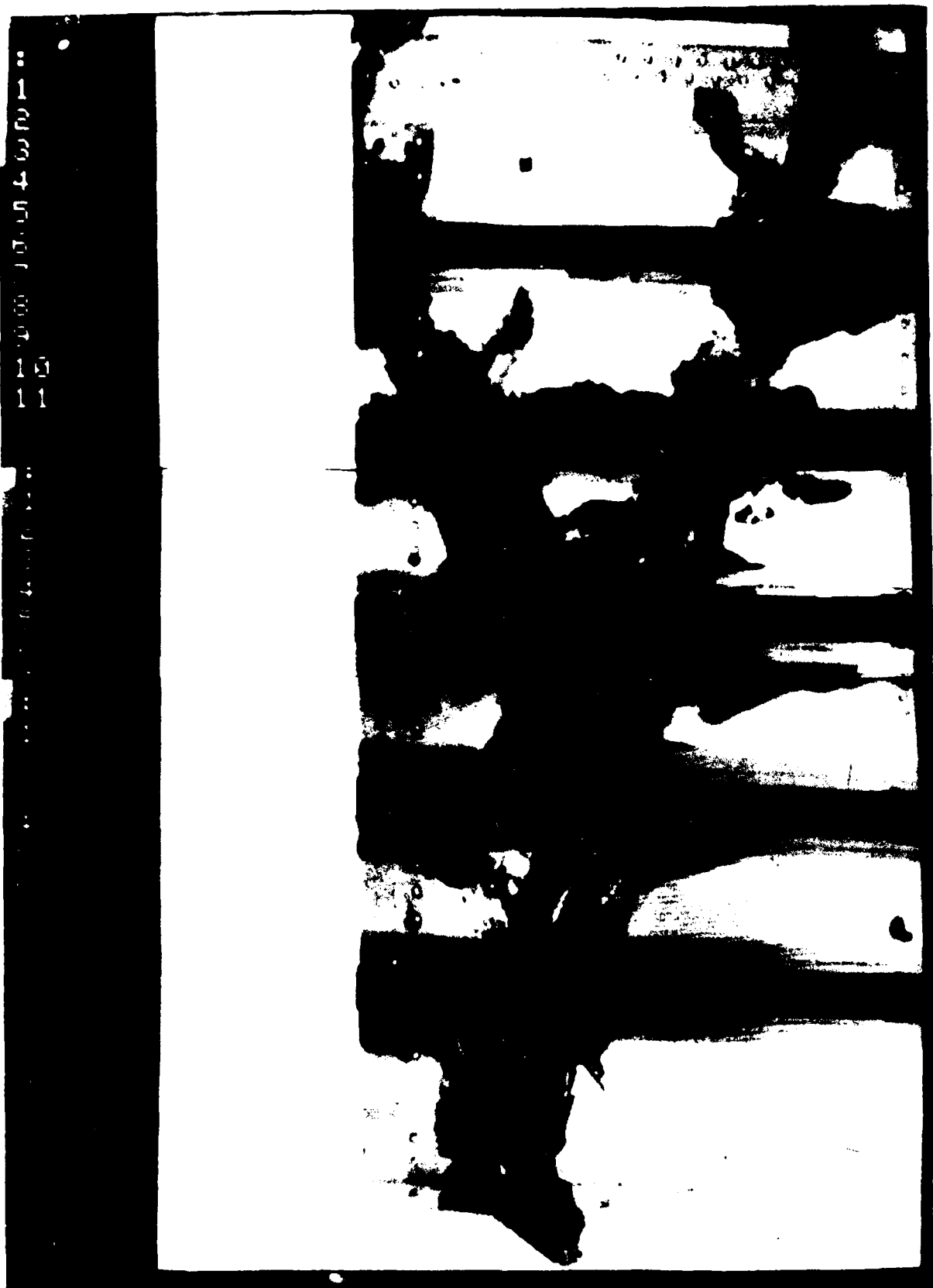


Figure 96 Ultrasonic C-Scan of Upper Skin Surface

F.B.I. 236-296

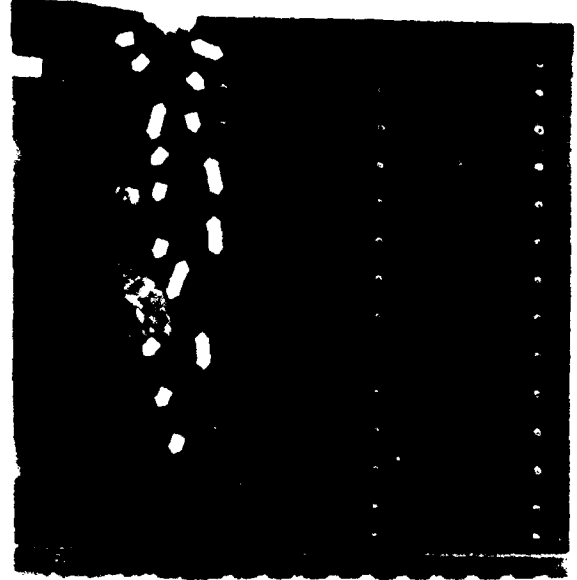
- Microstructure and porosity using optical microscopy; no resin starvation or porosity, no fiber waviness.
- Ply count and orientation using optical microscopy; all components in good condition except slight ply discrepancies in upper skin near trailing edge tab radius.
- Dimensional conformance to engineering drawing; upper skin tab radius = 1.5-in (drawing callout was 3.0-in). This discrepancy was evaluated by stress analysis for stress intensity (K_t) effect.

6.1.3 Fractography

Using the outline of the delamination generated by NDE, the delaminations were opened and separated from the structure with an abrasive cutoff wheel to minimize artifacts. Detailed crack mapping of the delamination surfaces was performed by optical microscopy, with documentation of the fracture morphologies obtained with the SEM. Areas of delamination were found to be principally Mode I tension dominated, with localized Mode II shear regions. The overall crack growth directions, as well as the fracture origin regions for the upper skin surface and the rear spar are shown in figure 97. These analyses revealed cracking of the upper skin initiated by compression buckling fracture mode at the trailing edge tab radius with resultant fracture propagating toward the leading edge. Similarly, the rear spar fracture originated in a region adjacent to the upper skin surface. Crack mapping the region near the upper skin was very inconsistent, with a nearly random variation in the microscopic river marks and hackle orientation. No anomalous conditions such as porosity, resin starvation, or chemical contamination were identified in the origin regions.

Similar fractographic analyses were performed on the lower skin and front spar, with crack mapping indicating that the fractures were a direct result of the progression of the cracking from the upper skin and the rear spar.

At this point the question of the sequence of failure between the upper skin and the rear spar was asked. Experience with fracture analysis of large composite structures indicated that smaller, well defined origin regions tend to initiate at lower overall strain levels at locations such as notches or holes and therefore exhibit less damage at the origin zone. The larger, ill defined origin zones tend to be indicative of overload, or rather, high overall strain fractures (with extensive damage) and are often not



(a) Rear Spar

Origin region
(tab radius)



(b) Upper Skin Surface

Figure 97. JVX Wing Test Box Crack Mapping Results

6-B70236-097

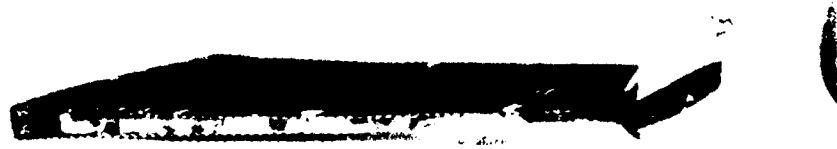
associated with notch sensitivities or defect conditions. Using this basis for a rationale, it appeared that the upper skin surface which had the small origin region, may have initiated first, at the tab radius which served as a notch.

6.1.4 Stress Analyses

While the efforts discussed above were being performed, several levels of stress analyses were also performed. These involved the initial design review to check known test conditions against the design envelope, as well as comparing test strains from the strain gauges and coarse global analyses with the overall strain allowables. The next stage was to take inputs from the materials characterization and the fractography analyses, and evaluate the strain criticality at the structural level. Through finite element analyses, an unanticipated strain level was identified at the upper skin tab radius, with the notch K_t effect at the radius contributing to the strain level. Subsequently, two small scale replicate panels were fabricated, tested and subjected to complete the failure analysis investigations. One panel was fabricated with, and one without, the tab and radii on the skin surface. Through these verification test panels, it was shown that by elimination of the tab, and thus the radii, a premature buckling mode that precipitated fracture could be prevented.

6.2 NASA HiMAT WING

Figure 98 presents the NASA HiMAT wing section in its as-received condition. This wing was built to study the behavior of aeroelastic structure design concepts over a range of flight altitudes of a highly maneuverable aircraft. The composite wing is a 44% scale model, to lower overall program cost and risk. Following numerous unmanned test flights, the outboard sweeping section of the wing was removed and subjected to simulated flight spectrum mechanical testing in the laboratory. Information supplied at this stage in the investigation regarding construction was very limited. The outboard canard was found to be fabricated from aluminum alloy and the remaining portion of the wing was fabricated from a continuous fiber reinforced laminate. Failure, denoted as a loss of structural stiffness, occurred during the mechanical testing well in excess of design ultimate load.



(a) Upper Surface

0.05X



(b) Lower Surface

0.05X

Figure 98. NASA HiMAT Test Wing in the As-Received Condition

6-B70236-098

6.2.1 Nondestructive Evaluation

Nondestructive evaluations were performed on the entire wing to determine areas of damage or defect conditions related to both testing and manufacturing. A wide variety of NDE techniques were used, primarily to evaluate each technique and to more completely determine the construction of the wing. The following techniques were applied; visual inspection, radiography, TTU (C-scan), pulse echo (B-scan), eddy current, and ultrasonic bond testing. Of these six, the key methods used to obtain data were visual inspection, TTU, and hand held pulse echo.

Although no visible primary translaminar fractures were identified, visual examinations revealed several delaminations along the inboard edge (up to 13-cm length), disbonds (up to 3-cm length) at bondlines to metal fittings, and surface delaminations (up to 13- by 8-cm). Blunt gouges were found at the center of two of the delaminations along the inboard edge of upper skin, appearing to be mechanically induced after part cure. This damage may have occurred during wing removal following flight testing. The gouges are shown in figure 99.

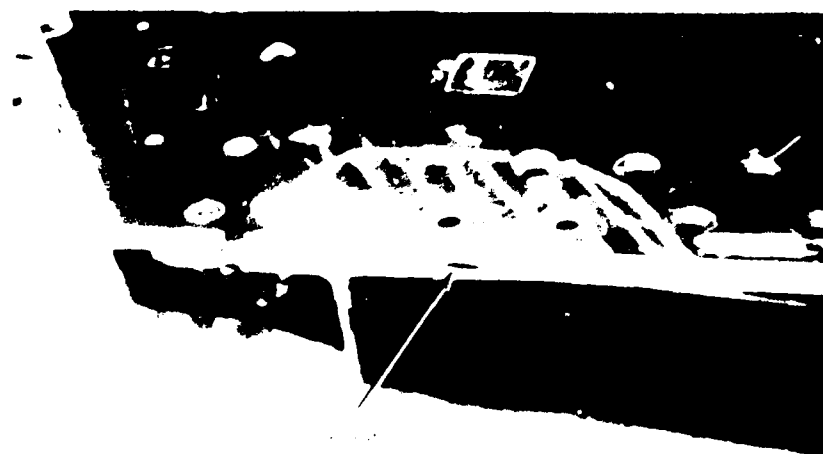
TTU analysis provided a thorough scan of the discontinuities along the upper and lower skins. The major delaminations and disbonds occurred along the inboard edge of the wing, with the exception of one donut shaped delamination at the center of the wing. Figures 100 and 101 show the TTU hardcopy printout. The areas indicated by alphabetical flagnotes were delaminations or disbonds which were crack mapped during subsequent fractographic examinations. However, the areas shown with numerical flagnotes were defects indicated by X-ray such as core to skin disbonds, core crush, and water in the core cells.

The hand held pulse echo inspections revealed the depth of each defect. The deepest delamination occurred 0.86-cm (0.34-in) below the skin surface. These depth measurements became very useful when the handmilling cuts were made to remove the delamination regions. This allowed precise cutting, reducing the extent of damage to the remaining portion of the wing, and allowed a more successful repair (because this part was to be later displayed as a historical exhibit item).



(a) Section C

0.8X



(b) Section B

0.63X

Figure 93 Upper Skin Inboard Edge Damage

6 B70236-099

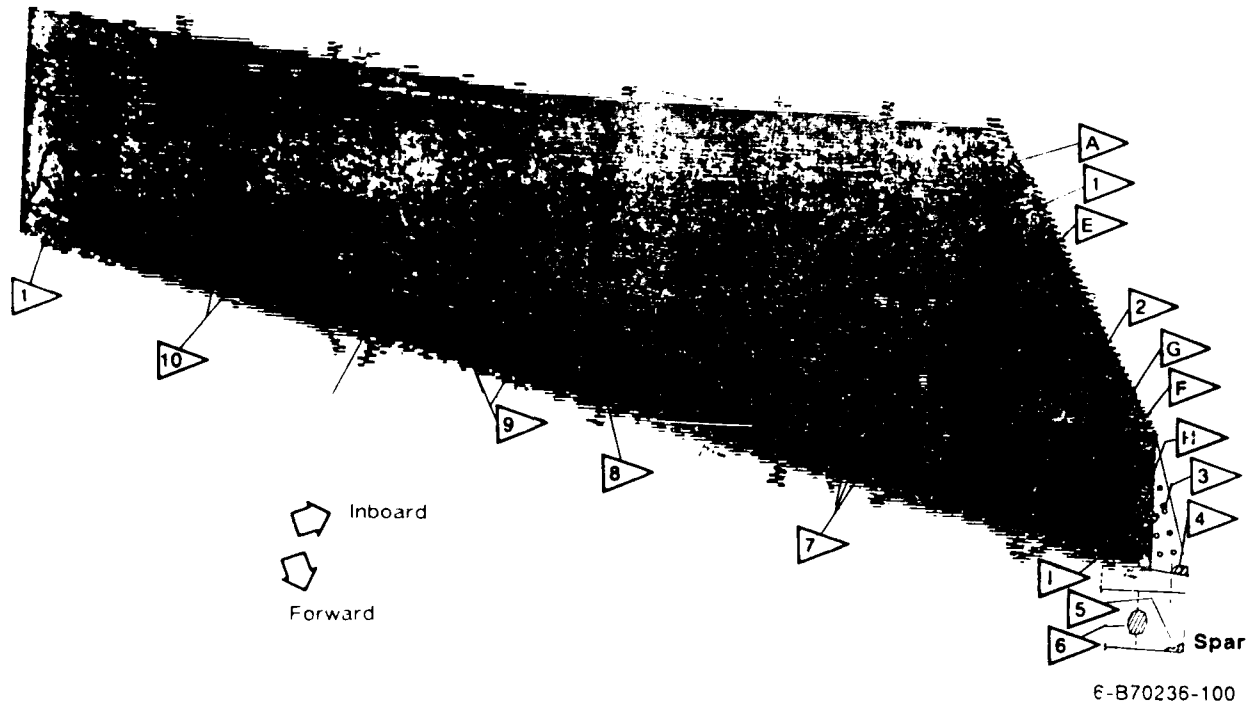


Figure 100. NDE Results of the Lower Surface

6-B70236-100

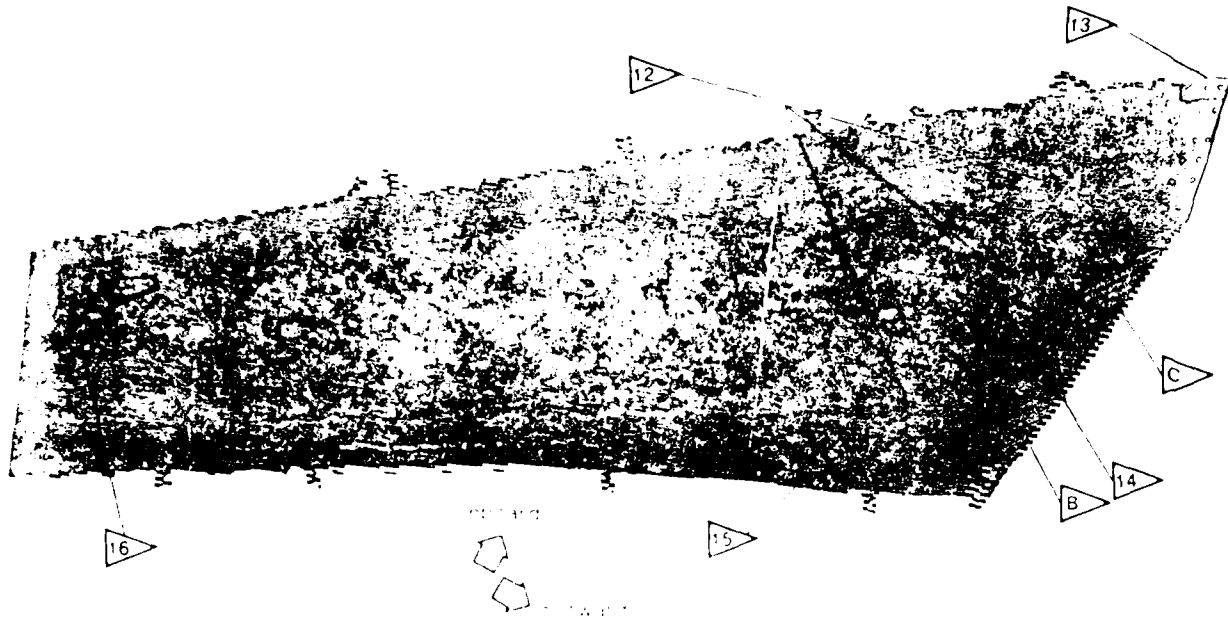


Fig. 1. - A typical sample of the sandstone.

F-B70236 101

6.2.2 Materials Characterization

Following the nondestructive inspection, material characterization of the wing was performed to verify material composition, ply orientation, ply layup, and material processing/cure.

The materials used to construct the wing were found to be carbon, boron-tungsten, and fiberglass fibers in an epoxy resin. These material constituents were identified by the following techniques; SEM, optical microscopy, electron probe microanalysis, and electron spectroscopy for chemical analysis (ESCA). The fibers were identified by SEM, ESCA (see figure 102), and optical microscopy (see figure 103). The novalac based epoxy resin was identified by infrared spectroscopy. The ply orientation and number of plies were found to be consistent with engineering drawing callouts. Localized discontinuities such as resin-rich and resin-starved regions (see figure 104) were usually caused by misalignments of the extremely large boron fibers. A small amount of porosity was seen in the graphite/epoxy plies between the 0- and 90-degree plies. These discontinuities were not found to be associated with the delamination regions and therefore were not considered as contributory factors to the cause of part failure.

Using thermomechanical analysis (TMA) in the flexure mode, the T_g was found to be 212°C, consistent with specification requirements for a 177°C cure system.

6.2.3 Fractography

Because materials characterization tests revealed that the laminate was constructed per specification and drawing requirements, efforts were directed toward the determination of the fractographic features related to each of the delaminations identified by NDE. Using optical microscopy, each delamination was crack mapped to determine the mode of fracture, the origin location, and any anomalous conditions associated with the origin. The fracture mode was primarily interlaminar or intralaminar Mode I tension, with origin locations at edge defects or fastener bores. The delamination interfaces were primarily between the fiberglass and boron plies or between the 0- and 90-degree graphite plies, which are often considered the weaker interfaces in a laminate. Two delaminations at the edge of the upper skin surface exhibited features indicative of crack growth by cyclic loading, evident by the presence of macroscopic beach marks (see figure 105) or extensive rubbing damage of the mating

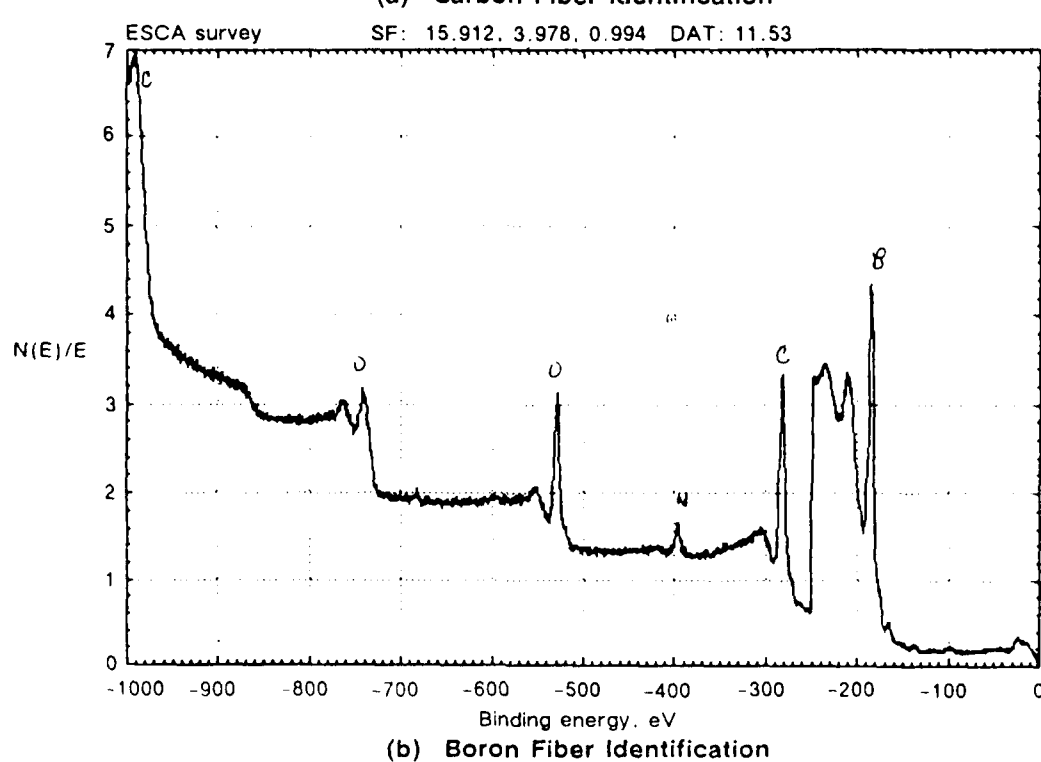
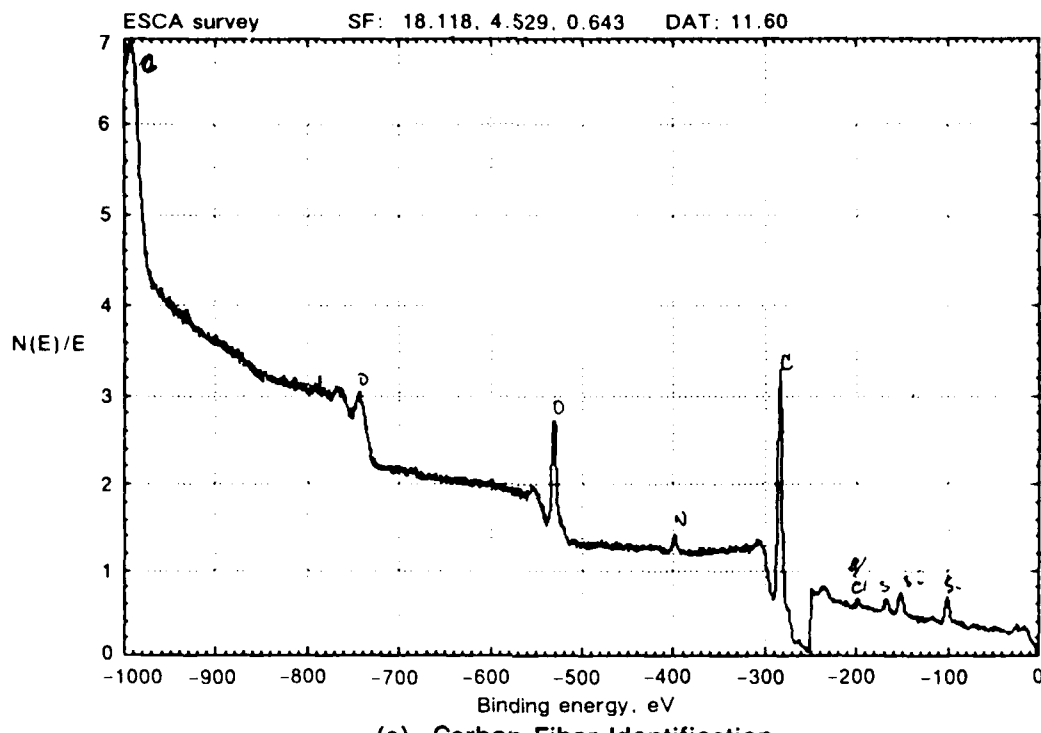


Figure 102. Fiber Identification by Surface Analysis

6-B70236-102

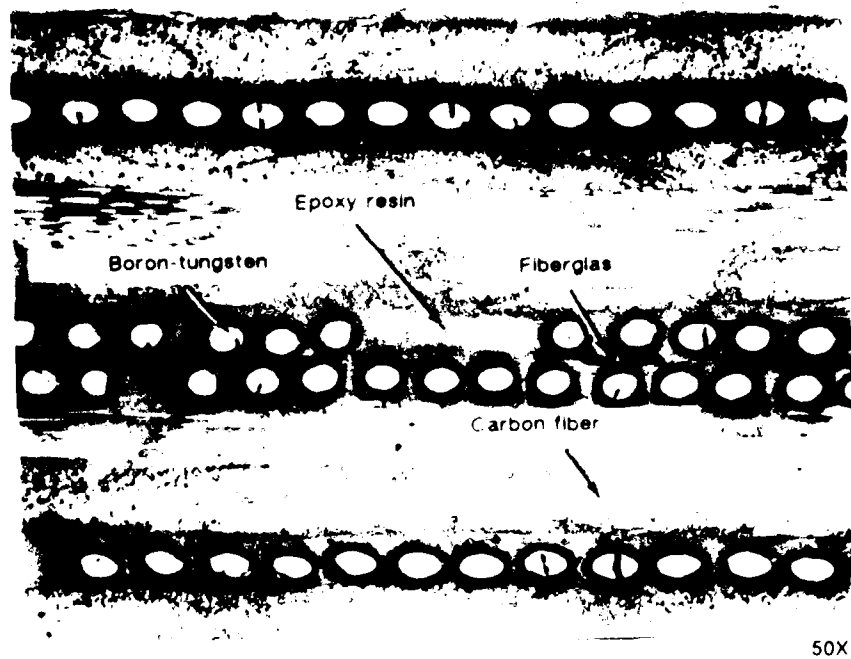
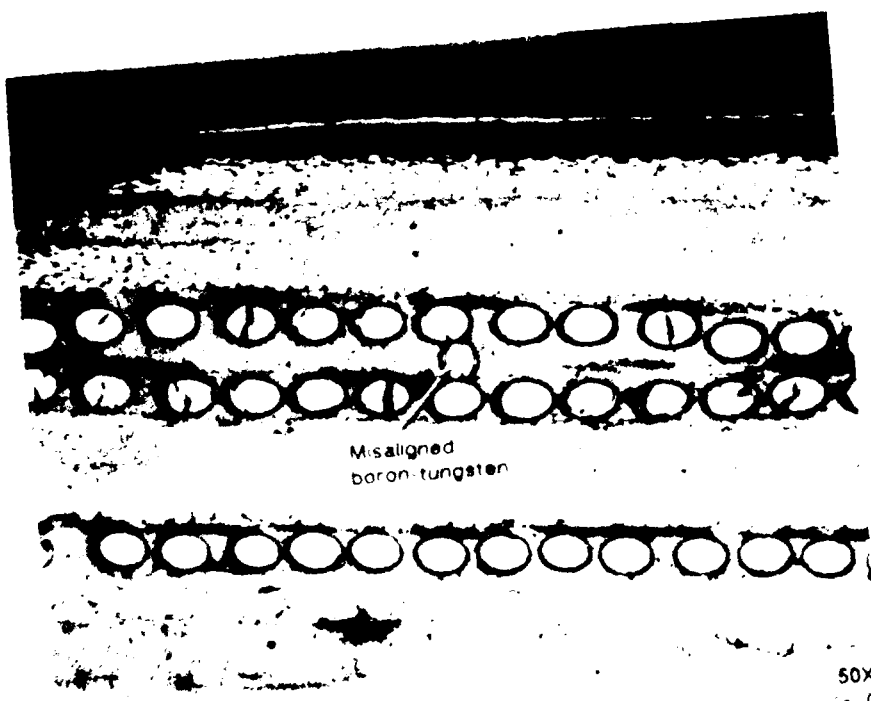


Figure 103. Photomicrograph of Cross-Section Damage Zone B

6-B70236-103



Misaligned
boron-tungsten

50X

Figure 104. Cross Section Illustrating Boron Fiber Misalignment Resulting in Resin-Rich
Adjacent Regions

6-B70236-104



Figure 105 Photomicrograph of Beach Marks Indicative of Cyclic Crack Growth and Crack Propagation Direction

6-B70236R1-105

fracture surfaces in which fine fracture details were obscured. Both of these fractures initiated at gouges at the inboard edge, possibly due to mechanical prying with blunt instruments during separation of the outboard section of the wing (following flight tests and prior to laboratory flight spectrum loading). No indications of cyclic crack growth (due to mechanical testing) were found on the other fractures. Figure 106 illustrates the features identified for each of the delamination regions. Figure 107 presents several of the fracture surfaces with arrows defining the direction of crack growth.

6.2.4 Stress Analyses

Stress analysis was not performed. This was due to limited funding and because the majority of the delaminations were associated with defect conditions identified by the techniques described above.

6.3 CARBON FIBER REINFORCED PLASTIC I-BEAM

Figure 108 shows the I-beam in its as-received condition. This component was fabricated by personnel at the Air Force Wright Aeronautical Laboratories (AFWAL). Information regarding the component layup, material composition, resin content, and cure temperature was provided by AFWAL. The component was tested in a four-point bend test. The I-beam consisted of a tape laminate with vertical web and two horizontal caps, similar to stringers used to stiffen skins on aircraft wing construction. Small vertical stiffeners were secondarily bonded at several points along the length to provide support of the cap flanges during loading. Efforts were aimed at determining the cause of failure with the quickest and lowest cost methods available. As a result, examinations such as fractography were performed without a SEM, relying on macroscopic and optical means of identifying the sequence and origin of fracture.

6.3.1 Nondestructive Evaluation

NDE was performed on the I-beam to determine areas of damage or defects caused from testing or manufacturing. Visual inspection of the beam revealed bearing damage on the caps indicative of the loading points during mechanical testing. This allowed determination of the types of stress (that is, compression, tension, or shear), imparted on the various regions of the beam. For continuity throughout this discussion, the upper cap was compressively loaded and the lower cap was in tension during flexural loading.

Delamination	Origin location	Fracture mode	Comments
Section A	At sharp radius at edge of skin	Mode II shear at origin with mode I tension growth	Boron-fiberglass interface
Section B	Likely at an edge gouge	Not determinable	Abrasive rubbing prevented analyses
Section C	At edge gouge	Mode I tension	Radial crack growth with beach marks from cyclic loading
Section D	Not determined	Mode I tension	Donut-shaped defect
Section E	Fastener bore	Mode I tension	Boron-fiberglass interface
Sections F and G	At edge with no defect	Mode I tension	Crack arrested at fastener bore
Section H	Fastener bore	Mode I tension	Resin particulate from drilling-induced delamination
Section I	Fastener bore	Mode I tension	Porosity aided crack initiation of fabric graphite plies

Figure 106. Fractography Results From NASA HiMAT Wing

6-B70236-106



Section E Note: Arrows denote local crack growth directions

Figure 107. Crack Mapping Results From Selected Delamination Regions

6-B70236R1-107

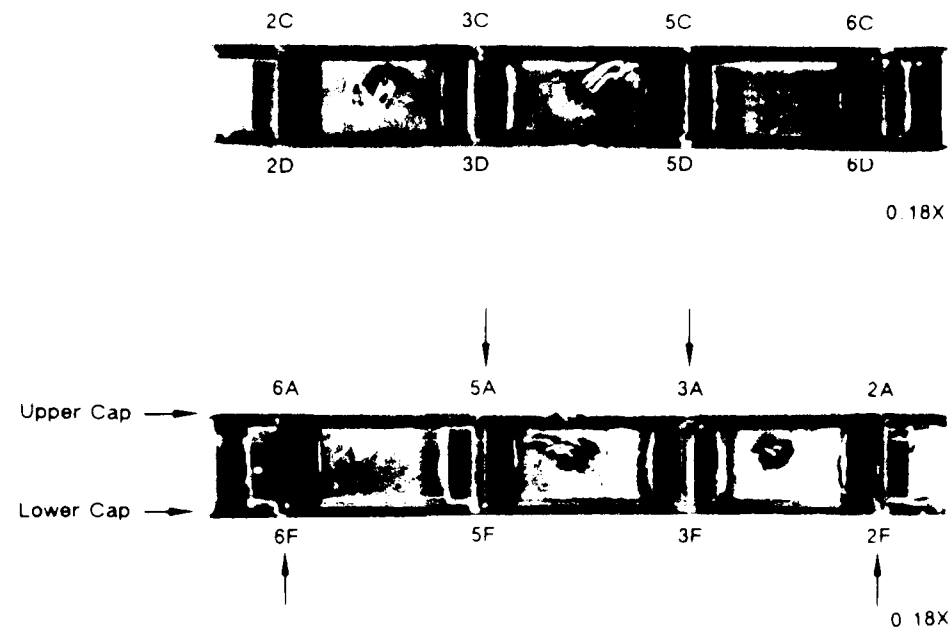


Figure 108. CFRP I-Beam in the As-Received Condition

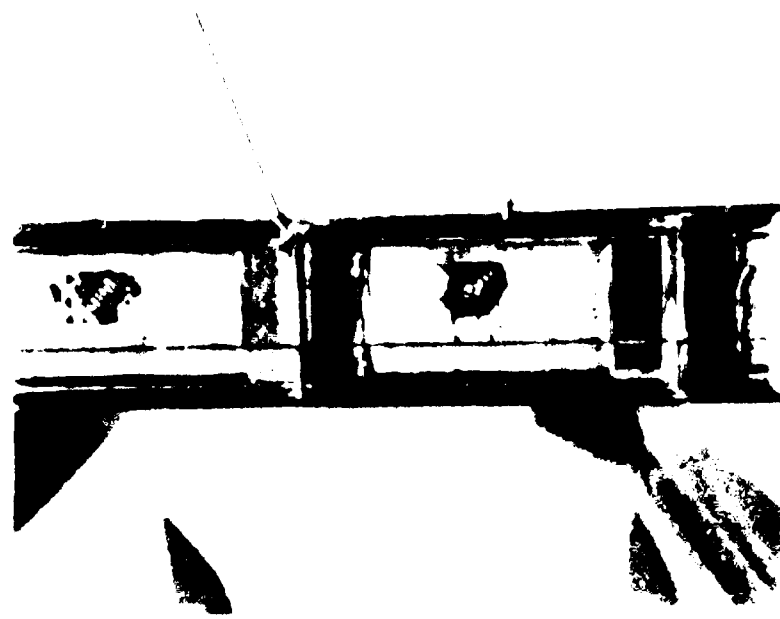
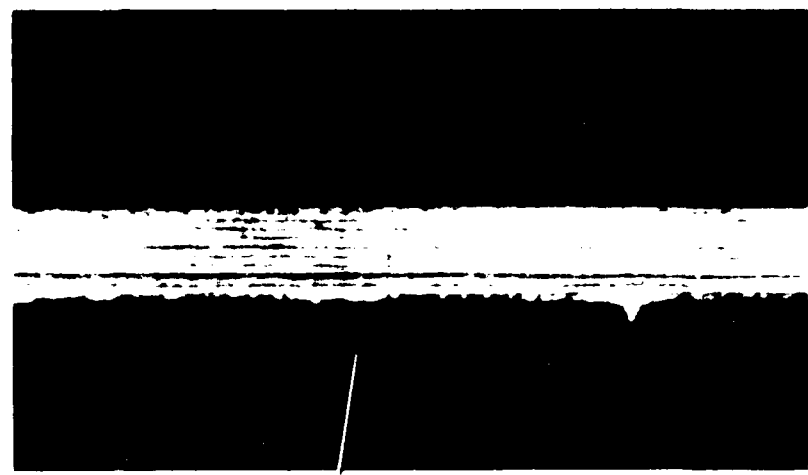
6-B70236-108

Delaminations were found at two locations in the upper cap, with remaining damage limited to brooming (localized buckling) of the small vertical stiffeners immediately below the two center loading points, most likely due to the compressive loading. These damage conditions are presented in figures 109 and 110. TTU inspection required three scans to evaluate the entire beam. First, the vertical web section was inspected. Because no delaminations were identified, the beam was cut longitudinally along the web to allow separate TTU inspection of the caps. The lower tensile cap was not damaged, however the upper compression cap was found to be delaminated in the identical regions which were visually identifiable (see figure 111). The upper cap was free of delaminations in the central region between the two loading points (an area of pure compression loading and no shear stress in the laminate plane).

6.3.2 Materials Characterization

Cross sections were performed on the ends of the beam to evaluate the laminate quality and construction. Ply counts indicated that the beam was fabricated with the correct number and orientation of plies. The overall part quality was found to be poor; extensive porosity was located at the web-to-cap junction and lack of adequate tooling constraint during cure allowed deformation through the entire laminate thickness (see figure 112). It should be noted that the extensive porosity was found to be at the same level in the upper cap as the visual delaminations.

Fiber diameters were measured to identify the fiber type (carbon AS4). Infrared spectroscopy was used to identify the novolac based epoxy resin and the presence of sulphur compounds indicative of a diaminodiphenyl sulphone (DDS) hardener used in epoxy resin systems. TMA using the flexural method was employed to determine a T_g of 379°F, verifying a complete cure of a 177°C (350°F) cure system. The resin content of each cap was determined by the density gradient column method. The resin content was 27% by weight, much less than that of the original prepreg which was approximately 34%. This was a definite concern because resin contents below 30% have been shown to significantly reduce the laminate strength, particularly for resin dominated properties such as interlaminar shear, interlaminar tension, or compression buckling.



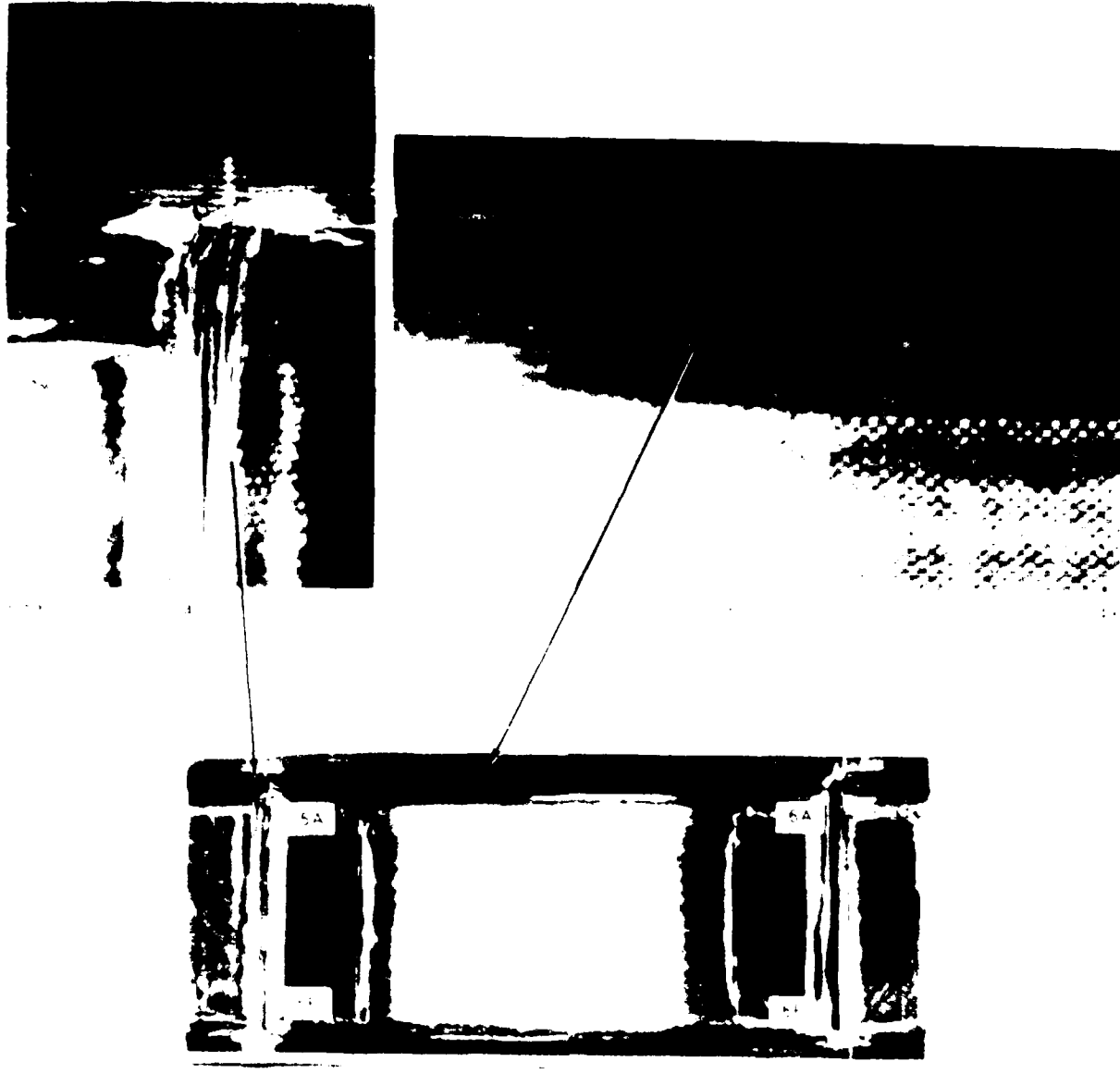


Figure 11. Another view of a. Compression Buckling and b. Delamination in the Cap
Layer of the Beam.

E. B. TUDOR, M.S.

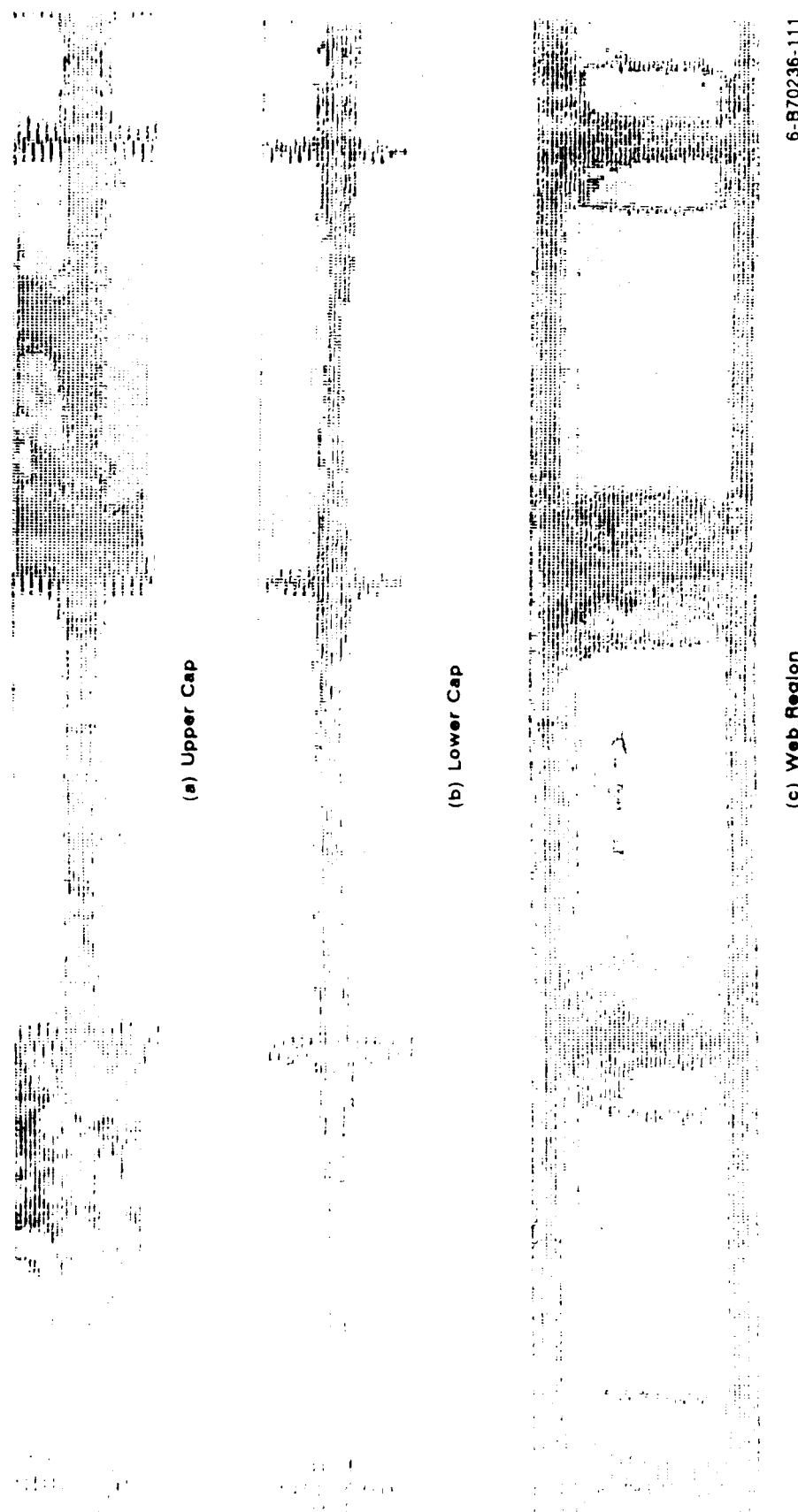


Figure 111. TTU C-Scans of the I-Beam Subcomponents

6-B70236-111



Figure 112. Extensive Porosity and Laminate Deformity in the Web-to-Cap Junction

6-B70236-112

6.3.3 Fractography

The delaminations in the upper caps were removed by cutting to prevent further delamination. Visual macroscopic inspection of the surfaces revealed the presence of both shiny and milky appearing regions, indicative of tension and shear dominated delaminations, respectively. The fracture occurred at the interface between the 0- and 45-degree plies, most likely due to the stress gradient between the axial 0-degree ply (which carries the primary axial flexural loads) and the off-axis 45-degree ply. Crack mapping was performed with the optical microscope; with the localized crack directions determined by examining the orientation of the hackles in the shear dominated regions and the river marks in the tension dominated regions. Cracking was found to initiate by shear at the web-to-cap junction, under the loading contact points. Cracking continued along the central region of the cap (where extensive porosity was evident) by a mixed mode, although primarily tension, toward the ends of the beam as shown in figure 113.

6.3.4 Stress Analyses

Although no calculations were performed, simple beam flexure theory identified the presence of an interlaminar shear stress gradient in the upper cap, being the most concentrated immediately under the central bearing points and reducing in stress toward the beam end. This gradient accounts for crack initiation by interlaminar shear at the load point, aided by the reduced strength in the cap due to extensive porosity.

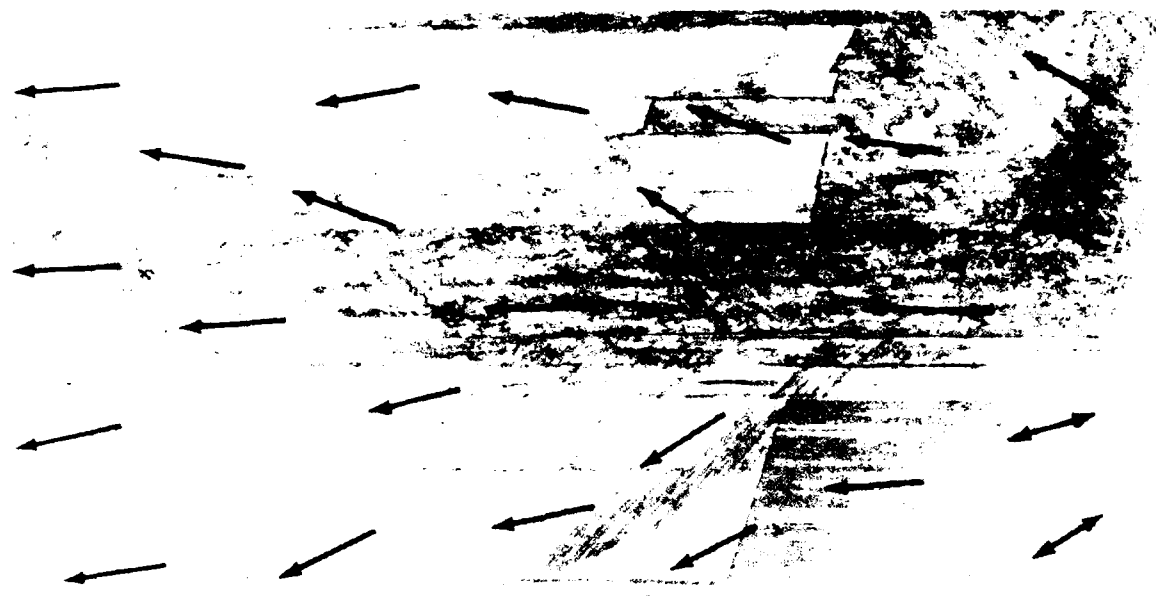


Figure 113. Results of Fractographic Crack Mapping of an Upper Cap Delamination

6-B70236-113

7.0. CONCLUSIONS

This program was designed as a major first step toward the development of a comprehensive failure analysis capability for composite material structures. The efforts performed on this multitask program have successfully achieved the three primary stated objectives. The three objectives were: (1) development of a highly flexible investigation process with a disciplined approach, or failure analysis logic network (FALN), (2) establishment of the detailed diagnostic techniques and the interpretive skills necessary to carry out this logic network, and (3) development of an instructional document (compendium) containing the logic network, required diagnostic techniques, and reference information. The attainment of each of these specific objectives has provided a capability in several of the analytical areas similar to that which exists for metals postmortem analysis and should set a firm groundwork for future research efforts.

This program was a necessary step to meet a longer term objective of having a widely disseminated and generally accepted "Composite Structure Failure Analysis Handbook" that will be similar to those for metal systems; for example, the Air Force sponsored electron fractography and failure analysis handbook.

Attainment of the first major objective involved a literature search and direct contact with several recognized experts in the field in order to compile and review the various diagnostic techniques and protocols which were currently available within the scientific community. Well developed diagnostic techniques were identified for both the nondestructive evaluation and materials characterization analytical disciplinary areas. These techniques were found to be sufficiently mature for direct incorporation into the Compendium. However, for fractography and stress analysis, the information available was insufficiently developed or documented for direct incorporation. Under task 1, the initial Boeing FALN was reviewed, updated, and expanded. Since the initial overall FALN applied to techniques on a broad scale, four sub-FALNs and supporting charts were added to the program to provide more detail regarding each of the disciplinary areas of nondestructive evaluation, materials characterization, fractography, and stress analysis.

The result of the task 1 review provided direction toward the development of the analytical disciplinary field of fractography, which was definitely at an infancy level of

capability as indicated through the literature review. Tasks 2 and 3 involved the fractographic examination of pedigree specimens that failed under tightly controlled conditions of a 177°C (350°F) AS4/3501-6 graphite/epoxy system. The results provided valuable baseline information for determination of the specific fracture features relative to crack growth directions, relative load state, and separation mechanisms for a variety of simple and complex failure conditions. Significant accomplishments involved interlaminar Mode I tension and Mode II shear fractures relative to determination of crack growth directions and fracture mechanisms.

The completion of task 4 provided a reference document which presented an overview of the analytical and diagnostic techniques that can be used to determine the causes of failure in continuous fiber reinforced composite materials. Such techniques included flow charts describing the logical arrangement of the investigative operations using fractography, materials characterization, nondestructive evaluation, and stress analysis as the primary diagnostic procedures. Interpretive methods were also presented to illustrate how to evaluate the information obtained during the application of the various analytical techniques. Finally, supportive data such as case histories of actual failure analyses and an extensive atlas of fractographs were included to provide a comparative reference source.

The Compendium has been provided to AFWAL as contract data requirements list (CDRL) item number 6, and should be considered as a precursor to a more comprehensive handbook which will be generated through Air Force Contract No. F33615-86-C-5071 (Boeing) and F33615-87-C-5212 (Northrop).

Task 5 involved the demonstration and evaluation of the FALNs, various analytical techniques, as well as the overall capability to adequately define the cause of failure. During the performance of this task, the cause of failure of three composite structural components were successfully determined. The FALNs and the various analytical techniques developed within this program were used to identify the sequence of failure, the origin locations, the loading conditions, and the direction of crack propagation for the following structural components:

- V-22 Osprey full scale wing test box.
- NAS HiMAT test wing.
- I-beam.

The successful results obtained during the postfailure analyses investigations suggested that the technology has come a long way since its start in the late 1970's. Through efforts within this program as well as other research programs from the scientific community, it is evident that many of the analytical instruments and methods are approaching the capability currently available for metals failure analysis. The primary deficiency evident through actual application of the various techniques on failed components, such as those evaluated in task 5, is that the fractography interpretive methods are still in the infancy stages. Although the capability to understand the microscopic fracture mechanisms and the characteristic microscopic fracture features are rapidly evolving from programs such as this, future efforts need to be aimed at lower magnification fracture analyses. Although experience through routine failure analysis investigations from the scientific world will ultimately provide the basis for this macroscopic capability, the Air Force sponsored programs subsequent to this program should significantly expedite the advancement of fractography for macroscopic investigations of fractured components.

8.0 GLOSSARY

AFWAL	Air Force Wright Aeronautical Laboratories
Beach Marks	Indicators of the beginning and end of incremental crack growth.
Brooming	localized buckling
CAI	compression after impact
CDRL	contract data requirements list
CLS	crack lap shear
Coupons	a small test specimen (or a portion of a large specimen).
DCB	double cantilever beam
DDS	diaminophenyl sulfone
ENF	end-notch flexural
ESCA	electron spectroscopy chemical analysis
FALN	failure analysis logic network
FEP	fluorinated ethylene propylene
Fractography	the detailed examination of the fracture surface of a failed component
Interlaminar	a fracture in composite materials <u>between</u> the plies on a plane parallel to that of the fiber reinforcement (delamination)
Intralaminar	a fracture in composite materials <u>within</u> the plies on a plane parallel to that of the fiber reinforcement (delamination)
IR&D	independent research and development
MMF	mixed mode flexural
MTS	mechanical testing system
NDE	nondestructive evaluation
Pedigree	the documented quality of a material (or specimen) which assures a representative (valid) test

Rail Shear	inplane transverse shear
River Marks	the multitude of microplanes that initiate at the fiber-matrix interface and link up as the crack propagates resulting in a coalescence of steps forming a branched pattern
SEM	scanning electron microscope
Striations	parallel sets of curved lines found at either the fiber-matrix interface or in the matrix resin
TGDDM-DDS	tetraglycidyl diaminodiphenyl methane-diaminodiphenyl sulfone
TMA	thermomechanical analysis
Translaminar	a fracture in composite materials having broken fibers as the dominating feature and extremely rough topography
TTU	through-transmission ultrasonic

END

10-87

DTIC